MANIPULATIONS OF VISCOELASTIC INSATBILITY AND INTERFACIAL SURFACE FORCES IN MICROFLUIDIC DEVICES FOR BIOMEDICAL AND MATERIAL SCIENCE APPLICATIONS

by

Chuan-Hsien Kuo

A dissertation submitted in partial fulfillment
of the requirements for the degree of
Doctor of Philosophy
(Mechanical Engineering)
in The University of Michigan
2010

Doctoral Committee:

Associate Professor Claus Borgnakke, Co-Chair
Associate Professor Shuichi Takayama, Co-Chair
Professor Ronald G. Larson
Professor Michael Thouless

To My Parents, and My Wife

Acknowledgements

This Dissertation is a culmination of research works that I had the opportunity to conduct either in the leading role, or to have a major contribution in a supporting role. However, it contents much more than just the academic research efforts of one person or a team; it is also a manifestation of good friendships and great working relationships I had experienced over the last few years in Professor Takayama‘s lab.

First and foremost, I would wish to express my sincere gratefulness toward Professor Shuichi Takayama of the Biomedical Engineering Department, my dissertation committee Co-chair. He kindly welcomed me to his lab when I was still wondering if I should have come back to school; and opened my eyes to the various exciting research topics. His vision, keen sense and foresight in the interdisciplinary fields relating to microfluidics had guided me along from novice in the field into someone who could perform effective, independent research. His unique approach allows the lab to be filled with creative challenging ideas, while keeping casual, stress-free environment. Without his mentorship, advices, and kind encouragements; none of the researches would be successfully conducted. The lessons I have learned from Professor Takayama here will serve as the model for the rest of my professional careers.

Next, I would like to express special thanks to my other committee co-chair, Professor Claus Borgnakke of the Mechanical Engineering. As the only remaining member of my former dissertation committee, his assistance in supporting my effort to return to school is what makes all the following research efforts even possible. Over the years in Takayama lab, he continued to provide me with advices and insight in area of fluid mechanics; with useful suggestions in analysis. I will be always thankful for his kindness and support.

There is much thanks to the other two committee members also. From working with Professor Thouless, I have learned valuable lessons about thinking as a researcher instead of an engineer; not an easy transformation after years in the industry. His great knowledge, straight-forward comments and advice, and constructive criticism had improved me along the study. It is also my great fortunate to meet Professor Larson during the research, his great knowledge and insight in the subject of viscoelastic instability had provided valuable resources for the current research.

There will always be a special place in my heart for my formal dissertation chair, Professor Emeritus Wen-Jei Yang of mechanical Engineering. He had always given me great guidance and kind encouragement during my early days in University of Michigan. Always believing me, he had never stopped helping me in my long and sometimes difficult road of doctorate research. Unfortunately he had passed away in April of this year, just before my oral defense; he is with god now. I will always miss him; and in his loving memory I will continue to be a better person and researcher, as he had wished me to be.

In addition to the guidance from professors, none of the research works would be possible without the helps, advices and tips I have received from the both the formal and current members of the Takayama lab. From the first day I was here, they have shown me great friendships and team work spirits. These includes: Lab Administrator Mayte Brown, Dr. Hossein Tavana, Dr. Yoko Kamotani, Dr. Dongeun Huh, Dr. Yi-Chung Tang, Dr. Tommaso Bersano-Bengy, Dr. Nobuhiro Kato, Dr. Nobuyuki Futai, Dr. Yusuke Torisawa, Dr. Jonathan Song, Dr. Alan Tkaczyk, Dr. Yunseok Heo, Dr. Wansik Cha, Dr. Albert Chueh, Dr. Angela Dixon, Dr. Joong Yull Park, Dr. Geeta Metha, Dr. Toshiki Matsuoka, Bobak Mosadegh, Amy Hsiao, Andre Chung, Andreja Jovic, Steve Cavnar, Nick Douvulle, Steve Allen, Arlyne Simon, Byoung Choul Kim, David Lai, Joshua White, Sasha Cai Lesher-Perez, and Robert Miguez. I also enjoyed working with great people from Thouless group: Dr. Kristen Mills, Yitao Zhuang, Rebecca Rousseau, Hai Wang, and Zhengyu Li. Various staff members from both mechanical and biomedical

engineering departments had provided me with administrative and research assistances, especially Cynthia-Quann White, Ruth Halsey, and Tonya Brown.

Finally, I would like to express my most sincere gratefulness and loves to my family who had given me continuous supports through all. Both of my parents, Chao-Yang and Ming-Liang Kuo, had instilled in me the value of hard works and joy of learning since youth, something that I will treasure for the rest of my life. They had never stopped believing in me, even when I was having doubts during difficult times. I am so fortunate to be their child; and if I could have some small measures of success and accomplishment in my life, it would be because of them. Last, but definitely not least, I wish to express my endless love and thanks to my most loving wife, Chia-Ling Yen. She had stayed by my side through it all, thick and thin; and endured so much. My life will be void without her love and care.

TABLE OF CONTENTS

LIST OF FIGURES

Figure

ABSTRACT

MANIPULATIONS OF
VISCOELASTIC INSTABILITY AND INTERFACIAL SURFACE FORCES IN MICRO FLUIDIC DEVICES FOR BIOMEDICAL AND MATERIAL SCIENCE APPLICATIONS

by

Chuan-Hsien Kuo

Co-Chairs: Claus Borgnakke and Shuichi Takayama

As a highly viscoelastic liquid, flowing blood exerts a shearing force that has a significant effect on the functioning of vascular endothelial cells (ECs), which regulates the human circulatory system. The first part of the thesis describes a microfluidic device along with a specially formulated media to provide an in-vitro testing microenvironment where cultured endothelial cell layers can be subjected to shearing forces from both stable and unstable flows. Complex and unstable flow patterns are generated within this microchannel device by engineering the viscoelastic properties of the EC culture media without the need of an extensive flow agitation apparatus. In-vitro shearing tests showed significant differences in the responses of Human Umbilical Vein Endothelial Cell (HUVEC) layers to laminar stable and complex unstable flows. The second part of the thesis describes a microfluidic method to generate uniform-sized polydimethylsiloxane (PDMS) microspheres over a size range of 85-200 microns by manipulation of the microchannel two-phase flow. Viscous PDMS prepolymer is pushed out of the middle channel of a 3-inlet-1-outlet converging microchannel flanked on each side by flow of an aqueous surfactant solution. Unique surface crack patterns are generated on the surfaces

of PDMS microspheres, and they are decorated by coating them with fluorescent protein and gold nanoparticles, which could be further enhanced into gold or silver nanowires. The unique ability to generate controllable selective 3D deposition patterns on PDMS microspheres introduces a new class of microscale functional materials, and provides opportunities for a multitude of material science and biomedical applications. Finally, the effect of channel surface properties on air- liquid two–phase flows and plug flows in a microchannel are investigated. Manipulation of the surface properties creates a several distinct flow regimes in a Y-shaped microchannel; and affects different plug propagation conditions in a K-shaped design, with important clinical implications for pulmonary airway cells injury.

CHAPTER 1

Introduction and Thesis Overview

Advancements in microfluidic technology has brought a new exciting dimension to many fields of scientific research, particular in the fields of chemical analysis, biotechnology, and material sciences. By reducing the dimensions of the devices, many advantages are brought forward. The abilities of minimal reagent use, quick testing result, high sensitivity and high throughput make it attractive tool for chemical analysis [1,2]. In Biology, the microfluidic systems approaching cellular dimensions can better simulate human physiology environments, both mechanically and chemically, than many current in-vitro tools such as petri-dishes; while the ability to control in-vitro test condition such as chemical gradient give microfluidic devices an added advantage. [3,4,5] Advancement of the micro-fabrication technology and quick prototyping, such as soft lithography [6,7]; and the abilities to make many miniaturized fluidic control and actuation components, such as valve, pump and mixers [8,9,10] have further pushed the utility and the popularity of microfluidic technology.

As the name suggests, the main characteristics of the microfluidics system is its miniaturized size. The fundamental differences between the fluid flow in macroscale dimensions and microscale had been studied and utilized [11,12]. Mainly, the flow in microchannels has been described as stable, laminar flow, characterized by very low Dimensionless Reynolds number (*Re*):

$$\mathrm{Re} = \frac{\rho U L}{\mu}$$

Where ρ, and μ are the density and viscosity of the fluid, *U* and *L* are the characteristic velocity and dimension of the flow. *Re* basically is a ratio of inertial versus viscous forces proportional to the importance of the inertial effects. In a microchannel flow, viscous force usually dominates. This inherent characteristic could be an advantage or a disadvantage of the microchannel, depending on the applications. For instance, for micromixer application, laminar flow does not promote good convective mixing due to the stable stratification of the flow field; and creative microchannel designs need to stir the stratification and promote mixing through diffusion [10,11]. Also, one main point of microfluidic flow noticed by researchers is the absence of turbulence [1,11]; in macroscale flow, turbulent flow is characteristic by high Reynolds number, where inertial forces dominate over viscous forces. Physically, in a microchannel, the miniaturized dimension in many ways is associated with small characteristic length, and thus a low Reynolds number and the absence of turbulence.

However, turbulent, unstable flow does not come from inertial forces alone. In industry, irregular flow patterns have long been observed in polymeric and other elastic fluids [13]; and trace amounts of highly elastic polymer in non-Newtonian viscoelastic solutions (with negligible inertia) can lead to purely elastic flow instabilities [14], making possible of low Reynolds number unstable flow. Later, researchers start to analyze the underlying mechanism of these particular kinds of flow instability, caused not by the inertial force of the fluid, but the elastic forces associated with the polymeric molecules within the fluid. Since then, researches have gained better knowledge of this unstable flow phenomenon, which share many of the same characteristics of Newtonian turbulence and sometimes has been called "Elastic Turbulence" itself [15]. The initiation, and transitions of this flow instability (or elastic turbulences) has been extensively studied for polymeric solution between rotating parallel plates or concentric cylinders (Taylor–Couette flow) [13,14,16]; and through these studies, the mechanism was deducted that, elastic 'normal stresses' was generated by the stretching of the polymer molecule along circular streamlines, which squeeze fluid inward, leading to a radial pressure gradient, and producing for example the famous "rod climbing" effect. The

magnitude of polymer stretching, and the associating tendency for a flow to become unstable is controlled by the Weissenberg number (*Wi*):

$$Wi = \nabla V \times \lambda$$

where ∇V is the shear rate and λ the characteristic polymer relaxation time [16]. Relaxation time is an elastic property of polymer solutions, where stress does not immediately become zero when the fluid motion stops, but rather decays with some characteristic time that is the relaxation time [15]. The value of Wi $\geq$ 0.5 is generally consider to be the value at which flows become unstable [17]. Viscoelastic effects and applications in microchannel is still a very understudied field, with main research interests focused on efficient mixing [18], and generating non-linear flow response for potential use as microfluidic logic components [19,20]; but not for biomedical applications. However, since blood is a strong non-Newtonian fluid [21-22], human blood vessels do have complex geometries, and arteries have high Reynolds' Number flow and hence turbulence, microfluidic application of viscoelastic disturbed flows to vascular research, such as endothelial cell (EC) monolayer shearing, may bridge the gap between macroscale studies of unstable blood flow by use of viscoelastic fluidic loops ex vivo (no EC cells)[23,24]; and microchannel based in-vitro studies which is mainly based on mechanically agitated Newtonian flow [25,26]. This attempt will be an important part of this research.

Another characteristic of micro fluidic fluid flow is the dominating role of the surface forces; as indicated by the scaling law, where high area (square) to volume (cubic) ratio become very large when the length scale is small[11,12]. The surface effect is especially important in microscale two phase flows in microchannels; since the contact area between fluids, and fluid to channel wall are all proportionally large by scale, adding complexities in analysis and control.

In microfluids systems, the application of two-phase flows offers additional opportunities to extend beyond traditional single-phase microfluidics. The potentials of two-phase flows at the microscale were utilized in a wide variety of applications such as

emulsification [27,28], electronic chip cooling [29], chemical reactions [30], flow cytometry [31], material synthesis and fabrication [33,34], chemical detection or screening [35] and cell-fluid interaction[36,37].

By careful manipulation of the surface forces many of above application can be further optimized and expand for further use. For instance, emulsification can be better controlled by flow focusing and change of working fluid surface energy to produce droplet sizes not limited to the geometrical dimension [38,39], make possible manufacturing of extremely small microspheres from even viscous pre-polymer flow; multiple two phase flow streams can be controlled, or switched to joint (mix) and separate on demand by dynamically changing the microchannel surface property [32], and physiological relevant liquids plugs can be generate, controlled, and utilized in microchannel to perform parameter controlled biological study with lung cells in vitro [37,40]. The second part of thesis will concentrate on the studies of varied two-phase flow phenomena and importance of surface force effects.

Overall, the Main objective of this thesis is to present a variety of microchannel applications beyond traditional single phase, stable, laminar flow regime; and aims to show that, by innovative design and utilization of various fluid mechanic principles, microfluidic devices can reach beyond the inherent limitations that is generally associated with its microscale dimensions and low Reynolds number flow operation; while retaining its advantage as a simple, resource efficient, high throughput, and physiologically relevant platform for biomedical and material science applications. Chapter 2 introduces a viscoelastic working fluid based microfluidic device to apply viscoelastic unstable flow to cultured endothelial cell layers. Taking advantage of the high molecular weight polymer added cell culture media, highly unstable flow is generated in microfluidic, low Reynolds number flow environments. It is postulated that the visco-elasticity of the polymer modified media recreates physiological unstable flow in-vitro better than many of the Newtonian flow based systems in simulating complex hemodynamic environment experienced by EC cells. Chapter 3 describes the manipulation of the flow-focusing phenomena in microchannel to generate 85-100 micro sizes microspheres from highly

viscous Polydimethylsiloxane (PDMS) prepolymer. With possibilities to get even smaller, approaching the cellular size scale. PDMS is a popular material in many biomedical and material science applications. Taking advantage on one of PDMS's unique chemical property, nano-scale crack patterns, with abilities to deposit varies functional materials within, can be applied to the surface in a controllable fashion on the surface of the PDMS microspheres. Chapter 4 describes the impact of surface wetting properties of the walls of the microfluidic channels on the applied air-water two-phase flow. Surface tension forces between the liquid and the channel wall and interfacial instability between air and water phase flow introduce varies flow regimes in the microchannels. Flow mapping experiments are performed and the flow regime observations are compared with relevant works in literature; with the fundamental mechanics discussed. Chapter 5 describes a way to generate micron sized liquid plug in microchannel, in an attempt to simulate the formation of liquid plug in the respiratory air ways. The formation, propagation, and rupture of the liquid plug in the air way has been identified with a form of lung injury cause by the high shear stress caused by the advancing of the liquid plug in narrow airways. The mediating effects of the surfactant solution on plug formation and propagation, based on the reduction of surface tension force, are discussed.

References:

1. G. Whiteside, *Nature*, 2006, 442, 368-372.
2. K. Jensen, *MRS Bull.*, 2006, 31, 101–107.
3. P. J. Hung, P. J. Lee, P. Sabounchi, R. Lin, L. P. Lee, *Biotechnology and Bioengineering*, 89,1, 1-8.
4. B. G. Chung, L. A. Flanagan, S. W. Rhee, P. H. Schwartz, A. P. Lee, E. S. Monuki, and Noo Li Jeon, *Lab on Chip*, 2005, 5,401-406.
5. S. Takayama, E. Ostuni, P. LeDuc, K. Naruse, D. E. Ingber, and G. M. Whitesides, *Chemistry & Biology*, 10, 123–130.

6. D. Duffy, J. C. McDonald, O. J. A. Schueller and George M. Whitesides, Anal. Chem., 1998, 70, 4974-4984.

7. G. M. Whitesides, E. Ostuni, S. Takayama, X. Jiang, and D. E. Ingber, Annu. Rev. Biomed. Eng., 2001, 3, 335-373.

8. D. B. Weibel, M. Kruithof, S. Potenta, S. K. Sia, A. Lee, and G. M. Whitesides, Anal. Chem., *2005*, 77 (15), 4726–4733

9. N. T. Nguyen & Z. G Wu, *J. Micromech. Microeng*, 2005, 15, R1-R16.

10. D. J. Laser and J. G. Santiago, J. Micromech. Microeng., 2004, 14, R35-R64.

11. H.A. Stone, A.D. Stroock, and A. Ajdari, *Annu. Rev. Fluid Mech.*, 2004, 36, 381–411.

12. T. M. Squires and S. R. Quake, *Rev. Mod. Phys*., 77, 977–1026

13. R. G. Larson, *Nature*, 2000, Volume: 405, pp. 27-28

14. R. G Larson, 1992, Rheol. Acta. 31, No. 3, pp.213-26

15. A. Groisman, and V. Steinberg, 2000, *Nature*, Volume: 405, pp. 53-55

16. B. A. Schiamberg,L. T. Shereda, H. Hu and R. G. Larson, J. Fluid Mech., 2006 ,554, 191–216.

17. Groisman, M. Enzelberger and S. R. Quake, *Science*, 2003, 300, 955-958.

18. T. Burghelea, E. Segre, I. Bar-Joseph, A. Groisman and V. Steinberg, *PHYSICAL REVIEW E*, 2004, 69, 066305: 1-8.

19. A. Groisman, M. Enzelberger and S. R. Quake, *Science*, 2003, 300, 955-958.

20. A. Groisman and S. R. Quake, *Phys. Rev. Lett*., 2004, 92, 9, 094501:1-4.

21. P. J. Marascalco, S. P. Ritchie, T. A. Snyder, M. V. Kameneva, *ASAIO J.*, 2006, 52, 5, 567-574

22. B. Thurston and N. M. Henderson, *Biorheology*, 2006, 43, 729–746

23. K. M. Khanafer, J. L. Bull, G. R. Upchurch Jr., and R. Berguer, *Annals of Vascular Surgery*, 2007, 21,1, 67-74.

24. T. T. Tsai, M. S. Schlicht, K. Khanafer, J. L. Bull, D. T. Valassis, D. M. Williams, R. Berguer, K. A. Eagle, *J. Vasc. Surg*., 47, 4, 844-851.

25. N. Kataoka, S. Ujita and M. Sato, *Med. Biol. Eng. Comput.*, 1998, 36, 122-128.

26. S. Chien 2008, *Annals of Biomedical Engineering*, 2008, 36, 4, 554-562.

27. Utada A S, Lorenceau E, Link D R, Kaplan P D, Stone H A and Weitz D A 2005 *Science* 308 537

28. Sugiura S, Nakajima M, Tong J H, Nabetani H and Seki M 2000 *J. Colloid Interface Sci.* 227 95.

29. Zhang L, Koo J M, Jiang L, Asheghi M, Goodson K E, Santiago J G and Kenny T W 2002 J. *Microelectromech. Syst.* 11 2002

30. Song H, Chen D L and Ismagilov R F 2006 *Angew. Chem., Int. Ed. Engl*. 45 7336

31. Huh D, Tung Y-C, Wei H-H, Grotberg J B, Skerlos S J, Kurabayashi K and Takayama S 2002 *Biomed. Microdev.* 4 141.

32. Huh D, Tkaczyk A H, Bahng J H, Chang Y, Wei H-H, Grotberg J B, Kim C-J, Kurabayashi K and Takayama S 2003 *J. Am. Chem. Soc.* 125 14678.

33. Yen B K H, Gunther A, Schmidt M A, Jensen K F and Bawendi M G 2005 *Angew. Chem., Int. Ed. Engl.* 44 5447.

34. Millman J R, Bhatt K H, Prevo B G and Velev O D 2005 *Nat. Mater.* 4 98.

35. Lau B T C, Baitz C A, Dong X P and Hansen C L 2007 *J. Am. Chem. Soc.* 129 454

36. Boedicker J Q, Li L, Kline T R and Ismagilov R F *Lab Chip* 8 1265.

37. Huh D, Fujioka H, Tung Y-C, Futai N, Paine R, Grotberg J B and Takayama S 2007 Proc. Natl. Sci. Acad. USA 104 18886.

38. Anna, S. L.; Mayer, H. C. *PHYSICS OF FLUIDS* 2006, 18, 121512-1:13.

39. Lee, W.; Walker, L. M.; Anna, S. L. PHYSICS OF FLUIDS 2009, 21, 032103-1:14.

40. H. Tavana, C.-H. Kuo, Q. Y. Lee, B. Mosadegh, D. Huh, P. J. Christensen, J. B. Grotberg and S, Takayama, Langmuir 2010, 26, 5, 3744–3752.

CHAPTER 2

A Viscoelastic Approach to Investigation of Unstable Flow Shearing Effects on Endothelial Cell Layers in Microfluidic Channels

Blood flow shearing forces have significant effect on the vascular endothelial cells (ECs) function, which regulate the human circulatory system. This work describes a microfluidic device along with specially formulated media to provide an in-vitro testing microenvironment where cultured endothelial cell layers are subject to shearing forces from both stable and unstable flows. Complex and unstable flow patterns are generated within this microchannel device, without the need of extensive flow agitation apparatus, by engineering the viscoelastic properties of the EC culture media. In-vitro shearing tests showed significant differences in Human Umbilical Vein Endothelial Cell (HUVEC) layers responses to laminar stable and complex unstable flows created by viscoelastic culture media. The results show that the microfluidic experiments using viscoelastic media produce endothelial cell responses that are more in-vivo-like even compared with results achieved by larger, more elaborate, Newtonian flow based test platforms that produce various types of disturbed flows. This viscoelastic microfluidic approach could potentially provide a simple, efficient, high-throughput compatible platform in studying and understanding the effects of disturbed flow patterns on ECs layer function.

2.1 Introduction

Cardiovascular disease is a major threat to the health of millions, and underlying many clinical cardiovascular disorders is a chronic blood vessel disease called atherosclerosis, a hardening of the blood vessel wall and the growth of the lesions which often lead to stenosis (narrowing) condition. The early clinical observation of the fact that atherosclerotic lesions often develop at "predictable" sites attracted great research interests both in vitro and in-vivo. The research has revealed the role of hemodynamic forces (1-6). Especially, complex, unstable blood flow patterns, have significant impacts on endothelial cell (EC) functions; these includes growth and alignment (7-12), cytoskeletal changes (4,14-17), calcium response (18), nitric oxide (NO) production (19-21), gene expression(5,21-16), and changes in junction protein integrity (2, 13, 27-31). Several of above effects have been identified as key factors in promoting or resisting development of atherosclerosis.

Current in-vitro studies into the effects of unstable flow shearing forces on EC layer rely on extensive mechanical setups. The Newtonian nature of the working fluids, mainly cell culture media, necessitate the use of complex fluid actuation/control apparatus to artificially modulate flow directions of the test fluid over the EC layer sample in an attempt to mimic the complex flow dynamics observed in-vivo without using large volumes of media and cells. These flow agitation techniques include the use of spinning cone- sample plate set- up similar to the viscometer (23,32-34); the use of oscillatory pump driven fluidic circuit toward a cell chamber (12,14,24,30,35-37); and pump driven parallel aligned silicon tubing as cell chamber (27-28). Although much knowledge has been gained, these flow actuation methods are not efficient methods to generate physiologically relevant complex flow environments for reagent, equipment, and resource effective EC layer testing. In the case of silicon tubing type EC test loops (27-28), the tests need to be terminated to make cellular observations. Advancement of microfluidic devices offers an attractive tool for many areas of EC research (11,38); offering an efficient, integrated test platform in a small, scalable package. However, due to the dimension of the flow channel, microfluidic flow is generally associated with

stable laminar flow patterns. This characteristic limits its use in EC layer shearing studies that require a disturbed, unstable or complex flow pattern.

Here, we present a microfluidic device together with viscoelastic media formulations capable of serving as an in-vitro ECs layer shearing test platform of transient unstable flow patterns using small dimension devices and in a reagent economic manner. The challenge is to accomplish transient unstable flow patterns typical of large scale high speed fluid flows using small channels with small volumetric flow rates. These seemingly contradictory needs are met by utilizing the properties of the viscoelastic properties of a modified EC culturing media together with geometrical designs of specifically-designed microchannels. Transient flow instability is thus generated in the microchannel, based on the phenomena of viscoelastic instability (39-42), without the need for an elaborate control and actuation apparatus. Thus far, the application of the viscoelastic instability in microfluidics had been mainly proposed for efficient mixing (40,43-44), and generating non-linear flow response for potential use as microfluidic logic components (45,46); but not for biomedical applications. However, since blood is a strong non-Newtonian fluid (47-50) and human blood vessels do have complex geometries, this microfluidic approach to EC monolayer shearing is not completely unphysiological.

Shearing tests were performed on Human Umbilical Vein Endothelial Cell (HUVEC) layers, a commonly used EC for cardiovascular research (51-55), under both laminar stable and transient unstable flow patterns with these microchannel devices. Significant differences in cells layer morphology and junction protein VE-cadherin redistribution responses were observed after exposures to different flow patterns for periods of ~ 24 hrs (11,14,30,55). Morphological responses of the HUVEC monolayer were quantified, and the junction protein staining tests are performed to compare the effects of different kind of flow forces on the HUVEC monolayer. Morphology analysis results were consistent with the observations made in in-vivo and relevant in vitro studies. Moreover, junction protein staining results suggests stronger resemblance to in-vivo observation of ECs in disturbed flows; much more so compared to Newtonian flow based experiments in literature (30,37). This is an important result as EC layer junction

integrity has been shown to be a major factor in the development of atherosclerosis (27-31). Our results show that the viscoelastic microfluidic approach may offer a new efficient and effective method in research involving shear responses of endothelial cells especially as it relates to disturbed flows and atherosclerosis.

2.2 Experimental

2.2.1 Microfluidic Device Design and Fabrication

The PDMS (Polydimethylsiloxane) microchannel devices are fabricated using a rapid prototyping technique called soft lithography (56,57). The channel feature is first designed and drawn using the AutoCAD software, and the resultant graphic file (.dxf) is converted to an appropriate file format (.gbr) using the conversion software such as LinkCAD, and then send to an outside vendor (CAD/ART services) to generate transparency film photomasks. The channel feature is printed at 20,000 dpi onto the transparency film, giving a feature resolution of about 1.27μm. This mask is used to create SU-8 master molds on the silicon wafers, with channel features appearing as positive reliefs (56,57). PDMS Prepolymer (Sylgard 184, Dow-Corning) at a 1:10 curing agent-to-base ratio was cast against the master mold to form a negative replica of microchannels, then cured at 60ºC overnight. Then, the PDMS channel is cut out of the master mold, and access holes to microchannels were punched using both 1.5 mm (pump tubing side) and 6mm (reservoir side) Biopsy punches (Miltex). This PDMS channel piece is bonded to another substrate PDMS piece after exposing the contacting surfaces to oxygen plasma for 30 seconds (Plasma Prep II, SPI Supply; for 3 minutes, at 250 mili-Torr vacuum, full power). After bonding, the soft tubing (1/32”ID, Tygon) is connect to the tubing side access hole with a 18 gage blunt needle and glued tight with epoxy adhesive. A larger reservoir cylindrical structure piece is cut out from 50 ml conical, and

glued above the reservoir side holes to increase the volume of reservoir. A finished device is shown in **Figure 2.1A**.

Microchannel geometries have been designed and tested with three major considerations in mind. First, the channel geometry should have sudden converging and diverging shapes, which promote viscoelastic flow instability when using viscoelastic working fluids (45,46). Second, although not mimicking, the channel geometry features should have some resemblance to diseased, narrowing vessel shapes (stenosis) (58,59), as a result of atherosclerosis lesion growth. As the sudden narrowing of the blood vessel are critical for the complex hemodynamic conditions and lead to additional effects on the functions of EC monolayer (30,60-62). Third, the microchannel must allow efficient EC seeding, monolayer growth and experimental observation. Through numerous iterations two channel shapes were finalized as shown in **Figure 2.1B&C.** Channel feature design one (iteration #18, **Figure 2.1B**) has 5 rectangular channels (~ 671 μm x 440 μm) with fluid entering from a narrow inlets (width ~ 70 μm, designed 50 μm, enlarged due to lithography process) and flow diagonally across the chamber and exits through another narrow chamber; called "**diagonal flow**" design. Channel feature design two (iteration #19, **Figure 2.1C**) has 4 rectangular channels (~ 671 μm x 440 μm) with fluid entering from a narrow bottom inlet, turn and cross the chamber, and turn back toward the bottom and exit through another narrow outlet (width ~ 70 μm, designed 50 μm); called "**turn-around flow**" design. Outside the testing chamber area, both microchannel designs consist of long straight channels of ~671 μm in width. Channel heights for current EC shearing tests are ~66 μm.

2.2.2 Modified EC Culturing Media:

High molecular weight polyacrylamide (MW=18,000,000) was the polymer of choice in various literatures to provide viscoelastic mixture solution (44-46); and was selected as the polymer to mix with the EC culturing media to form a modified culturing media to generate viscoelastic flow instabilities and to support culturing of EC cells in the

microchannel devices. Also, in order to better simulate the flow condition within the blood vessel this viscoelastic mixture of polyacrylamide polymer and EC culturing media should have comparable viscoelastic property to that of blood. Mainly, the apparent dynamic viscosity of this mixture should be similar to that of the human blood in the shear rate range of the cell shearing tests.

Early in the preliminary work, multiple concentration ratios of the polyacrylamide polymers were mixed and the dynamic viscosity measurements were performed with an AR1000 rheometer (TA Instruments), with temperature control capability. Temperature setting was set to 37ºC to simulate the blood temperature and cell culturing/testing environment. **Figure 2.2** shows the apparent dynamic viscosity test results for the two concentrations of polyacrylamide polymer in EC Culture media (EGM-2, Lonza) (0.05% and 0.1% by weight) at a wide range of shear rates. The apparent viscosity data point at each shear rate is the average of 3 measurements at same shear rate (programmed automatically). The dynamic shear rate of the human blood is plotted using an equation obtained from literature (50); average of 9 adult blood samples were measured to acquire this curve, with average hematocrit (Hct.: percentage by volume of packed red blood cells) count = 44%. It was observed that the 0.1 % wt. solution of polyacrylamide in EC Culturing media fit the dynamic apparent viscosity of human blood reasonably well in the range of shearing rate generally experienced in EC cell shearing tests. Other percentages (0.01%, 0.05%, 0.15%, and 0.2%) did not fit the curve well. As a result, 0.1% wt. solution of polyacrylamide in EC Culturing media was chosen as the working solution for viscoelastic cell shearing tests. Figure shows, in the range of shear rate applied for varies EC cell shearing (~100-1000 sec^{-1}), the viscosity of the viscoelastic modified media is about 4 times the value of pure culture media (~1 cps) used for Newtonian flow test. These formulations and values are used throughout this study to regulate the flow rate and shear stress applied to the EC cells.

In addition to the dynamic viscosity profile, another critical parameter in determining viscoelastic property of a fluid is the characteristic relaxation time (λ) (40-

42). The tendency for a viscoelastic flow to become unstable is controlled by the dimensionless Weissenberg number:

$$Wi = \nabla V \times \lambda$$

where ∇V is the shear rate and λ the characteristic polymer relaxation time (45); and a value of ≥ 0.5 is generally consider to be the value at which flows become unstable (45-46). For Newtonian fluids, the relaxation time approaches 0 so it does not reach the region of viscoelastic unstable flow. For 0.1% Polyacrylamide solution (in water), the relaxation time is estimated to be about 7 ms by invoking the Zimm relaxation time model (63), with intrinsic viscosity determined from the molecular weight using the Mark-Houwink relationship (64-65) (See supporting information for estimation calculation). While, the relaxation time for blood depends on flow geometry, shear rate and health; it ranges from ~ 0.5 ms for normal blood to as big as ~20 ms for blood with sickle cell disease (49). So while 0.1% polyacrylamide added media does not mimic blood perfectly, it should be considered an adequate working fluid in the viscoelastic shear tests.

Before using the polyacrylamide polymer added EC culturing media to perform shearing tests on EC cell layers in the microchannel devices, this working liquid needed to be tested for its compatibility with EC cells. This is important because the EC cell shearing tests generally last over 24 hours, and the cultured EC cell need to be pre-conditioned with polymer added culture media for extended times before the shearing test; if the EC cells reacts negatively toward the polymer added media even without the additional mechanical effects introduced from viscoelastic flow instability, the shearing test becomes impossible to evaluate. The compatibility test was performed by simply culturing the EC cells for extended time with both pure EC culture media (as control) and varies concentrations of polyacrylamide polymer added media. We observed the resultant EC cells growth, proliferation, and morphology. Mechanical effects of the flow were eliminated by performing the EC cell static culturing inside T-25 flasks. HUVEC cells (Human umbilical Vein Endothelial Cells) were seeded into three different flasks at the same seeding density and amount, and cultured under same conditions in the

incubator (37ºC, 95% Relative Humidity, and 5% CO2) with (a) pure EC culture media, (b) 0.1% Polyacrylamide added media. 4 ml of media (or polymer media) were refreshed every 48 hours, and the cells flasks were checked and imaged every day. The observations (images not shown) revealed that there were little if any differences between the EC cells appearance, proliferation, and time needed to reach confluence. EC cells continue to grow and proliferate in each flask, and later could be passage again and continued to grow into the next generation in very similar manners. This observation result was consistent with the osmolarity measurements for each of culture media solutions, as the dilute polymer/media solutions (at 0.1% wt. and 0.25% wt.) have basically the same osmolarity value as the pure EC culture media (~270). Osmolarity is an important indicator of how fluid penetrates into or out of the cell membrane. As a result of this and other preliminary tests, it was determined with good confidence that the polyacrylamide added EC culture media, at the concentration level used in the EC cell shear tests (~0.1%), is very compatible with the EC cells.

2.2.3 HUVEC Layer Culturing in Microchannel Device

The microchannel device is plasma oxygen treated for 20 minutes (Plasma Prep II, SPI Supply; for 15 minutes, at 250 mili-Torr vacuum, full power) to generate a hydrophilic channel surface; this greatly reduces the possibility of trapped bubbles during the solution filling process, and is especially important since the chamber geometries make it prone to trapped air bubbles. Next, the device is sterilized for ~30 minutes in a UV chamber. Then, the microchannel is treated with fibronectin, a common extracellular matrix protein to enhance the attachment and growth of the ECs to the microchannel. Pre-mixed fibronectin solution (concentration: 100μg/ml) in phosphate buffered saline (PBS, GIBCO, Invitrogen Co.) is applied to the microchannel by first introducing it to the device reservoir; a 3 ml syringe (BD Plastic) equipped with 18 gage needle is connected to the silicon tubing of the device, and used as a suction device to pull the fibronectin solution into the microchannel from the reservoir. Then, the tubing is clamped and the device is kept in the incubator (37ºC, 5% CO_2, 100% humidity) for 4 hrs. Following

incubation, the fibronectin solution is replaced by EC culturing media (EGM-2, Lonza) following the same suction procedure. To fully purge the fibronectin solution, EC media is pumped through the microchannel device for ~30 minutes (at the rate of 100 µl/hr) using a syringe pump (KD Scientific). The microchannel is kept wet during all liquid changing process.

HUVEC cells suspended in media solution (~10^6 cells/ml) are introduced into the microchannel from the reservoir through gravity-driven flow; and EC distribution within the microchannel is checked through microscopy. After desired seeding is obtained, the silicon tubing is clamped to prevent further solution flow. The seeded microchannel device is placed into the incubator for ~90 minutes for ECs to settle and attach to the bottom of the microchannel. After inspection for satisfactory cell attachment condition, slow perfusion of the fresh EC media is performed by connecting the silicon tubing with a 3 ml syringe that is secured on a syringe pump (KD scientific), which is also placed in the incubator. Slow suction perfusion (withdraw mode of syringe pump) is aimed to provide the ECs with fresh media from the reservoir side while preventing excess flow which could pre-maturely shear the cell and affect the result of future shearing tests. The pump suction flow rate is set at (30-35 µl/hr). The reservoir is exchanged with fresh media every 24 hr and EC proliferation is check daily. It usually take about 36-72 hrs from seeding for a confluent EC monolayer to form.

2.2.4 HUVEC Layer Shearing and Flow Characterization

Once the HUVEC layer becomes confluent, it is removed from the perfusion culture syringe pump and perfusion culture 3mL syringe; and reconnected with a larger syringe holding more EC media (See **Figure 2.1D**) for extended, high flow rate shearing of the HUVEC layer. Then the syringe is again secured on the syringe pump (KD scientific), and place back in the incubator to begin high flow rate shear test. To better simulate human physiology, the pump is set to push mode instead of suction mode used

in the perfusion culture period, to prevent the possible large negative normal pressure gradient associated with high flow rate suction flow in the microchannel.

The high flow shearing tests last for 24 hrs. The shearing sample are check once or twice during the period (at 8th, 12th or 16th hour) to first, ensure the success of the test; since bubble growth is a common occurrence in microchannel and it wipes out the EC layers passing through the microchannel; and second, if necessary, to supply additional media into the syringe for the extended test period. When the 24 hour shear test is finished successfully, microchannel devices are placed under a microscope (TE300, Nikon) under phase contrast mode with 10 x magnification objective, and imaged using a Simple PCI software (Compix Inc.) driven digital camera (ORCA-OR, Hamamatsu) attached to the microscope driven by Simple PCI software (Compix Inc.) for data analysis.

It is important to set a clear flow reference for HUVEC shearing tests. Due to the complex geometry experienced by the flow in the chambers area of the microchannels (with "diagonal" and "turn-around" flow), a general flow reference is set at the long, straight section of the microchannels (**Figure 2.1 B & C**) which is the same for each channel design, with rectangular cross-sections of (~ 671 μm width x 66 μm height). With this reference geometry, application of different flow rates can be easily converted into reference average flow speeds ($\boldsymbol{U_{ref}}$) simply by dividing the flow rate with the reference cross section area. And reference wall shear rate ($\nabla V_{wall-ref}$) can be calculated, with fully developed parallel plate laminar models (11,17,66), since channel width (w) is much larger than channel height (h):

$$\nabla V_{wall-ref} = \frac{6Q}{h^2 w} \qquad \text{(Eq. 1)}$$

where Q is the working fluid flow rate controlled by the syringe pump. And reference wall shear stress ($\tau_{wall-ref}$) then can also simply be calculated by multiplying the wall shear stress with the working fluid viscosity (μ):

$$\tau_{wall-ref} = \mu \times \nabla V_{wall-ref} = \frac{\mu 6Q}{h^2 w} \qquad \text{(Eq. 2)}$$

Similarly, reference Reynolds numbers (Re_{ref}) can be calculated by the following equation (66):

$$\mathrm{Re}_{ref} = \frac{2\rho Q}{\mu(h+b)} \qquad \text{(Eq. 3)}$$

where ρ is the density of the working fluid. Reference Reynolds number Re_{ref} is used less frequently in this work to compare different test conditions due to the fact that the polyacrylamide modified EC media has much higher viscosity value (~4 times at the common range of testing condition, see **Figure 2**) compared to regular EC media and similar density, which will reduce Re_{ref} even with similar flow conditions and shear rates.

Flow visualization is achieved by adding 1 μm dyed polystyrene microparticle suspension solution (Polysciences, Inc.) or 0.5 μm fluorescent polymer microsphere (Thermo Scientific Inc.) solution into the working fluid (~1% by volume). These small particles are carried by the flow stream and present clear indication of the flow profile for both still image and continuous video acquisition. Fluorescent microspheres make better streamline images, but sometimes fluorescent microspheres are attached to the channel wall and their illumination block out the main channel flow, making it more difficult to observe the flow profiles.

2.2.5 Junction Adherence Protein (VE-Cadherin) staining test procedure

Following shearing test and imaging, the HUVEC sample were first washed with PBS by filling the reservoir with PBS and have flow through the microchannel via gravity-driven forces by placing the end of the silicon tube at a lower elevation. PBS is allowed to flow for 5 minute to purge the remaining media the microchannel. Next, HUVEC samples were fixed in 4.0% paraformaldehyde in PBS for 30 min (same method

as PBS wash is used to introduce paraformaldehyde solution into the microchannel, and then allowed to sit for 30 minutes). This is followed by another PBS wash. Then, the HUVEC sample is membrane permeabilized with 0.2% Triton X-100 in PBS for 10 min (same flow in method), followed by another PBS wash. Next, sample is treated by 1.5% Bovine Serum Albumin (BSA, Sigma-Aldrich) in PBS solution for one hour to block nonspecific binding; followed by another PBS wash. Next, the HUVEC sample is treated with anti-cadherin protein (VE-cadherin(C-19), Santa Cruz Biotechnology) in PBS solution (0.8 ug/ml) for one hour, followed by another PBS wash. At last, HUVEC sample is treated with fluorescent secondary antibody (Alexa Fluor® 488 donkey anti-goat IgG (H+L), Invitrogen) in PBS solution (2 ug/ml) for one hour in dark. Then, the sample is washed again with PBS and is ready for fluorescence imaging. Fluorescence microscopy were performed using a microscope (TE300, Nikon) under phase contrast mode with several different magnification objective (10x, 20x, 40x), and FITC fluorescence filter, using a Simple PCI software (Compix Inc.) driven digital camera (ORCA-OR, Hamamatsu) attached to the microscope driven by Simple PCI software (Compix Inc.) for data analysis.

2.3 Results and Discussion

2.3.1 Observation: Newtonian and Viscoelastic Unstable Flow in Microchannels

A design objective of this work is to accommodate both Newtonian and Viscoelastic unstable flow in the same micro fluidic device. Comparison between these two flow patterns is an important step before evaluating the morphological response of the HUVEC layer toward the shear stress generated by these flows.

Observations of Newtonian flow by pumping pure EC culture media through the chamber at various flow rates inside a reasonable range for cell shear tests showed many classic characteristics of low Reynolds number laminar flow in microchannel: stable flow profile remain basically unchanged throughout the flow range tested: from cell perfusion flow rate of about 30 µL/hr ($\boldsymbol{U_{ref}}$ = 0.19 mm/sec, $\nabla V_{wall-ref}$ = 17.34 sec^{-1}, $\tau_{wall-ref}$ = 0.174 dyn/cm^2, Re_{ref} ~ 0.0285) to the highest end flow rate for shear testing of 3 ml/hr ($\boldsymbol{U_{ref}}$ = 19 mm/sec, $\nabla V_{wall-ref}$ = 1733.9 sec^{-1}, $\tau_{wall-ref}$ = 17.24 dyn/cm^2, Re_{ref} ~ 2.285), even as the particle velocity increases with the flow rate along these same flow paths. The Newtonian flow results are the same for both "diagonal flow" design and "turn-around" flow design. **Figure 2.3A** shows the image of the flow profile for "diagonal flow" design at flow rate equal to 1.8 ml/hr ($\boldsymbol{U_{ref}}$ = 11.44 mm/sec, Re_{ref} ~ 1.37), and **Figure 2.3B** shows the image of the flow profile for "turn-around flow" design at flow rate = 1.5 ml/hr ($\boldsymbol{U_{ref}}$ = 9.54 mm/sec, Re_{ref} ~ 1.142).

Since the Newtonian flow profile stay the same throughout the tested range of flow rates. It can be used as the stable reference of flow direction for cell morphology analysis against unstable flow pattern generated by the viscoelastic media. In **Figure 2.3A**, the dotted rectangular area within the "diagonal flow" chamber represents a region used in cell morphology analysis where the general Newtonian flow could be considered flow in one uniform diagonal direction. The angle of the diagonal flow direction will be used as reference angle 0º when analyzing the HUVEC alignment to flow. Similarly in **Figure 2.3B**, the dotted rectangular represent an analysis area in the "turn-around" design chambers where the Newtonian flow could be generally considered straight from left to right.

In contrast, when the 0.1% polyacrylamide is added to the EC media, the flow is no longer stable as the flow rate is increased, and shows a very different flow characteristics when compare to the Newtonian flow. The increase in flow instability in both microchannel designs are characterized by the following observation: First, the flow pattern start to become unstable and stream lines undulate as the applied flow rate (and

subsequently $\boldsymbol{U_{ref}}$) is increased. Second, at certain flow rates, small standing vortices start to appear, and the boundary of the vortices are unstable and prone to periodic partial shedding which reduces the size of the primary vortex. The size of the vortices and the frequency of the periodic washout both increase with the applied flow rate. The vortex shedding spread toward the corner of the downstream chamber wall across of the narrow outlet. Third, as the applied flow rate continued to increase, secondary vortices start to appear intermittently at the chamber corners towards the primary vortex washouts direction, although without fixed periods (not every washout toward the corner generates a secondary vortex); its size, intensity, and appearance frequency increases with the applied flow rate. Unlike the primary vortices, the secondary vortices disappear whereas the primary vortices only partially wash out. There seems to be some sort of exchanging interaction between the two vortices when they appear together, and affects the frequency of periodic washouts of the primary vortices; making the flow pattern very complicated to analyze. Unsteady flow patterns at varies applied flow rate are video imaged and frame by frame analysis produce the frequency of the washout for primary vortex for both microchannel designs. **Figure 2.4A-C** shows the time snap shot images showing the maximum growth, shedding toward the wall, and post shedding suppression of the primary vortex in "diagonal flow" design at flow rate of 0.8 ml/hr ($\boldsymbol{U_{ref}}$ = 5.09 mm/sec, $\nabla V_{wall-ref}$ = 462.4 sec^{-1}, $\tau_{wall-ref}$ = 18.5 dyn/cm^2, Re_{ref} ~ 0.152) and **Figure 2.4D** shows the secondary vortex at the same flow rate (not in sequence with A-C). **Figure 2.4E** shows that the primary vortex washout frequency increases near linearly with the applied flow rate. Each data point is gathered from 2 independent tests with ~10 readings for each test. At and above the flow rate = 0.8ml/hr, secondary vortex start to appear intermittently at the downstream corner, and the plotted washout frequency only applies when the secondary vortex is not present. Larger standard deviations shown for higher flow rates suggest the effects of the secondary vortex on the primary vortex frequency, even when it is not seen on the image during data analysis. Similarly, **Figure 2.5A-C** shows the maximum growth, shedding, and suppression of the primary vortex in the "turn-around flow" design at flow rate of 0.75 ml/hr ($\boldsymbol{U_{ref}}$ = 4.77 mm/sec, $\nabla V_{wall-ref}$ = 433.5 sec^{-1}, $\tau_{wall-ref}$ = 17.3 dyn/cm^2, Re_{ref} ~ 0.142) and **Figure 2.5D** shows the

secondary vortex at the same flow rate (Not in sequence to A-C). **Figure 2.5E** also shows the primary vortex shedding frequency increases nearly linearly with the applied flow rate, in the absence of the interrupting secondary vortex. Each data point is gathered from 2 independent tests with ~10 readings for each test. And secondary vortices start to appear intermittently at flow rates of 0.75 ml/hr. Video sequence of the unstable flows is provided as supplemental files. Unstable vortex formations are also reported by Groisman et al (45,46) for viscoelastic flow in microchannel, however, the vortices were not quantified in terms of frequency so comparison is not possible.

Interestingly, if one extends the linear trend of **Figures 2.4E** or **2.5 E** toward frequency = 0 Hz, it seems to point toward a general on-set boundary where flows become viscoelastic unstable. For **Figure 2.4E** ("diagonal flow" design), the rough trend-line equation cross zero at flow rate value of about 0.396 ml/hr, this gives the reference wall shear rate $\nabla V_{wall-ref}$ of about 229 sec^{-1}. With the estimated value of 7 ms for modified polymer relaxation time, the estimated Weissenberg number (*Wi*) at the zero cross is about 1.6; Similar calculations for **Figure 2.5E** ('Turn-around flow" design) gives zero-cross flow rate, reference wall shear rate, and *Wi* values of 0.263 ml/hr, 152 sec^{-1}, and 1. This is in the same order of the general threshold value of 0.5, above which flows are known to become unstable (45,46). Even though the flow could have become unstable even before manifesting vortex shedding, vortex shedding proved to be a good clear indicator of flow instability. The earlier on-set of flow instability and higher wash-out frequency of the "turn-around" flow design may be used to evaluate how different blood vessel geometries in vivo may impact the complex hemodynamic forces and affect the local endothelial function.

2.3.2 HUVEC Monolayer morphology response to Newtonian laminar flow and Viscoelastic unstable flow.

HUVEC layer morphology responses toward the different kind of flow shearing forces were evaluated using two generally used parameters. First, the alignment of the

cell's major axis compared to a reference direction, generally the direction of flow, called Angle of Orientation (AO). AO = 0° indicates a cell aligns perfectly with the direction of flow and AO= 90° is a cell aligns exactly perpendicular to the direction of flow. Second parameter is called the Shape Index (SI), it is a dimensionless parameter measuring the roundness of the cell's outline shape. It s calculated using the following equation:

$$SI = \frac{4\pi A}{P^2} \qquad \text{(Eq 4)}$$

where A is the area of the cell, and parameter is the outline parameter of the cell. The SI ranges from 0 to 1 where 0 is a straight line (maximum elongation) and 1 is a perfect circle shape (no elongation) (11,35,36). Both *AO* and *SI* can be analyzed from the cell images taken in the experimentations using the free image analysis software, ImageJ (NIH). Two options of *SI* calculation can be chosen, first, *SI* can be obtained using the detailed outline perimeter fitting; this often produces higher perimeter values and lower *SI* values. Another option is to obtain SI using the perimeter value of the estimated elliptic shape based on the major and minor axis; the outline is smooth with smaller perimeter values, making the *SI* value larger. In general, these two approaches produce proportionally consistent results. The first option is used in this research.

Images of the confluent HUVEC monolayer are taken at the end of the slow perfusion period for each test; and these images represent the pre-shearing test states of the HUVEC samples. Then after the HUVEC layer samples are successfully shear tested for 24 hours with either stable laminar Newtonian flow or viscoelastic unstable flow, images are taken again to evaluate the changes in cell morphology. For each microchannel design, only the HUVEC cells within the pre-determined reference zone, as shown in **Figure 2.3**, are evaluated using the general reference direction of the flow (arrow, based on stable Newtonian profile) as the reference angle for AO calculation.

For "Diagonal Flow" microchannel, **Figure 2.6A** shows a sample image of the pre-sheared state of HUVEC layer within the reference zone, adjusted to horizontal layout with arrow showing the reference flow direction; **Figure 2.6B** shows a sample

image for the 24-hour Newtonian flow sheared HUVEC layer using applied flow rate of 2.4 ml/hr ($\boldsymbol{U_{ref}}$ = 15.26 mm/sec, $\nabla V_{wall-ref}$ = 1387 sec^{-1}, $\tau_{wall-ref}$ ~ 13.87 dyn/cm^2, Re_{ref} ~ 1.828). This condition gives a moderate value of reference shear stress $\tau_{wall-ref}$ of about 14 dyn/cm^2, well within the general physiological value of (5-40 dyn/cm^2)(3,9,11,13), and similar value used by many researchers. **Figure 2.6C** shows a sample image for the 24-hour viscoelastic unstable flow sheared HUVEC layer using a flow rate of 0.6 ml/hr ($\boldsymbol{U_{ref}}$ = 3.815 mm/sec, $\nabla V_{wall-ref}$ = 346.8 sec^{-1}, $\tau_{wall-ref}$ ~ 13.87 dyn/cm^2, Re_{ref} ~ 0.114). This gives an estimated wall shear stress value $\tau_{wall-ref}$ that is similar to the Newtonian flow shear test. Physiologically, unstable flow regions usually experience higher instantaneous shear stress values than that of stable flow regions (3), but using the similar reference shear stress level gives direct comparisons between the results of different flow regimes. **Figure 2.6 D & E** shows the change in angle of orientation (AO) and shape index (SI) before and after 24 hrs of Newtonian and viscoelastic unstable flow; with error bars being the standard deviation of the data. Shear result data is compiled through 5 successful Newtonian flow shear test (n=5) and 5 unstable flow shear tests (n=5), with about 25-40 cells analyzed per test in reference zone; with pre-shear condition being the pre-shear condition of these successful tests (n=10). The pre-sheared HUVEC generally exhibit a more rounded cell shapes and no clear directionality, as it was developed under slow flow perfusion with minimal amount of shear stress (11). Result for AO shows a clear reduction for 24hr Newtonian shear test compared to pre-sheared HUVEC layer; with significance value $p < 0.01$ (Student's t test); meaning a clear significant change in HUVEC layer morphology toward aligning with the stable, Newtonian flow field. However, for the viscoelastic unstable flow shear test, there is no significant change in AO, suggesting no alignment for HUVEC layer even after 24 hr of unstable flow. The results for SI shows that, for 24-hr Newtonian flow shear test, the SI value also decreased to a significantly lower value ($p < 0.01$). The SI for the viscoelastic unstable flow also decreases to a value similar to that of the result for 24-hr Newtonian shear ($p<0.01$). The standard deviation, however, is much larger reflecting the wider variation of flow patterns in the unstable shear condition.

Similarly for the "Turnaround-Flow" microchannel, **Figure 2.7A** shows a sample image of the pre-sheared state of the HUVEC layer within the reference zone, adjusted to the horizontal layout with arrows showing the reference flow direction; **Figure 2.7B** shows a sample image for the 24-hour Newtonian flow sheared HUVEC layer using an applied flow rate of 2.4 ml/hr ($\boldsymbol{U_{ref}}$ = 15.26 mm/sec, $\nabla V_{wall-ref}$ = 1387 sec^{-1}, $\tau_{wall-ref}$ ~ 13.87 dyn/cm^2, Re_{ref} ~ 1.828). **Figure 2.6C** shows a sample image for the 24-hour viscoelastic unstable flow sheared HUVEC layer using a flow rate of 0.6 ml/hr ($\boldsymbol{U_{ref}}$ = 3.815 mm/sec, $\nabla V_{wall-ref}$ = 346.8 sec^{-1}, $\tau_{wall-ref}$ ~ 13.87 dyn/cm^2, Re_{ref} ~ 0.114). **Figure 2.7 D & E** shows the change in angle of orientation (AO) and shape index (SI) before and after 24 hrs of Newtonian and viscoelastic unstable flow compared to pre-sheared state; with error bars being the standard deviation of the data. Shear result data is also compiled through 5 successful Newtonian flow shear test (n=5) and 5 unstable flow shear tests (n=5), with about 30-40 cells analyzed per test; with pre-shear condition being the pre-shear condition of these successful tests (n=10). Result for the AO shows a clear reduction for the 24hr Newtonian shear test compared to the pre-sheared HUVEC layer ($p < 0.01$) (Student's t test); indicating a clear change in the HUVEC layer morphology toward aligning with the stable, Newtonian flow field. However, for viscoelastic unstable flow shear test, there is again no significant change in AO, suggesting no alignment for HUVEC layer after 24 hr of unstable flow. The results for the SI shows that, for the 24-hr Newtonian flow shear test, the SI value also decreases to a significantly lower value ($p<0.01$). For the viscoelastic unstable flow, the SI again decreased significantly to a value close to that of the result for 24-hr Newtonian shear ($p<0.01$) with a large standard deviation. The statistic analysis do not show

The HUVEC layer morphology response studies using the two microchannel designs show that, for 24-hr Newtonian flow shear conditions, both the AO and SI are significantly reduced consistent with reports by others (9,11,35,36,67,68). This observation is as expected; since it already well established that ECs detect the flow direction and reorient itself toward the direction of stable flow (3,7,8,67).

The viscoelastic unstable flow conditions gave drastically different, results. There was no alignment of the HUVEC layer toward a reference direction (no clear reduction in AO). The unstable, vortex shedding flow, as observed in **Figures 2.4** & **2.5**, provide no set flow direction for the ECs to align them self to resulting in highly random alignment angles and large standard deviations (**Figure 2.6D & 2.7D)**. This non directionality has also been observed by other Newtonian based in-vitro systems that generate disturbed flow by mechanical methods (30,35,37,71). The result for the shape index (SI) is more difficult to reconcile. The smaller SI indicates that the shape of the HUVEC layer cells is no longer rounded. Majority of previous literature on how the SI changes for EC cells under disturbed flow report that ECs remain rounded and not stretched out (30,36,37,71). Only one previous study suggests reduced SI similar to our results (14). This variability suggests that there are qualitative differences among various "unstable" flows. Also notable is the lack of the use of viscoelastic working fluids in previous disturbed flow studies of ECs. A question is, which type of unstable flow and EC response is more physiological. We address this question in the next section.

2.3.4 Junction Protein (VE-Cadherin) Staining Result

To examine the biological impacts of viscoelastic unstable flow on the HUVEC layer, we stained for an adherens junction protein (VE-Cadherin, Vascular Endothelial Cadherin). VE-cadherin plays an important role in regulating paracellular permeability, a key factor in regulating the crossing of larger molecules such as atherosclerosis promoting low density lipidproteins (2,13). Previous studies have also reported significant effects of steady and unsteady shear stress on the junction protein (27-31). **Figure 2.8A** shows a typical VE-cadherin staining result for a confluent HUVEC layer cultured in a T-25 Flask under static condition. **Figure 2.8B** shows VE-cadherin staining for a HUVEC layer after 24 hr of Newtonian shear in a "diagonal flow" design microchannel with an applied flow rate of 2.4 ml/hr ($\boldsymbol{U_{ref}}$ = 15.26 mm/sec, $\nabla V_{wall-ref}$ = 1387 sec^{-1}, $\tau_{wall-ref}$ ~ 13.87 dyn/cm^2, Re_{ref} ~ 1.828). **Figure 2.8 C&D** shows VE-

cadherin staining for HUVECs after 24 hr of unstable flow in a "Turn-around" design microchannel with an applied flow rate of 0.6 ml/hr ($\boldsymbol{U_{ref}}$ = 3.815 mm/sec, $\nabla V_{wall-ref}$ = 346.8 sec^{-1}, $\tau_{wall-ref}$ ~ 13.87 dyn/cm^2, Re_{ref} ~ 0.114). For both Figure A and B, the VE-cadherin protein are concentrated to cell to cell junctions, illuminating around the outline of the cells, indicating good junction integrity. For viscoelastic flow samples in **Figures C & D**, the VE-cadherin protein is in not concentrated in the cell to cell junction, but is spread throughout the cell. This absence of VE- cadherin at the boarders suggests weak junction integrity in this HUVEC layer. This result is significant. The loss of junction protein at the cell to cell boundaries is suggested as a signature of ECs in vivo in disturbed flow regions and has a been a goal of previous disturbed flow research (g4). Miao et al., for example, exposed ECs to 24 hours of disturbed flow generated by an oscillatory pump and noted reduced VE-cadherin at the cell-cell junctions (30). However, the weakening of the VE-cadherin re-created in-vitro was not strongly evident compared to the clear loss of junction proteins in vivo suggesting the "disturbed flow" in this previous report may not be very physiological. In contrast, VE-cadherin staining of ECs exposed to our viscoelastic disturbed flow, as seen in **Figure 2.8 C & D**, is very similar to ECs observed in disturbed flow regions in vivo as characterized by an almost complete absence of VE-cadherin at the cell to cell borders. This high similarity of the viscoelastic instability shearing result to in-vivo results suggest that our viscoelastic unstable flow is applying more physiological mechanical forces to the cell layer compared to many of the previous Newtonian flow driven disturbed flow systems. The more physiological, simple, small size, disturbed flow endothelial cell culture tool opens new possibilities in drug testing platforms (68), microchannel based vascular simulators to study the impact of different blood vessel geometry such as bifurcation, sharp turn, and aneurysm, and stenosis that are highly susceptible to atherosclerosis(6); and test platform for shearing modulated impacts on susceptibilities of EC layer to the attachments of flowing monocytes (54,69), cancer cells (38), or other microparticles (70) in the blood stream.

2.4 Conclusion

We described a simple yet multi-functional microfluidic device and long-chain polymer engineered culture media to perform endothelial cell layer shearing tests under both laminar stable flow and transient, unstable flow patterns. This system simplifies and makes efficient in-vitro techniques for creating and studying unstable flow pattern effects on endothelial cells by eliminating the need for extensive mechanical control and actuation apparatus and greatly reducing the media volumes required. Engineering both the device channel geometry and the viscoelastic properties of the polymer added culturing media were keys to overcoming the common limitations of microfluidic systems in generating complex flow patterns. This in-vitro shear test is envisioned to contribute greatly toward the extensive testing efforts in large scale studies of complex hemodynamic on endothelial cells due to its reagent, equipment, and resource effective nature.

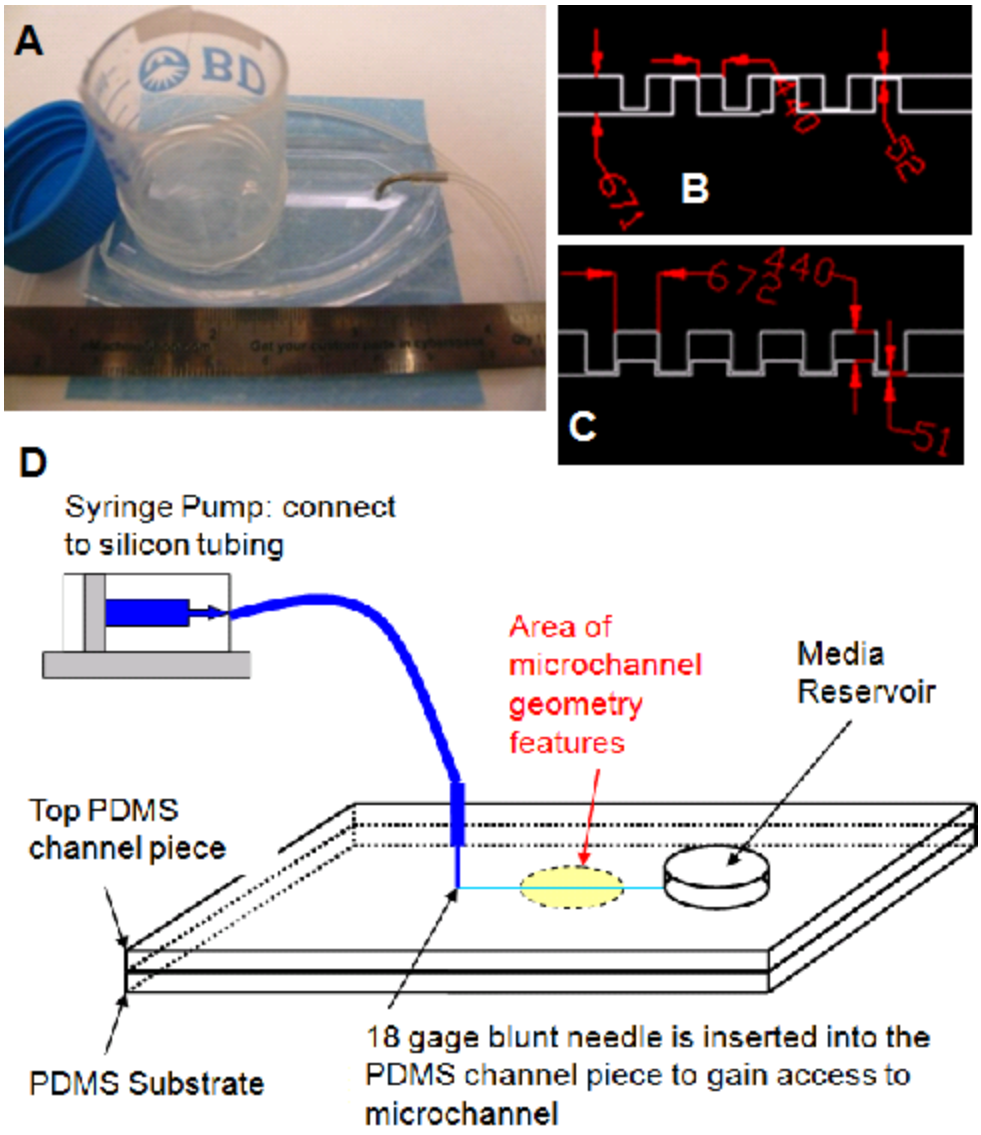

Figure 2.1. A) A complete microchannel device. B) Channel geometry AutoCAD screen for "Diagonal flow' design. Note that narrow neck is designed for 51 µm, but light diffraction during lithography exposure process enlarges the dimension of the master mold feature size. C) Channel geometry AutoCAD screen for "Turn-around flow' design. D) Experimental setup for both HUVEC culturing and shearing.

Fig. 2.2

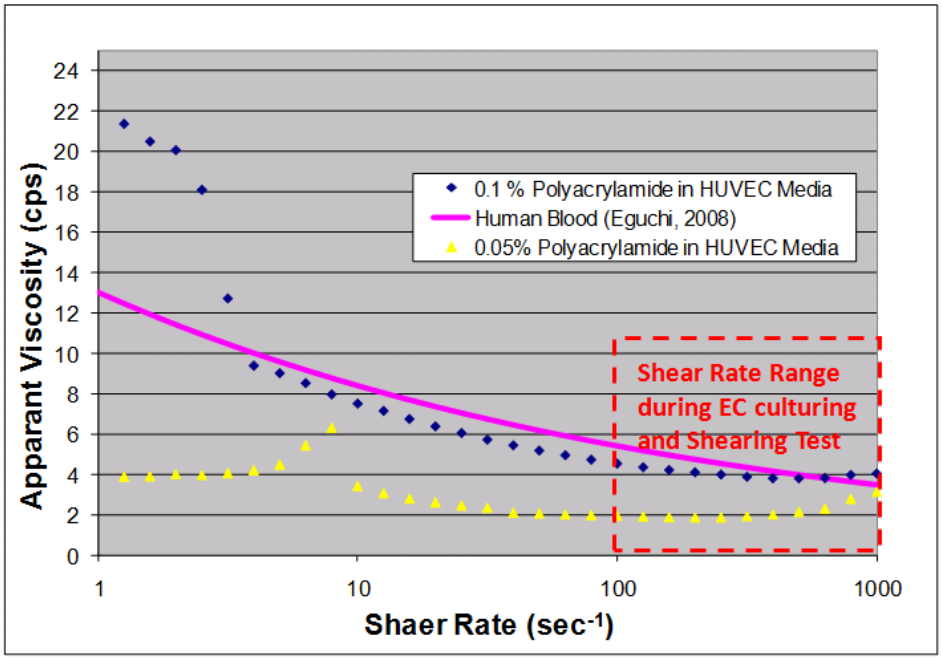

Figure 2.2. The Dynamic viscosity of the 0.1% wt. Polyacrylamide added EC media, as compared with the human blood dynamic viscosity curve developed by Eguchi et al. (2008). In the general shear rate ranges used in viscoelastic HUVEC shearing experiments (~ 100-1000 sec-1), both human blood and modified media have viscosity of about ~ 4 cps, 4 times that of the pure EC media. This ratio is used to adjust flow rate and shear stress test conditions.

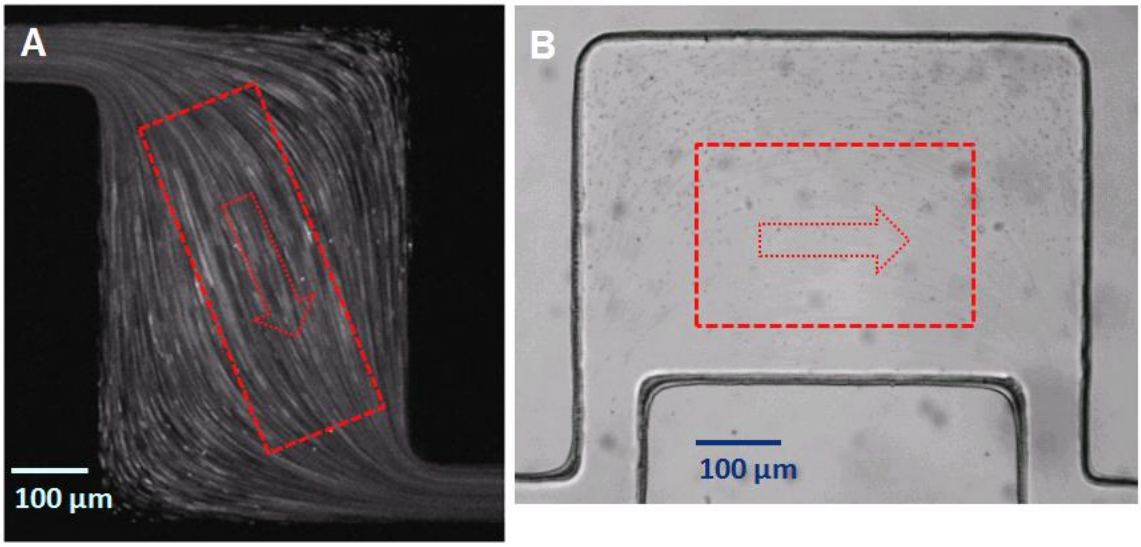

Figure 2.3. Representative images of Newtonian flow profiles by pushing pure EC media through microchannels. A) "Diagonal flow" flow profile with flow rate = 1. 8 ml/hr ($\boldsymbol{U_{ref}}$ = 11.44 mm/sec, Re_{ref} ~ 1.37); and B) 'Turn-around" flow profile with flow rate = 1.5 ml/hr ($\boldsymbol{U_{ref}}$ = 9.54 mm/sec, Re_{ref} ~ 1.142). For both channel design, the Newtonian flow profiles are basically the same from flow rate range as low as 0.03 ml/hr to 3 ml/hr. Red squares are the analysis zones where the flow directions are considered unidirectional in the directions of arrows. During HUVEC morphology analysis, only the cells in the reference zone will be analyzed, using the arrow direction as reference direction.

Fig. 2.4

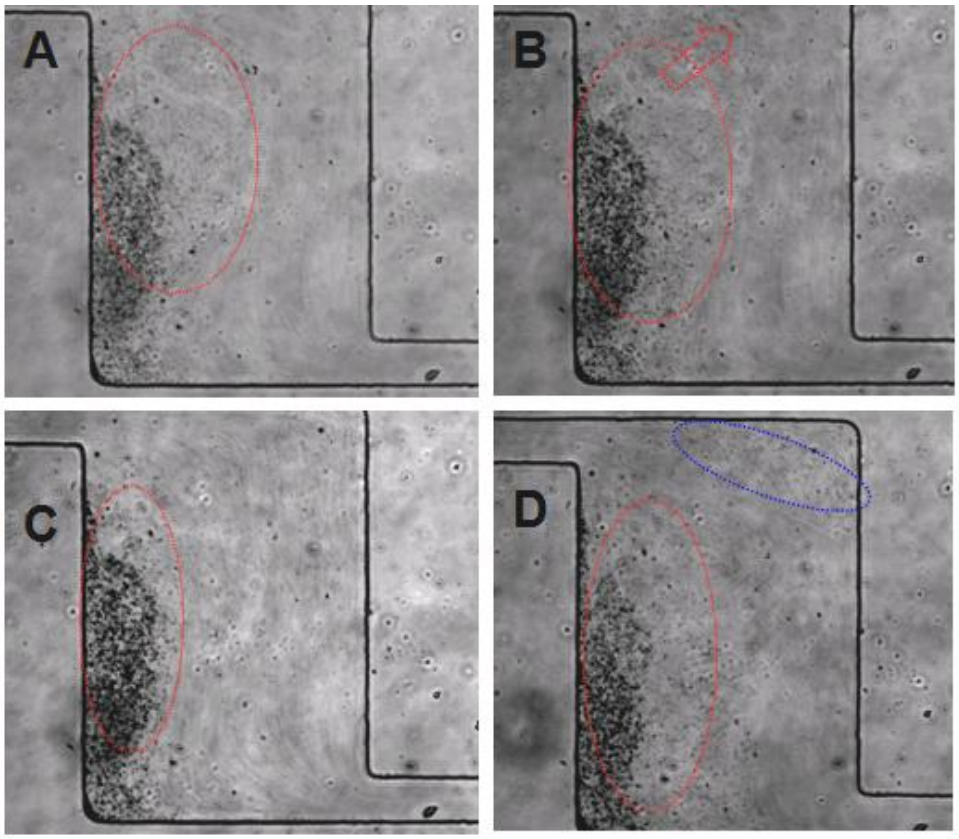
A
B
C
D

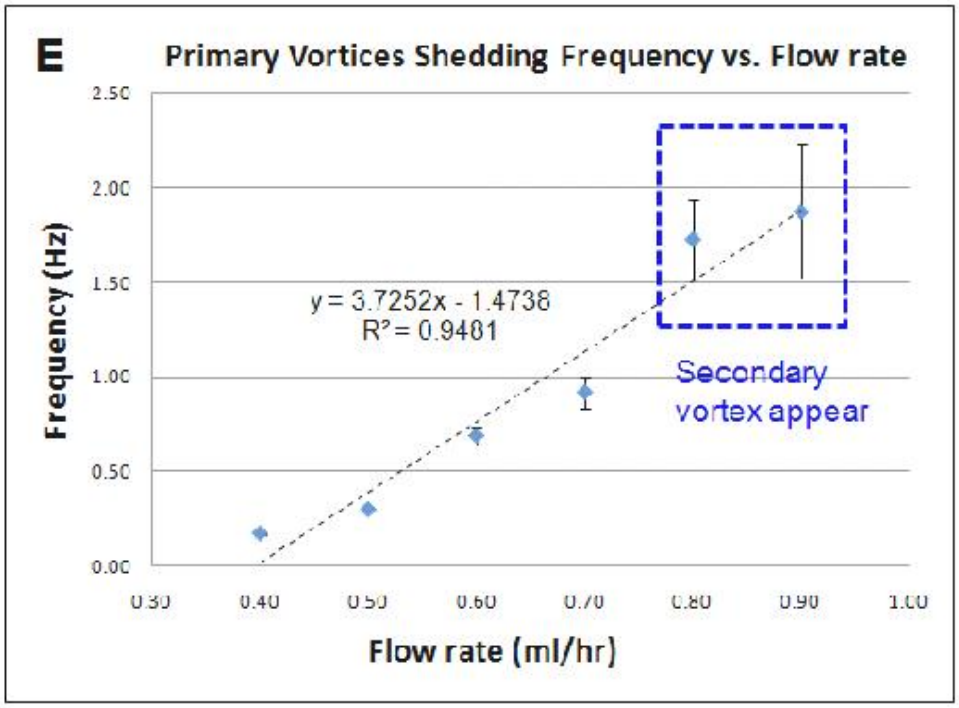
E
Primary Vortices Shedding Frequency vs. Flow rate
Frequency (Hz)
2.50
2.00
1.50
1.00
0.50
0.00
y = 3.7252x - 1.4738
R² = 0.9481
Secondary vortex appear
0.30
0.40
0.50
0.60
0.70
0.80
0.90
1.00
Flow rate (ml/hr)

Figure 2.4. A)-C) Snapshot images of viscoelastic unstable flow in "diagonal flow" design microchannel. Flow rate applied = 0.8 ml/hr ($\boldsymbol{U_{ref}}$ = 5.09 mm/sec, $\nabla V_{wall-ref}$ = 462.4 sec^{-1}, $\tau_{wall-ref}$ = 18.5 dyn/cm^2, Re_{ref} ~ 0.152); fluid flow direction is from bottom right to upper left. Part A shows the primary vortex growing to the maximum size while undulating (red dotted circle indicated a general range of vortex boundary). Followed by Part B, the top part of the vortex washed out in the direction of arrow, toward the upper left corner. And Part C shows the reduction of the primary vortex after partial shedding. D) Sometime the shedding part attaches to the upper-right chamber corner and form a secondary vortex, which disappear after a while (blue circle). E) A chart of the partial shedding frequency of the primary vortices compared to applied flow rate. Note that the period frequency only holds during the absence of the secondary vortices. Blue area shows the flow rate range where secondary vortices appear intermittently. Frequency data here is only analyzed during the absence of secondary vortices.

Figure 2.5

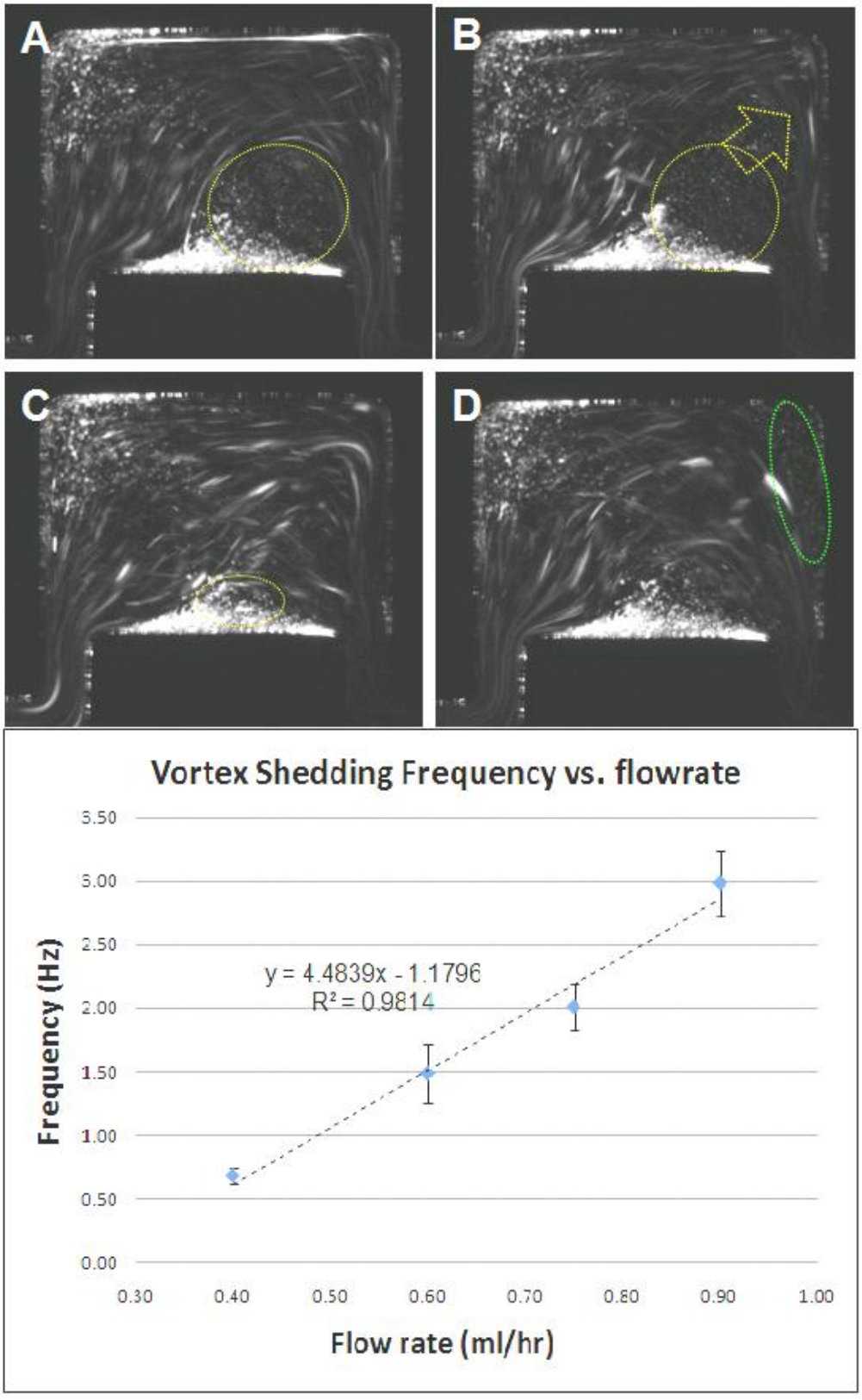
A
B
C
D
Vortex Shedding Frequency vs. flowrate
y = 4.4839x - 1.1796
R² = 0.9814
Frequency (Hz)
Flow rate (ml/hr)
3.50
3.00
2.50
2.00
1.50
1.00
0.50
0.00
0.30
0.40
0.50
0.60
0.70
0.80
0.90
1.00

Figure 2.5. A)-C) Snapshot images of viscoelastic unstable flow in "diagonal flow" design microchannel. Flow rate applied = 0.75 ml/hr ($\boldsymbol{U_{ref}}$ = 4.77 mm/sec, $\nabla V_{wall-ref}$ = 433.5 sec^{-1}, $\tau_{wall-ref}$ = 17.3 dyn/cm^2, Re_{ref} ~ 0.142); fluid flow direction is from bottom left to bottom right. Part A shows the primary vortex growing to the maximum size while undulating (yellow dotted circle indicated a general range of vortex boundary). Followed by Part B, the top part of the vortex washed out in the direction of yellow arrow, toward the upper left corner. And Part C shows the reduction of the primary vortex after partial shedding. D) Sometime the shedding part attaches to the upper-right chamber corner and form a secondary vortex, which disappear after a while (green circle). E) A chart of the partial shedding frequency of the primary vortices compared to applied flow rate. Note that the period frequency only holds during the absence of the secondary vortices. Blue area shows the flow rate range where secondary vortices appear intermittently. Frequency data here is only analyzed during the absence of secondary vortices.

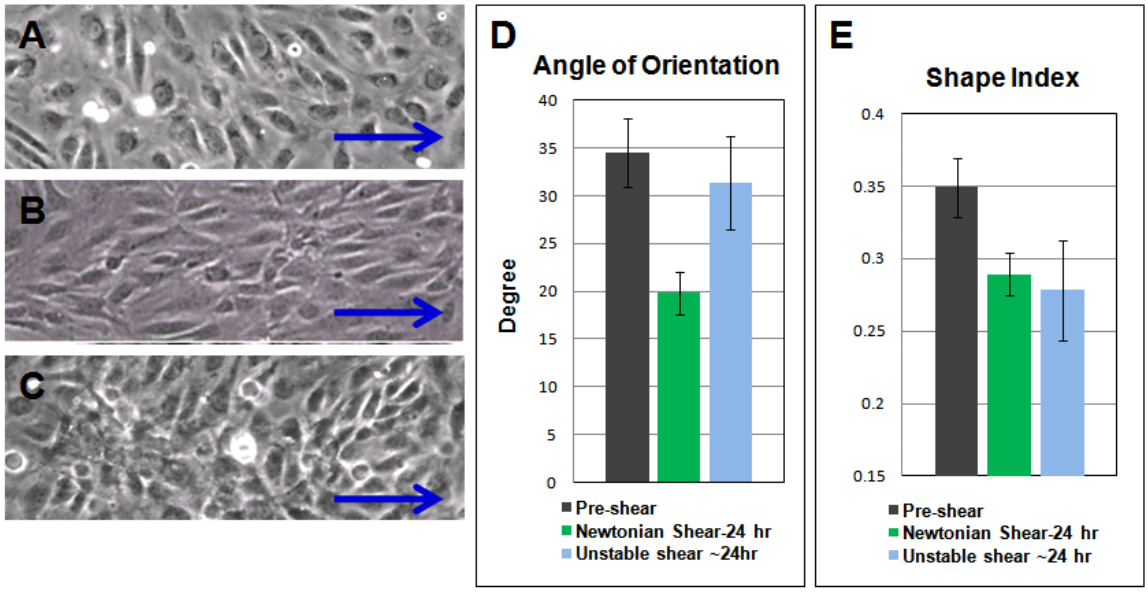

Figure 2.6. The Newtonian laminar and viscoelastic unstable flow results for "Diagonal flow" microchannel design. A) Typical Pre-sheared HUVEC layer image in the analysis zone, blue arrow indicates flow direction. B) Typical HUVEC layer morphology after 24 hours of flow shearing under Newtonian stable flow; most HUVEC are stretched and aligned to flow. C) Typical HUVEC layer morphology after 24 hrs of viscoelastic unstable flow shearing. HUVEC layer do not have directionality nor fixed cell shape. D) Tabulated data for HUVEC layer Angle of Orientation (AO). Significant reduction of angle of orientation is observed for Newtonian sheared HUVEC layer. ($p < 0.01$). There is no significant reduction of unstable flow sheared HUVEC layer. E) Tabulated data for HUVEC layer Shape Index. Significant reductions of Shape Index are observed for both Newtonian sheared and unstable flow sheared HUVEC layer ($p < 0.01$ for both case). However, unstable sheared HUVEC layer has larger variation is data; result in larger standard deviation value.

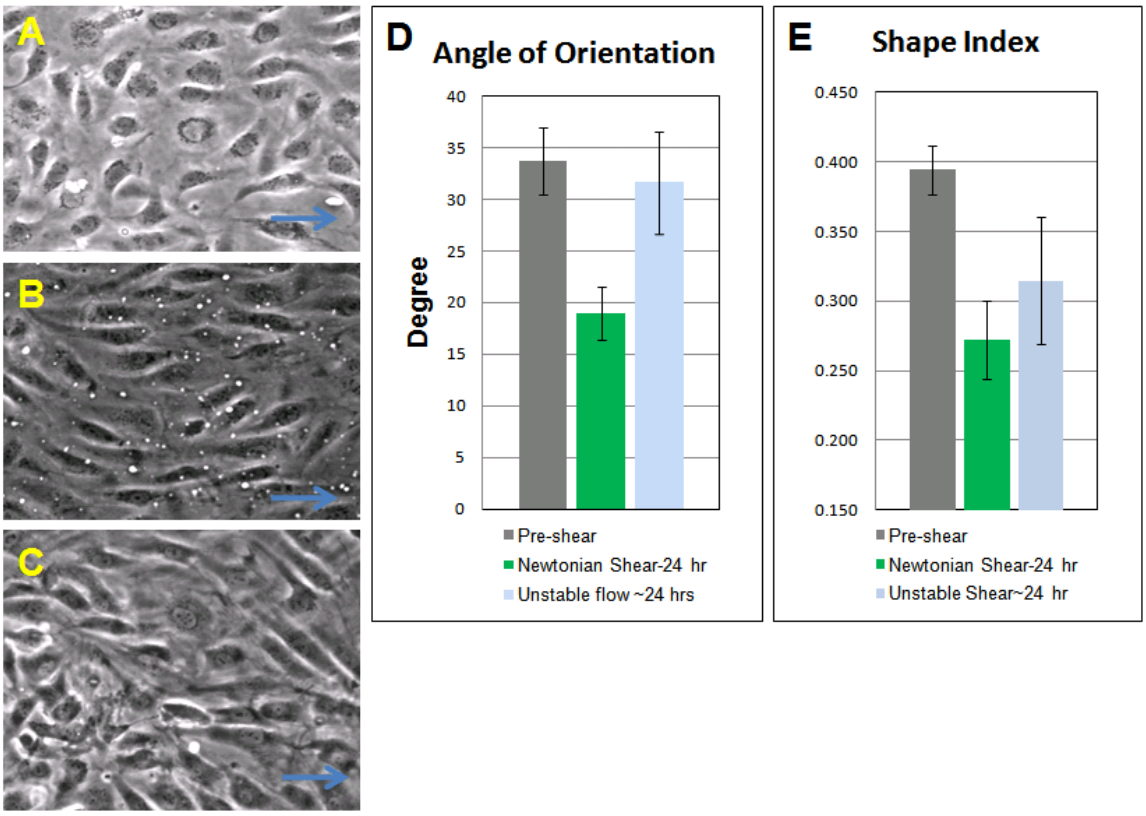

Figure 2.7. The Newtonian laminar and viscoelastic unstable flow results for "Turn-around flow" microchannel design. A) Typical Pre-sheared HUVEC layer image in the analysis zone, blue arrow indicates flow direction. B) Typical HUVEC layer morphology after 24 hours of flow shearing under Newtonian stable flow; most HUVEC are stretched and aligned to flow. C) Typical HUVEC layer morphology after 24 hrs of viscoelastic unstable flow shearing. HUVEC layer do not have directionality nor fixed cell shape. D) Tabulated data for HUVEC layer Angle of Orientation (AO). Significant reduction of AO is observed for Newtonian Sheared HUVEC layer. ($p < 0.01$). There is no significant reduction of AO for unstable flow sheared HUVEC layer. E) Tabulated data for HUVEC layer Shape Index (SI). Significant reduction of SI is observed for both Newtonian sheared and unstable flow sheared HUVEC layer from the pre-sheared state. ($p < 0.01$ for both case). ($n = 5$ individual experiments performed for Newtonian shear and unstable shear)

Figure 2.8

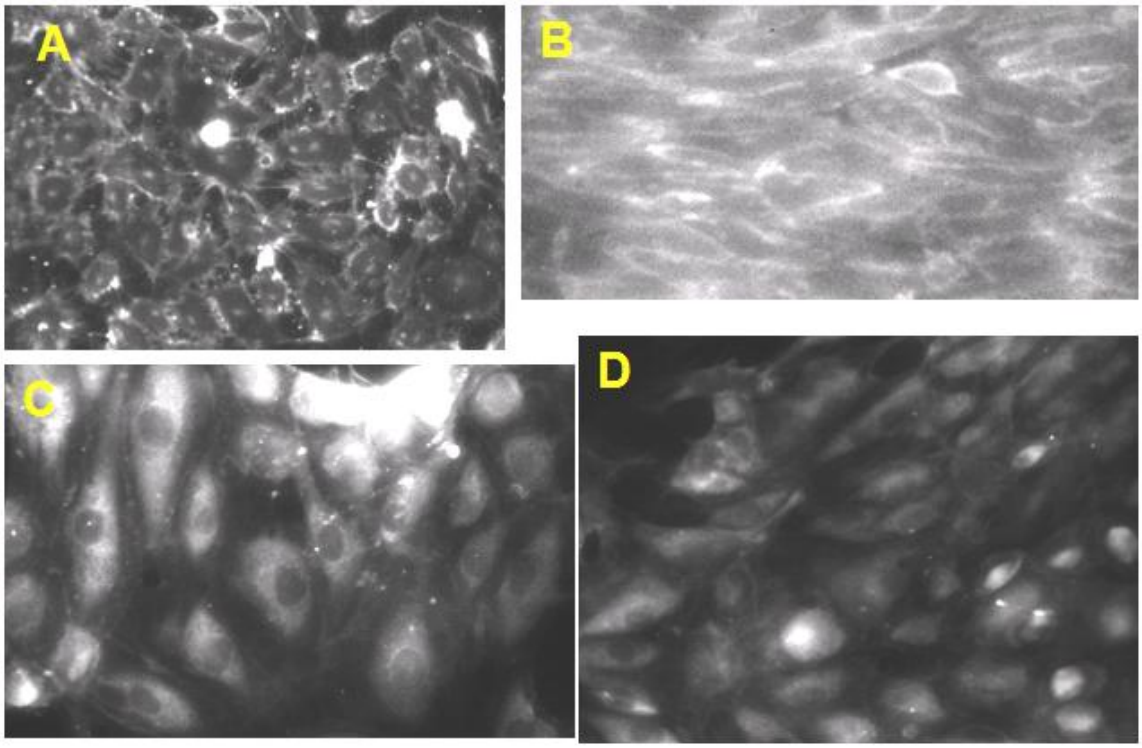

Figure 2.8. VE-Cadherin (Junction Adherens Protein) protein fluorescence staining of HUVEC layers samples under different flow conditions. A) Under Static culture in T-25 Flask, and B) After 24 hr of Newtonian Shear in "Diagonals flow" design microchannel. C) & D) After 24 hrs of viscoelastic unstable flow shear. For both A and B, the VE-cadherin protein are concentrated to cell to cell junction, illuminating around the outline of the cells, indicating good junction integrity. For Viscoelastic flow samples C and D, the VE-cadherin protein in not concentrated in the cell to cell junction, but spread throughout the cells. This absence of the VE- cadherin at the boarders suggest weak junction integrity HUVEC layer.

2.5 References

1 D. C. Schwenke and T. E, Carew, *Circ Res.*, 1988, 62,699-710.

2 S. Weinbaum and S. Chien, *J. Biomech. Eng.*, 1993, 115, 602-610.

3 P. F. Davies, *Physiological Reviews*, 1995, 75, 3, 519-560.

4 J. J Chiu, D. L. Wang, S. Chien, R. Skalak and S. Usami, *J. Biomech. Eng.*, 1998, 120, 2-8.

5 P. F. Davies, C. Shi, N. DePaola, B. P. Helmke and Polacek DC, Ann. *NY Acad. Sci.*, 2001, 947, 7-18.

6 P. F. Davies, *Annals of Biomedical Engineering*, 2008, 36, 4, 563-570.

7 R. M. Nerem, *J. Biomech. Eng.*, 1993, 115, 510-514.

8 S. Colangelo, B. L. Langille and A. I. Gotlieb, *Cell Tissue Res.*, 1994, 278, 235-242.

9 T. K. Hsiai, S. K. Cho, H. M. Honda, S. Hama, M. Navab, L. L. Demer and C. M. Ho, *Ann. Biomed. Eng.*, 2002, 30, 5, 646-656.

10 E. Sho, M. Komatsu, M. Sho, H. Nanjo, T. M. Singh, C. Xu, H. Masuda and C. K. Zarins, *Experimental and Molecular Pathology*, 2003, 75, 1-11.

11 J. W. Song, W. Gu, N. Futai, K. Warner, J. E. Nor and S. Takayama, *Anal. Chem., 2005*, 77, 3993-3999.

12 S. Chien, *Am J Physiol Heart Circ Physiol*, 2007, 292, 1209-1224.

13 D. E. Berardi and J. M. Tarbell, *Cellular and Molecular Bioengineering*, 2009, 2, 3, 320-331.

14 J. J. Chiu, D. L. Wang, S. Chien, R. Skalak and S. Usami, *J. Biomech. Eng.*, 1998, 120, 2-8.

15 C. G. Galbraith, R. Skalak and S. Chien, *Cell Motil. Cytoskel.*, 1998, 40, 317-330.

16 B. Wojciak-Stothard and A. J. Ridley, *J. Cell Biol.*, 2003, 161, 429-439.

17 T. Ohashi and M. Sato, *Fluid Dynamics Research*, 2005, 37, 40–59.

18 G. Helmlinger, B. C. Berk and R. M. Nerem, *Am. J. Physiol.*, 1995, 269, 367-375.

19 Y. C. Boo, J. Hwang, M. Sykes, B. J. Michell, B. E. Kemp, H. Lum and H. Jo, Am. J. Physiol. *Heart Circ. Physiol.*, 2002, 283, H1819-H1828.

20 M. B. Dancu and J. M. Tarbell, *Journal of Biomechanical Engineering*, 2006, 128, 329-334.

21 A. Yee, K. A. Bosworth, D. E. Conway, S. G. Eskin and L. V. McIntire, *Annals of Biomedical Engineering*, 2008, 36, 4, 571-579.

22 B. P. C. Chen, Y. S. Li, Y. H. Zhao, K. D. Chen, S. Li, J. M. Lao, S. Yuan, J. Y. K. Shyy S. and Chien, *Physiol Genomics*, 2001, 7, 55-63.

23 G. Garcia-Cardena, J. Comander, K. R. Anderson, B. B. Blackman and M. A. Gimbrone, *Proc. Natl. Acad. Sci.*, 2001, 98, 4478-4485.

24 Y. Liu, B. P. Chen, M. Lu, Y. Zhu, M. B. Stemerman, S. Chien and J. Y. Shu, *Arterioscler. Thromb. Vasc. Biol.*, 2002, 22, 76-81.

25 D. S. Vara, G. Punshon, K. M. Sales, G. Hamilton and A. M. Seifalian, *Biotechnol. Appl. Biochem.*, 2006, 45, 119-130.

26 N. Wang, H. Miao, Y. S. Li, P. Zhang and J. H. Haga, *Biochem. Biophys. Res. Commun.*, 2006, 341, 1244-1251.

27 H. Jo, R.O. Dull, T. M. Hollis and J. M. Tarbell, *Am. J. Physiol.*,1991, 260, H1992-H1996.

28 H. W. Sill, Y. S. Chang, J. R. Artman, J. A. Frangos, T. M. Hollis and J.M. Tarbell, , *Am. J. Physiol.*,1995, 268, H535-H543.

29 S. Noria, D. B. Cowan, A. I. Gotlieb and B. L. Langille, *Circ. Res. 1999*, 85, 504-514

30 H. Miao, Y. Hu, Yan-Ting Shiu, Suli Yuan, Yihua Zhao, R. Kaunas, Y. Wang, G. Jin, S. Usami and S. Chien, *J Vasc Res*, 2005, 42, 77–89.

31 J. Ukropec, M. K. Hollinger and M. J. Woolkalis, Experimental Cell Research 2002 273, 240–247.

32 S. R. Bussolari, C. F. Dewey Jr., M. A. Gimbrone Jr., Rev. Sci. Instrum., 1982 53(12), 1851-1854.

33 M. Noris, M. Morigi, R. Donadelli, S. Aiello, M. Foppolo, M. Todeschini, S. Orisio, G. Remuzzi and A. Remuzzi, *Circulation Research*, 1995, 76, 536-543.

34 C. Hermann, A. M. Zeiher and S. Dimmeler, *Thromb. Vas. Biol.*, 1997, 17, 3588-3592.

35 K. Ookawa, M. Sato and N. Ohshima, *J. Biomechnics*, 1992, 25, 11, 1321-1328.

36 N. Kataoka, S. Ujita and M. Sato, *Med. Biol. Eng. Comput.*, 1998, 36, 122-128.

37 S. Chien 2008, *Annals of Biomedical Engineering*, 2008, 36, 4, 554-562.

38 J. W. Song, S.P. Cavnar, A. C. Walker, K. E. Luker, M. Gupta, Y. Tung, G. D. Luker and S. Takayama, *PLoS ONE*, 2009, 4, 6, e5756, 1-10.

39 R. G. Larson, *Rheol Acta*, 1992, 31, 213-263.

40 A. Groisman and V. Steinberg, *Nature*, 2000, 405, 53-55.

41 A. Groisman and V. Steinberg, *Nature*, 2001, 410, 905-908

42 B. A. Schiamberg,L. T. Shereda, H. Hu and R. G. Larson, *J. Fluid Mech.*, 2006 ,554, 191–216.

43 T. Burghelea, E. Segre, I. Bar-Joseph, A. Groisman and V. Steinberg, *PHYSICAL REVIEW E*, 2004, 69, 066305: 1-8.

44 H. Y. Gan, Y. C. Lam and N. T. Nguyen, *APPLIED PHYSICS LETTERS*, 2006, 88, 224103:1-3.

45 A. Groisman, M. Enzelberger and S. R. Quake, *Science*, 2003, 300, 955-958.

46 A. Groisman and S. R. Quake, *Phys. Rev. Lett.*, 2004, 92, 9, 094501:1-4.

47 J. Long, A. Undar, K. B. Manning and S. Deutsch, *ASAIO J.*, 2005, 51, 5, 563-566.

48 P. J. Marascalco, S. P. Ritchie, T. A. Snyder, M. V. Kameneva, *ASAIO J.*, 2006, 52, 5, 567-574

49 G. B. Thurston and N. M. Henderson, *Biorheology*, 2006, 43, 729–746

50 Y. Eguchi and T. Karino, *Annals of Biomedical Engineering*, 2008, 36, 4, 545-553.

51 A. Paez A, A. R. Méndez-Cruz, E. Varela, E. Rodriguez, J. Guevara, L. Flores-Romo, L. F. Montaño and F. A. Massó, *Clin Exp Immunol.*, 2005, 141, 3, 449-458.

52 Y. Zeng, Y. Qiao, Y. Zhang, X. Liu, Y. Wang and J. Hu, *Cell Biology International*, 2005, 29, 11, 932-935.

53 G. Dai, S. Vaughn, Y. Zhang, E. T. Wang, G. Garcia-Cardena, and M. A. Gimbrone, Circ. Res., 2007, 101, 723-733.

54 I. Cicha, M. Goppelt-Struebe, A. Yilmaz, W. G. Daniel, and C. D. Garlichs, *Clinical Hemorheology and Microcirculation*, 2008, 39, 1-4, 113-119.

55 I Cicha, K. Beronov, E. L. Ramirez, K. Osterode, M. Goppelt-Struebe, D. Raaz, A. Yilmaz, W. G. Daniel, C. D. Garlichs, *Atherosclerosis*, 2009, 207, 93–102.

56 D. Duffy, J. C. McDonald, O. J. A. Schueller and George M. Whitesides, *Anal. Chem.*, 1998, 70, 4974-4984.

57 G. M. Whitesides, E. Ostuni, S. Takayama, X. Jiang, and D. E. Ingber, *Annu. Rev. Biomed. Eng.*, 2001, 3, 335-373.

58 D. J. Pennell, H. G. Bogren, J. Keegan, 1996, *Heart*, 75, 127-133.

59 T. Giesler, U. Baum, D. Ropers, S. Ulzheimer, E. Wenkel, M. Mennicke, W. Bautz, W. A. Kalender, W. G. Daniel1 and S. Achenbach, *AJR*, 2002, 179, 911-916

60 K. J. Hutchison, E. Karpinski, *J. Biomechanics*, 1985, 18, 4, 285-296.

61 T. Zand, J. J. Nunnari, A. H. Hoffman, B. J. Savilonis, B. MacWilliams, G. Majno, I. Joris, *Am J Pathol.*, 1988, 133, 2, 407-418.

62 S. A. Berger and L-D. Jou, *Annu. Rev. Fluid Mech.*, 2000, 32, 347–382

63 B. H. Zimm, *J. Chem. Phys.*, 1956, 24, 269-278.

64 F. E. Bailey and R. W. Callard, *Polymer Science*, 1959, 1, 1, 56-62.

65 P. S. Virk, *Journal of the American Institute of Chemical Engineers*, 1975, 21, 4, 625-656.

66 S. M. White, Fluid Dynamics, second edition, 1986, McGraw-Hill Inc., 321-325.

67 S. G. Eskin, C. L. Ives, L.V. McIntire and L. T. Navarro, *MICROVASCULAR RESEARCH*, 1984, 28, 87-94.

68 A. M. Malek and S. Izumo, *Journal of Cell Science*, 1996, 109, 713-726.

69 I. Cichaa, K. Beronov, E. L. Ramirez, K. Osterode, M. Goppelt-Struebec, D. Raaz, A. Yilmaza, W. G. Daniel, C. D. Garlichs, *Atherosclerosis*, 2009, 207, 93–102

70 O. C. Farokhzad, A. Khademhosseini, S. Jon, A. Hermmann, J Cheng, C. Chin, A. Kiselyuk, B. Teply, G. Eng and Robert Langer, *Anal. Chem.* 2005, 77, 5453-5459.

71 J. Shao, L. Wu, J. Wu, Y. Zheng, H. Zhao, Q. Jin and J. Zhao, *Lab Chip*, 2009, 9, 3118–3125.

CHAPTER 3

Surface Decorated Polydimethylsiloxane (PDMS) Microspheres of Uniform Size Made by Microfluidics and Crack Patterning

This paper describes a microfluidic method to generate uniform-sized polydimethylsiloxane (PDMS) microspheres over a size range of 85-200 microns, and then form sub-micron patterned features on the surface. Viscous PDMS prepolymer is pushed out of the middle channel of a 3-inlet-1-outlet converging microchannel flanked on each side by flow of an aqueous surfactant solution. The resulting uniform PDMS microsphere size is regulated by adjusting the flow rates of the aqueous sheath solution according to established multi-phase fluid mechanic theories; with potential to further decrease the size of uniform microspheres. To generate lined pattern features, the surface of the PDMS spheres is made brittle through plasma oxidization. Subsequently, application of compression stress induces fractures on the brittle surface layer. The spacing of the fracture patterns on the surface of PDMS microspheres is controlled by the amount of compression strain applied on the microspheres. These crack patterns can be further decorated by coating them with fluorescent protein and gold nanoparticles, which could be further enhanced into gold or silver nanowires. The unique ability to generate controllable selective 3D deposition patterns on PDMS microspheres introduces a new class of microscale functional material, and provides opportunities for multitude of material science and biomedical applications.

3.1 Introduction

Polymeric microspheres are useful as biological micro-carriers[1-6], drug-delivery tools[7-9], cell mimics[10-13], scaffold structures for tissue engineering[14-17], and micro-lenses and high resolution micro display arrays[18-21]. Despite the prevalence of microspheres prepared from many different materials[22-27], there are few reports of generating PDMS microspheres. The unique properties of PDMS, such as chemical stability, optical clarity, gas permeability, adjustable strength & flexibility, and high biological compatibility make it a preferred material for many micro fluidic based biomedical applications. Furthermore, the mechanical and chemical properties of the surface of PDMS can be modified by plasma oxidation for strong bonding and hydrophilic-hydrophobic switching[30]. This surface modification can also be used to create surface patterns by cracking[29,30]. Interestingly, there have been only limited attempts to make PDMS microspheres[19-21,27,31-33], perhaps owing to the extreme high viscosity of its pre-polymer (362 cps)[36], highly adhesive nature of the pre-polymer solution, and the tendency to cure into solid form even at room temperature; these methods in literatures either do not yield uniform sizes, or are unsuitable for stable, high-volume production, as it had been done for other less viscous prepolymers. Due to the fact that many applications of microspheres involving generating 2-D monolayers[18-21] or 3-D scaffolds[14-17] that require the assembly of large numbers of uniform microspheres, mass production of uniform microspheres is a critical measure being sought in this work.

Microfluidic-based techniques for producing polymeric microspheres are generally performed by first producing microdroplets from the pre-polymer liquid using emulsifying two-phase flow; then cure these prepolymer microdroplets into solid microspheres[23-27]. In general, this approach is applied for polymers with relatively low viscosity pre-polymer solutions such as polystyrene[22], hydrogel[23], isobornyl acrylate[24], or sodium alginate[25-26]. Low-viscosity pre-polymer solutions are relatively easy to handle in microchannel devices, enabling the application of oil-in-water types of micro-scale hydrodynamic focusing and droplet emulsification to generate microspheres[28,29]. PDMS,

however, is highly viscous even when diluted by a solvent like toluene to reduce the mixture viscosity[37]. In our work to generate PDMS microsphere by microfluidic methods, this factor, along with other previously mentioned properties of PDMS prepolymer, needed to be accounted for carefully.

Currently there are two main types of microchannel geometries used for microdroplet generation by two-phase emulsifying flow; first is the T-junction types[23,25,28,29,] , and second is the flow focusing types[23,24,26,29,39-49]. In T-junction type of geometry, one immiscible liquid flow perpendicular into a main flow stream of a second immiscible liquid; the column is sheared by the second liquid flow and elongated in the direction of flow until the surface tension force could no longer hold, and the droplet breaks off and the process repeats itself. In a flow focusing design, the flow column of the first immiscible fluid is jointed and sheathed by surrounding second immiscible fluid flows while overall channel narrows toward a narrow orifice downstream. When the flows squeeze through the narrow neck, pressure forces from surrounding second liquid compress the first liquid column and deceases its thickness, and finally the interfacial instability break down the column into microdroplets. Two-phase emulsification flows and droplet formation in both geometries are well studied for working fluids with relatively low viscosities and relatively easy to handle compared to PDMS pre-polymers. However, previous methods and channel geometries need to be modified to adapt to the properties of PDMS prepolymer. Initial studies suggest that the T-Junction geometry designs are not suitable for PDMS prepolymer; it is very adhesive to the channel wall surface when direct contact is made without a secondary fluid layer providing a separation layer; and in two-phase flow, this contact forms a crippling stream of PDMS in the direction of main flow along the wall surface. The droplet break-off characteristics of the T-junction geometry, as shown in previous studies, shows a close contact between the droplet phase fluid and the channel wall at the corner and immediate downstream of the perpendicular intersection[23,28,29], resultant from the pressure of the mainstream secondary fluid. While in most oil-in-water or water–in-oil emulsification flows using non-adhesive working fluid this phenomena does not effects the eventual break-off of the droplets downstream; in the case of PDMS, the pre-polymer will most likely just stay

attached to the channel wall and creep downstream along the wall. The nature of the flow-focusing type geometry design offers a better option for PDMS prepolymer flow, since the secondary immiscible fluid would basically sheath the PDMS prepolymer at the junction and provides a separation layer to keep it away from the channel wall. A commonly used and well studied microchannel based flow-focusing design was presented by Anna et al[39,40,43,48,49], consisting of straight main channel containing three parallel smaller channels, two identical outer channels for sheath fluid and one central channel for the droplet phase fluid, jointing in a square area with a narrow orifice at a distance downstream in the middle the main channel where all fluids are purged out to a wide straight main channel. This design has well-defined geometric parameters and was studied extensively for the underlying mechanism of the flow focusing theory; however, the presences of the narrow orifice with square edges are again problematic when using a highly viscous and adhesive PDMS pre-polymer liquid as the droplet phase liquid. In this design[39], the central channel droplet fluid often comes in contact with the orifice edge when squeezing through the orifice, especially for larger droplet break-off regimes. This contact is again not a major problem in common oil-in-water or water-in-oil emulsification flows with low viscosity, non-adhesive working fluids[39, 40,43,49], where the droplets just bounce off the channel wall on contact; and in many cases it is suggested to use a more viscous fluid for the sheathing fluid than that of the droplet fluid[29], which provides better isolation between the droplet fluid and the channel wall. For PDMS prepolymer droplet flow, the flow focusing geometry must be modified to minimize the opportunity of contact between the prepolymer and any part of the channel wall. Also, the high viscosity of the prepolymer implies high sheathing fluid flow is needed; this suggests the flow focusing geometry design should enhance a smooth converging flow of inner and outer channels; the Anna et al. design with narrow orifice and square edges do not converge the flows smoothly. Designing a proper flow focusing microchannel for PDMS prepolymer is a critical task of this research project.

We have previously used plasma oxidation to modify the mechanical and chemical properties of PDMS surface layer and to introduce fracture patterns on flat PDMS strips[32-33], centimeter-sized cubes, and on millimeter size spheres[31]. Owing to the

fact that the generation of cracks exposes the underlying PDMS that has not been affected by the plasma oxidization; the cracked region on the sphere can have very different surface properties from the un-cracked region on the spheres. This further enables the unique ability of selective deposition of different molecules, such as protein and gold nanoparticles on the linear crack patterns on the surface of PDMS microspheres.

Deposition of micro to nanoscale metal or semi-conductor particle array or wires on varies substrate surface has gain great research interests from researchers in the field of stretchable electronic[50-55], molecular and biosensors[56-57], and optical sensors[58-59]. Surveying of these works reveal that, although the methods of wire generation varies greatly, these deposited wire patterns has been predominantly on two-dimensional (2D) basis over flat substrate; due to the limitation of fabrication methods that are substrate surface based. In this current work, the ability to generate linear crack patterns on PDMS microsphere, and then selectively deposit protein molecule or metal particle which can be enhanced into metal wires is presented as a way to generate nanowire-decorated on microscale objectives such as microspheres.

This manuscript focuses on three aspects of the fabrication of uniform sized surface-decorated PDMS microsphere: (i) Design flow focusing based microchannel design which enable handling of PDMS prepolymer flow and result in uniform PDMS microspheres with high production rate; (ii) Study the potential for decreasing the size-scale of the uniform microspheres; and (iii) decoration of the surface of the microspheres with striped patterns of fluorescence proteins and gold nanoparticles which are enhanced into nanowires; demonstrating their potential for microscale biomedical and material applications. The first two goals are addressed by using micro-fluidic fabrication techniques and two-phase flow focus theory. The third goal is addressed through the application of fracture mechanics combined simultaneously with selective adhesion on the modified surface of microspheres.

3.2 Material and Methods

3.2.1 Micro-fluidic based generation of PDMS microspheres:

Fabrication of the microspheres includes two major steps. First is the formation of micro-droplets consisting of a PDMS pre-polymer solution in the micro-channel devices. Second is the collection and thermal curing of these micro-droplets to form solid PDMS microspheres.

A 3-to-1 converging micro-channel device as shown in **Fig. 1** is used for the production of micro-droplets. The design is a modified form of previously reported flow focusing geometries without the narrow orifice. The smooth impinging angles of the sheathing side channels and the size of each channel were designed to maximize the focusing force of the side channels while maintaining stable flow, while minimize the potential contact of the PDMS prepolymer with the channel wall. The main objective is to maintain the flow focusing characteristics of the Anna design, while tailoring for the highly viscous and adhesive PDMS prepolymer. The channel geometries are cast into a block of PDMS from a negative photo-resist mold deposited on a silicon wafer using the soft-lithography technique[30]. Appropriate access holes are punched through the PDMS block using biopsy punches (1.5mm and 6mm, Miltex Inc.); these connect the end of microchannel geometries to act as channel inlets and outlets. The top PDMS piece with channel-geometry indentations is then bonded to a glass substrate through oxygen plasma treatment to enclose the microchannels and form the device.

To begin the microsphere fabrication, the microchannel device is treated by plasma oxidation to enhance the hydrophilicity of the channels; this enhances the injection of the working liquids and eliminates entrapped air bubbles[38]. The two side channels of the device are connected by soft tubing (1/32”ID, Tygon) to two 60 ml plastic syringes (BD syringe) containing a surfactant solution of 0.1% wt. pluronic F108 (BASF); this is considered to be the “continuous” phase in this two-phase flow process. The middle channel is connected to a 3 ml syringe containing a fresh mixture of toluene

and PDMS pre-polymer solution (10:1 pre-polymer to curing agent) at a desired ratio; this is considered to be the "dispersion" phase owing to the fact that it will be broken up into droplets. Because the PDMS prepolymer mixture starts to cure as soon as the curing agent is added, even at room temperature; for prolonged microdroplet production process, the PDMS mixture will start to cure in the syringe and change its viscosity, affecting the microsphere sizes. Chilling is used as a simple method to maintain the pre-polymer mixture from premature curing: where the PDMS prepolymer-toluene mixture is first kept in -20ºC freezer for 40-60 minutes, and then inserted in the 3 ml syringe just before the test begins.

Two 60 ml syringes are actuated by a single multi-syringe pump (KD Scientific), to ensure the synchronous application of equal flows on both side channels; the middle channel is actuated by a single syringe pump (KD Scientific). Flow rate ramping steps for both continuous phase driving pumps and disperse phase driving pump are controlled carefully to minimize the time needed to initiate convergence of two liquid phases, and to maintain stable focusing flow in the microchannel device. Also, during the flowing process, a solution of 70% ethanol and 30% water is sprayed around syringe and tubing to cool the system and to slow down the self-curing and solidification of PDMS prepolymer. While the toluene-PDMS pre-polymer solution is pumped through the central channel (dispersion phase), the pluronic solution flow from the side channels (continuous phase) impinges on the central stream acting as a sheathing fluid. The interaction between the two streams results in the formation of micro-droplets of the toluene-PDMS pre-polymer solution. An optical microscope (TS-100, Nikon), and attached video camera (Infinity 2, Lumenera Scientific) connected to a host notebook computer are used for microfluidic observation. Image software (Infinity Capture, Lumenera Scientific) records both the video of the droplet formation process at the Y-channel junction and the still images of the resultant PDMS droplets in the outlet reservoir for later analysis.

The low surface energy of the pluronic surfactant solution helps to maintain the PDMS micro-droplets in the outlet reservoir after they have been formed. After being

collected at the outlet reservoir into glass bottles, the droplets are cured and the toluene is evaporated from them by heating in a 60 ºC oven overnight, forming solid PDMS microspheres. In experimental observations, the size of the cured PDMS microspheres do not change significantly compared to the pre-cured microdroplets.

3.2.2 Crack pattern forming on the surface of plasma oxidized PDMS microspheres:

The technique of forming crack patterns on flat PDMS strips and single spheres was first demonstrated by Mills et al[33], and Uchida et al[31]. Parallel aligned cracks along the meridian direction were observed, with the crack spacing controlled by the extent of compression.

In preparation for surface-crack patterning, the cured PDMS microspheres are washed and dispersed in de-ionized water; then the water is drop onto clean glass slide. Evaporation of the water in a 60 ºC oven enables the microspheres to be deposited on a glass slide. This microspheres sample is then exposed to radio-frequency oxygen plasma (Plasma Prep II, SPI Supply; for 5 minutes, at 250 mili-Torr vacuum, full power) to create a stiff, brittle, silica-like thin layer (about 200 nanometers thick[32]) on the surface of the PDMS microspheres. A uniform compressive stress was then applied to the microspheres using a modified version of a custom-built sliding-stage compressor apparatus similar to that used in previous work (as shown in **Figure 3.3A**)[31], and the level of compression strain is controlled by the means of a custom made spacer in the size range of 40-120 micron. The term compression ratio is used to describe the level of strain, and defined as the percentage of the reduction from the original diameter when spheres are compressed. The spacer is manufactured by spin-coating the negative photoresist resin (SU-8, Microchem Inc.) on glass slide, pre-baking at 65ºC hotplate, exposing to ultra-violet (UV) light, then post- baking at 95 ºC to develop the resin film into a hard solid. The spacer is then removed from the glass slide by scalpel, and then baked further in 120 ºC oven to increase the hardness. The spin coating speed and type

of photoresist resin determine the photoresist resin film thickness on the slide, therefore the thickness of the spacer.

3.3 Results and Discussion

3.3.1 Experimental Observation: Size variation of PDMS microspheres

The effects of the two flow parameters on the size of the droplets were examined: the composition of the PDMS solution and the flow rate of the sheathing fluids. The relationships between the diameters of the spheres and side channel (containing the surfactant solution, the continuous phase) flow rates from both 1:1 and 3:1 PDMS-toluene ratio solutions (the disperse phase) are plotted in **Fig 3.2A**. Each data point is averaged from the results of 5 (n=5) individual test result curves under same testing conditions. For each individual test, the results are obtained from averaging the size of 10 randomly selected resultant droplets. The curves show a clear inverse, but non-linear, relation between the continuous phase flow rates within side channels and the resulting diameter of the microspheres. The diameter of the microspheres decrease more quickly with increasing continuous phase flow rate in side channels at the lower range of the flow rate; and the curve flattens out at higher flow rates. Further increasing of continuous phase flow rate outside the plotted range generally results in small but erratic droplet sizes caused by an unstable interface between the two phases. At the other extreme, if the continuous phase flow rate in the side channels was too low beyond the curve, the central PDMS-Toluene stream cannot be pinched off, and the whole system became a steady laminar two-phase continuous flow, forming no droplets. In **Fig. 3.2A** the flow rate of PDMS-Toluene mixture solution in central channel (disperse phase) was maintained at 0.04 ± 0.01 ml/hr for the 1:1 ratio, and 0.08 ± 0.02 ml/hr for 3:1 ratio. However, as mentioned in the previous section, the disperse phase flow rate does not significantly

affect the size of microspheres. As depicted the **Fig. 3.2A**, this technique allows successful mass-production of PDMS microspheres as small as 85μm in diameter with excellent uniformity, especially with a 1:1 PDMS-toluene mixture ratio. Coefficients of variation (CVs) for the sphere diameters between all individual tests are below 2% for all data points of 1:1 ratio curve except at the lowest value of side channels flow (CV= 2.4% at 0.1 ml/min side flow rate). The CVs are below 3.1% for all data points for the 3:1 curve except at the highest side channels flow rate (CV= 4.4% at 1 ml/min side flow rate), where the two-phase flow becomes unstable. This low CV between data points for individual tests suggests that reliable size prediction is expected with high confidence. Finally, the production rate of the microspheres is simply obtained by subtracting the flow rate of PDMS-Toluene mixture (disperse phase) by the volume of resultant microspheres. The stable production rate ranges from less than 0.3 Hz for the largest microspheres (>200 micron diameter), to about 8 to 10 Hz for the smallest spheres (<90 micron), depending on the chosen disperse-phase flow rate. Real-time observation of the experiments agrees approximately with these numbers, example video is provided in supplemental section. (**Supplemental video**)

3.3.2 Experimental Observation: Crack pattern formation

Following the generation of compression crack patterns, the sphere samples are sputtered coated with a thin gold or silver film (SPI module, Gold Coater); and observed using a scanning electronic microscope (SEM, Philips/FEI XL30FEG, University of Michigan). **Figure 3.3B** shows an SEM image of a single PDMS microsphere cracked under a compression ratio of 46.7%. Under compression strain, the crack, the crack patterns are characterized by a round crack pattern on the top of the sphere, indicating the contacting area with the hard flat surface of the compression apparatus. Similar round crack pattern is created on the bottom of the sample. Similar round patterns were observed by Uchida and Uchida Mills et al.[31], termed contact circle. Between the contact circles are parallel straight cracks along the meridian direction. The repeated observations show that the size of the contact circle and the spacing between the parallel

cracks are determined by the compression ratio which and gives a measure of control to the crack patterns that can be generated on PDMS microsphere, also shown in to the previous analysis[31].

3.3.3 Experimental Observation: Selective deposition of fluorescently labeled Bovine Serum Albumin (BSA) and gold nanowires on compression crack pattern:

Deposition of a fluorescent protein on tensile crack patterns on flat PDMS samples surface was first demonstrated by Zhu et al[33]. The procedure to selectively deposit the fluorescent dye (TRITC) labeled Bovine Serum Albumin (TRITC BSA, Sigma-Aldrich) on the compression crack pattern is similar to the cracking process described in the previous materials and methods section. The cured PDMS microspheres are first cleaned of surfactant solution by repeated DI water rinsing, deposited and dried on the clean glass slide, then oxidized in a plasma etcher for 5 minutes (Plasma Prep II, SPI Supply; 250 mili-Torr vacuum, full power) to generate a silica-like hard layer on microsphere surface. Then they are submerged within 5% BSA solution for 30 minutes at room temperature to effectively block the PDMS surface from further protein adhesion. Next, the microspheres are washed, and compression cracks are induced with custom compressor while the microspheres are submerged within a solution of TRITC dye conjugated BSA in PBS (1 mg/ml) for 30 minutes in 37ºC incubator. Following the incubation, the compression load is removed, the microspheres are washed to remove the non-attached fluorescence BSA solution off the surface, and the microspheres sample observed using a Nikon 300 microscope with green excitation / red emission TRITC filter. **Figure 3.4A** show an image of a PDMS microsphere with TRITC BSA deposited in the compression induced crack patterns (compression ratio = 30.3%). The fluorescence illuminated crack patterns shows similar outline features to that of **Figure 3.3B**, including the contact circle at the pole, and the parallel lines, indicating the fluorescence protein bound only to the cracks which expose the under layer PDMS and not on the other parts of PDMS microsphere surface. To further examine the TRITC BSA deposited PDMS microspheres, the sample are imaged using SEM. **Figure 3.4B** shows one such

microsphere sample under SEM imaging. The cracks that contain protein deposits have very distinctive stained appearances compared to the cracks that do not, as in **Fig. 3.3B.** This filled up appearance could be attributed to the aggregation of the protein within the cracks which changes reflective properties under SEM; or caused by the fact that protein attached surface attracts sputtered gold coating differently from blocked PDMS surface.

Deposition of the gold nanowire on the surface of the PDMS microspheres is similar to the deposition of the fluorescence protein in many regards. Cleaned and dried PDMS microsphere sample on the glass slide are first oxidizer treated in a plasma etcher for 5 minutes (Plasma Prep II, SPI Supply; 250 mili-Torr vacuum, full power) to generate a silica-like hard layer on microsphere surface. Then the microspheres are submerged in 3% Pluronic F108 surfactant solution for 50 minutes to block the surface from further protein adhesion. After surface block, the microsphere samples are washed thoroughly. Then, desired compression ratio is applied for 5 second to microsphere sample with the custom apparatus while it is submerged in Nano-Gold particle conjugated bovine serum albumin (Au-BSA) solution (5 nm size, Ted Pella Inc.), after the compression stress is released, the Au-BSA solution is left with the sample for 10 minutes to further attach itself with crack patterns exposed sub-layer PDMS. After the selective attachment of Au-BSA to the crack patterns, the nano-gold particles could be enhanced into gold wire by applying silver and gold enhancement solutions[52]. By repeating applying silver and gold enhancer solutions (silver enhancer LI & Gold enhancer LM, Nanopores Inc.) to the microspheres, silver and gold ions in the solution would be drawn toward the gold nanoparticles that was deposited in the crack patterns and grow on then, eventually into continuous silver, gold, or combination wires. Current protocol call for repeating the enhancer step 4 times on the Au-BSA deposited microspheres in silver – gold – silver-gold enhancement steps, each lasting 15minutes, and sample are washed thoroughly between each step. Following the last enhancements step, the sample is washed and dried, then baked in 120ºC oven to enhance its quality for Scanning Electronic Microscope (SEM, Philips/FEI XL30FEG) observation. **Figure 3.4C** shows a typical PDMS microsphere sample with enhanced gold nanowire lined along the expected parallel crack patterns similar to that of **Fig. 3.3B** along meridian direction, the surface without the

cracks are basically smooth and clean. A few small gold derbies are suspected to be either grown from small Au-BSA deposits that were attached to the microsphere surface despite the surfactant solution blocking. It is also possible that these are the result of self-nucleation of the gold or silver ions in the enhancer solution, as mentioned by the manufactures. Improved blocking process and/or repeating enhancer steps is expected to improve the cleanness of the nanoscale gold wires PDMS microsphere surface even more. Current enhancement protocols produce wire thickness of about **300-500 nm**; potentially, by increasing the silver and gold enhancer steps, the wire size can be increased. Finally, utilizing the Energy Dispersive Spectroscopy (EDS) system and the Genesis software equipped on the SEM microscope, X-ray spectrum of the sample surface was performed to identify the chemical species on the gold wire lined microsphere surface. **Figure 3.4D** clearly shows the presence of gold traces (above the background noises) along the imaged gold wires; confirming their existences. The lower portion of the figure shows the counted peaks of each of the species detected from the bright-field image, which includes Gold (Au), Oxygen (O), Silicon (Si), Sodium (Na) and Carbon (C). The Si, O and C are sourced from the oxidized PDMS surface. The presences of the Na is left from the Phosphate-Buffered Saline (PBS, GIBCO, Invitrogen Co.) used to wash the sample beside using DI water.

3.3.4 Discussion

Several authors had studied the fundamental mechanism of flow focusing type of the microfluidic device of varies designs; and identified some important parameters, in forms of dimensionless groups, that effects the size, production rate, and size uniformity of the resultant droplets. Since the current microchannel design is modified from the previously studied flow-focusing type of geometry, and one of the main objective of current research is to generate uniform, smaller PDMS microsphere beyond the current size order of 100 um in diameter; it is important to compare the current experimental results with the existing theories to gain some essential relevant physical fundamentals of

the current design; and potentially utilizes them toward future attempts in generating smaller PDMS microspheres.

Early works by Anna et al. on a flow focusing geometry design, with two outside continuous phase flow (oil) and an inside disperse phase flow (water) being forced through small downstream orifice[39], developed a phase diagram in which it was described that, for two immiscible liquids with similar viscosity value (6 cps for oil, 1 cps for water) the size of the resultant water droplets depend not only by the oil phase flow but also significantly on the ratio of the flow rates between the water phase and oil phase. Gerstacki et al. did a more detailed studies on a similar design flow focusing device with air as the disperse phase and liquid with varies viscosity as continuous phase[40]; key findings of this important work include: first, classical capillary instability theory based on unbounded continuous phase (no flow focusing, gas disperse freely into bubble in surround liquid) failed to predict the experimental observation in the speed of collapse of middle air flow column into droplets. The collapsing speed estimated by the classical theory, both in viscous or inertial force dominated region transitioned by Ohnesorge number (*Oh*) being unity, are 1 to 3 orders of magnitude larger than the observed middle air column collapse in the flow focusing device; meaning the normal stress applied by the continuous phase liquid on the disperse phase gas due to the focusing geometry play a dominating role in droplet (bubble) formation, termed "squeezing" mode due to the fact the disperse string is squeezed and pinched off. Second, they identified three stages of gas column collapse and only in the last stage when the gas column neck is squeezed to be very narrow does the interface become unstable due to Rayleigh type instability and break off the gas bubble[41-47]. Third, a rough proportional relation (not dimensionally scaled) on the volume of the resultant disperse phase droplet (V_d) was formulated to be: $V_d \propto 1/\mu_c Q_c$, where μ_c and Q_c denotes the viscosity and the flow rate of the continuous phase. Works by Utada et al.[44] and Suryo et al.[46] further explore the droplet breakup mechanism and showed that with increase of continuous phase liquid flow rate, shear stress applied by the continuous phase gradually dominate over the normal pinching force and the mode of droplet break up changes slightly from the 'squeeze' mode; into a

"dripping" mode; the droplet size continued to be controlled by viscosity and flow rate of the continuous phase. For scaling purpose, capillary number ($Ca = \mu_c U/\sigma$) is identified as the controlling dimensionless number governing the droplet size in this mode; where μ_c denotes continuous phase viscosity, U is flow velocity term, and σ is the interfacial tension between the two phases. In the "dripping' mode, the size of the sphere reduces with the increase of the *Ca* (generally controlled by increase continuous phase flow rate) until the velocity becomes too high and the droplet break-off mode transition into another region term the "jetting" region; where the size of droplet become unstable and unpredictable. Ganan-Calvo and Riesco-Chueca[45] investigate the boundaries between the stable "dripping" region and the and unstable "jetting" mode of flow focusing droplet flow and concluded that the boundary are controlled mainly by disperse stream based Reynolds number ($Re=\rho_d D_d U/\mu_d$) and Weber number ($We= \rho_d D_d U^2/\sigma$); where ρ_d , D_d, and μ_d are the density, column width(diameter), and viscosity of the disperse phase, and U is the average disperse phase column speed which is effected by flow rate ratio between the two phases and the flow focusing geometry. The Anna group further identified a potential new approach in generating extreme small monodisperse microdroplets by modifying the surfactant concentration in the continuous phase liquid[43]; the presence of the surfactant effectively decreased the interfacial tension between the two fluids and this would increase the capillary number *Ca* while keeping all other factors the same; and effectively pushing the transition boundary between stable "dripping" mode and unstable "jetting' mode toward higher *Ca* number, thus enable stable production of smaller microspheres without changing the flow focus channel geometry. More comprehensive works on the effects of flow focusing channel geometry and the fluid properties were presented by Lee et al.[49]; in this paper, experimental results of droplet size in multiple channel dimensions were plotted against a modified *Ca* number containing many of the channel dimensions.

$$Ca \equiv \frac{\mu_c Q_c a}{\sigma h \Delta z}\left[\frac{1}{w_{or}} - \frac{1}{2w_c}\right]$$

Where a, h,H d_{or}, and w_c are all particular dimensions of the particular flow focusing channel geometry. The diameter of the microdroplet in the squeezing and dripping mode showed a good power law correlation with this modified *Ca* number. For the entire data using several different dimensions but keeping the viscosity ratio between the two fluids at 1/40 (disperse phase/continuous), the fitted power exponents give the following relation:

$$d_n \propto Ca^{-0.33}$$

Where d_n denotes normalized microdroplet diameter. This result was remarkably similar to the previously mentioned finding of Gerstacki et al.[40]; where the volume of microdroplets was estimated to be inversely proportional to $\mu_c Q_c$ (which could be considered a form of capillary number without interfacial and dimensional terms). In the same paper, Lee et al. also observed when the viscosity ratio increases above 1/10 (disperse phase/continuous phase), the power law still holds but the power exponent no longer stay at -0.33, but goes lower.

The main reason for summarizing the above previous work was to compare the current proposed PDMS microsphere generation method against these theoretical findings in an attempt to find some parallel in fundamental mechanisms of PDMS microdroplet generation. Direct comparison with literature results may not be applicable due to the following facts: first, the differences in device geometry design means some of the geometrical dimensions used in the literature were not clearly defined in the current PDMS microchannel. Second, Due to the destructive nature of the PDMS prepolymer toward measuring instrument, data's are lacking for the interfacial tension values and the viscosity values for the mixtures of PDMS prepolymer with toluene at different ratios, as used in this paper; thus direct calculation of the capillary number *Ca* for the current system was not possible at this point.

Revisiting the experimental data shown in **Fig. 3.2**, it is realized that by simply taking a log-log plot of the current data set, a power law relation between the continuous phase (F108 solution) flowrate and the PDMS microsphere diameter also become

apparent; as shown in **Fig. 3.2B**. The data curve for 1:1 PDMS-toluene ratio can be fitted to a power exponent of -0.317; and the data curve for 3:1 PDMS-toluene ratio can be fitted to a power exponent of -0.436. In both cases, the coefficient of determination (R^2) value for the data to power law fitting are above 0.99. This power law compliance shows an important parallel in fundamental mechanism for current flow focus channel to different designs in literature. The difference in power exponent value compare to ~0.33 was also explained by the vastly different range of viscosity ratio between the two fluids. In the current PDMS microsphere channel, the disperse phase (PDMS-Toluene) fluid has a much higher viscosity (can you give some estimate of the magnitude.) than the continuous phase fluid (0.1 % F108 solution); so the viscosity ratio would go much above unity (disperse phase/ continuous phase). As mentioned by Nei et al.[48], and Lee et al.[49], this change of viscosity ratio above ~0.1 will start to affect the exponent number of the power law fitting significantly. Finally, the high continuous phase (F108 solution) flow condition which was experimentally observed to be unstable and producing non-uniform sized PDMS microsphere can be explained by the fact that the system had reached the "jetting' region.

The fundamental similarity of current PDMS channel to the different designs analyzed in literature enable the following postulates in future continuous attempts to achieving the objective of smaller, uniform sized PDMS microspheres:

a. Reducing general microchannel dimensions: since the droplet size are geometrically constrained in "squeezing" and "dripping" mode of microdroplets flow. However, this approach need to be taken carefully, as when the dimension of the channel decrease, by scaling law the Weber number (*We*) would increase much faster than capillary (*Ca*) number; and the flow regime may shift to unstable "jetting" region much faster[45]; thus lessening the effectiveness of this approach. Careful reduction of both disperse phase flow and the continuous phase flow will be needed.

b. Modifying the surfactant (Pluronic F108) concentration in the continuous phase solution: this is applying studies by Anna et al.[43], where the increase in

surfactant concentration induces a new microdroplet flow regime where extremely small droplet could be generated. This attempt could be done and evaluated with the current channel geometry.

The unique capability of the PDMS microsphere to be surface modified and generating crack patterns, and the ability to deposit varies proteins and metals along these surface patterns presents some potential applications in the fields of biomedical and material sciences. For instance the gold wire patterns can be further functionalized with functional materials with high gold affinity, such as thiol group[50,60]; and microspheres themselves become microscale scale objectives with particular complex functional surfaces. These will be particularly interesting in the studies of microscale self-assemblies[60-63]. The nanowire-patterned surface of the microsphere could be chemically treated and functionalized and used as new kind of 3D micro-sized sensors for bio-molecules[50,56,57,64], which so far has been mostly done on 2D flat surfaces in the microchannel. With the continuing effort to reduce the size of the PDMS microsphere, potential toward the order of the spread-out cell attachments, these microspheres can also be use as new kind biological microcarriers, with designed complex surface chemical property, for novel cells for behavior studies[4,5,65].

3.4 Conclusions

In summary, an efficient method using droplet formation in a microchannel device has been used to fabricate small PDMS microspheres. To adapt to the properties and overcome the inherent difficulties in manipulating the high viscosity, highly adhesive PDMS pre-polymers; following necessary modifications from the popular flow focusing type two-phase emulsification method are studied and utilized:

1. Channel geometry is redesigned to avoid the direct contact between the disperse phase PDMS prepolymer and the channel wall. Sharp edges and narrow orifice are eliminated.

2. Channel geometry is also redesigned to accommodate high continuous phase to disperse phase flow ratio. Smooth converging geometry is used to enhance smooth flow profile. Due to the extreme high viscosity of the PDMS prepolymer, the flow ratios up to 1200:1 or beyond are needed to generate microdroplets of desired size; much higher than regular oil-in-water or water-in-oil two phase flow in literature.

3. Flow rate adjustments for both the continuous phase and disperse phase flows are ramped slowly to avoid excessive change of flow pattern in the microchannel.

4. Solvent (Toluene) is added to PDMS prepolymer to reduce the continuous phase viscosity.

5. PDMS Prepolymer solutions are temperature controlled to prevent premature curing.

6. Channel wall are oxygen treated to enhance hydrophilicity which enhance the contact with aqueous continuous phase while isolate the disperse phase PDMS prepolymer.

As a result, controllable and uniform sized PDMS microspheres in the range of 85-200 microns were mass-produced in a simple, efficient fashion for the first time. The parametric study result provides a valuable reference in determining the fabrication set-up condition to produce desired microsphere size.

Taking advantage of the unique property of PDMS, crack patterns were introduced on the surfaces of the microspheres by compression force after curing and a surface treatment of plasma oxidization. Some degrees of controllability are available for these surface patterns through compression ratio applied to the PDMS microsphere, and it

is extremely difficult to engineer these surface features on the object surface of this size skill any other way. These crack patterning demonstrates the potentials to generate simple to complex microscale surface cracking features on a single microsphere or, if desired, a self-assembled monolayer or multi-layer patch of numerous PDMS microspheres. To further enhance the potential functionality of the patterned PDMS microspheres in varies biological and material science applications, surface crack patterns are selectively treated with fluorescence protein and a gold nanoparticles to form nanowire; which is achieved by further taking advantage of the unique surface properties of PDMS material; potentially offering a new kind of microscale function material, with complex surface structures. Finally, efforts are underway to further expand the functional capabilities of surface patterned PDMS microspheres by decreasing the size of microspheres and altering the softness.

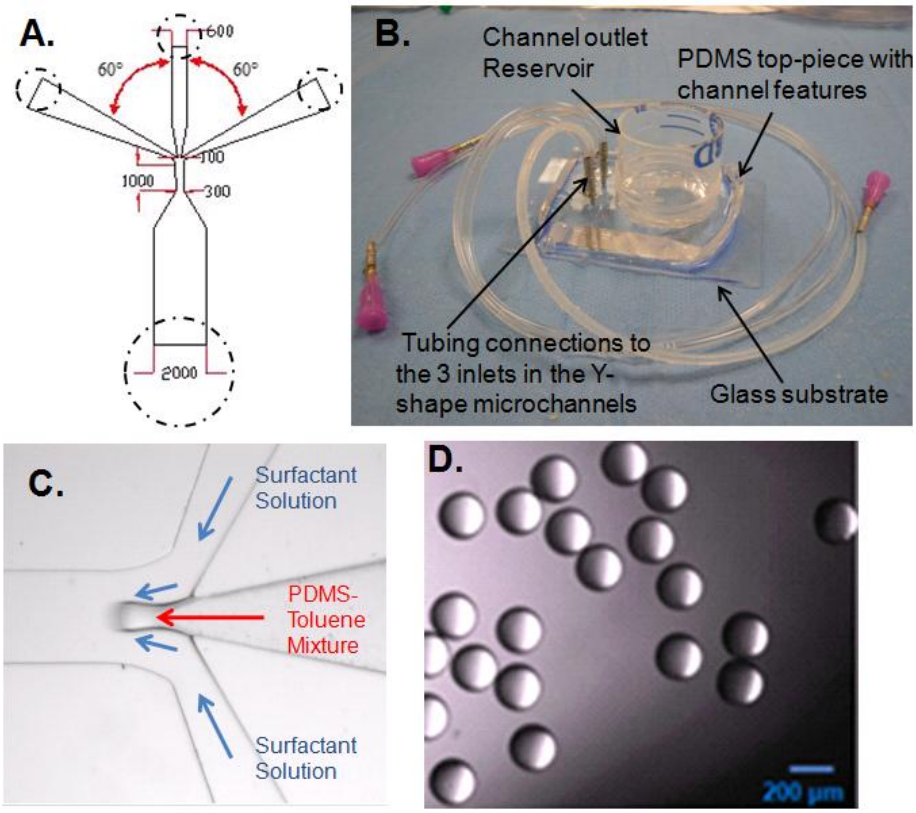

Figure 3.1. A) Geometric design for the Y-shaped 3-inlet microchannel device used in PDMS microsphere production. Units for dimensions are in micron. B) A completed microchannel device with a PDMS channel top piece bonded to a glass substrate. Tubing is connected to the three inlets, and an outlet reservoir is fabricated by cutting out a 50 ml conical section. C) A stream of a PDMS-toluene solution exits a central channel, and interacts with flows of a surfactant solution from the two side channels; flow focusing flow generate the droplets. D) PDMS Prepolymer Micro-droplets that are collected in the outlet reservoir before curing.

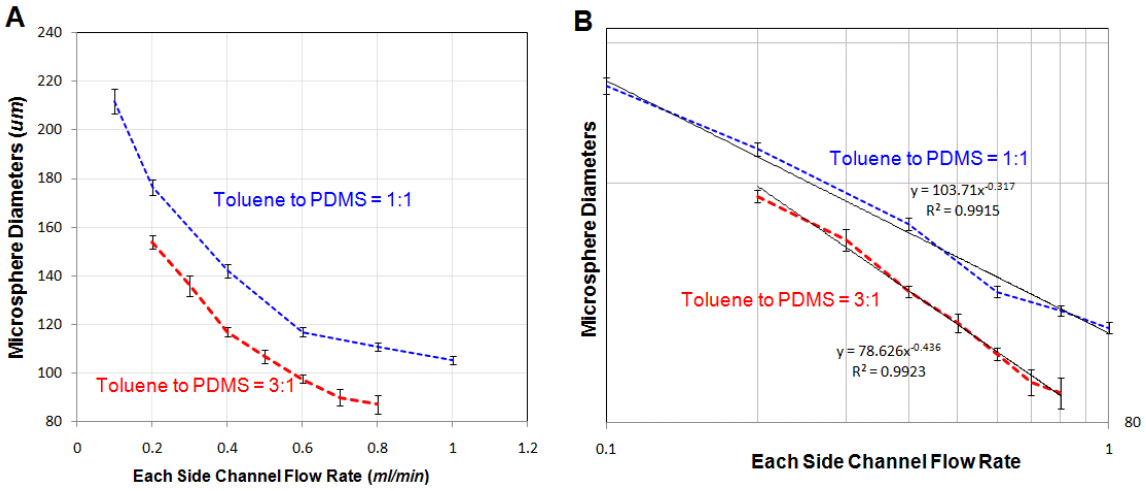

Figure 3.2. A) The size of the microspheres decreases as the flow rate of the side channels increases. The PDMS pre-polymer-toluene mixture flow rate is kept at 0.03 ml/hr. The upper curve is for a toluene to PDMS pre-polymer ratio of 1:1, and the bottom curve is for a ratio of 3:1, which is much less viscous mixture. The less viscous pre-polymer results in smaller microspheres, this is consistent with postulates of the dimensional analysis. B) The log-log plot of the same data presented in **Fig. 3.2A**; add the power law estimation trend lines of the data series. Note that the power law fits the data series very well with high coefficient of determination (R^2> 0.99); which almost result in linear relations in this plot. This result is very similar to the diameter to capillary number relation presented by Anna et al.[43,49], showing the similarity in droplet emulsification mechanism, even with very different flow focusing channel design.

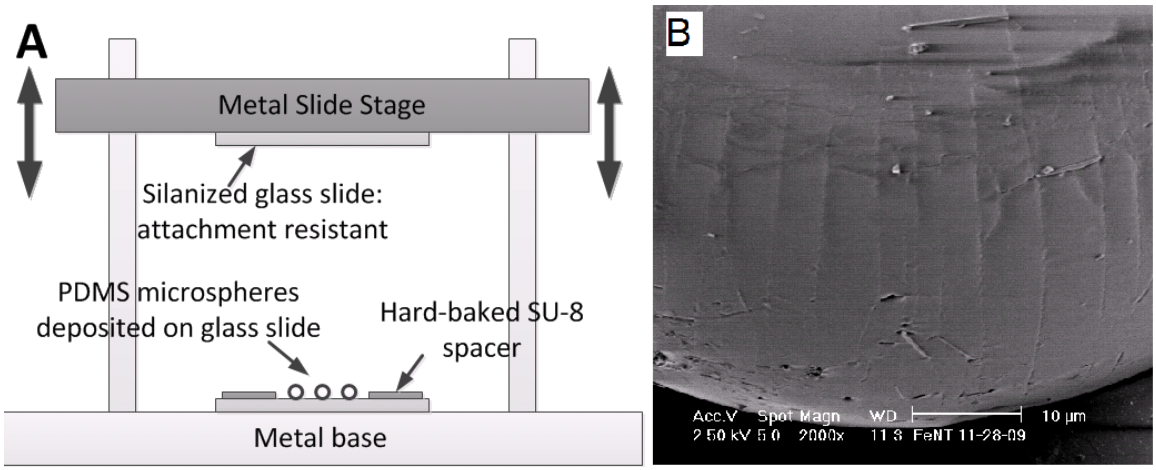

Figure 3.3. A) A custom built compression apparatus used with slight modifications to provide a uniform compression on a layer of surface-modified PDMS microspheres to form the crack patterns. B) SEM image of a single PDMS microsphere (diameter = 150 µm), compression ratio = 46.7% (with 80 µm spacer). The crack pattern consists of contact circle at the poles, and parallel meridian cracks that are in general evenly spaced; result is agreement with larger sphere cracking observed by Uchida et al[31].

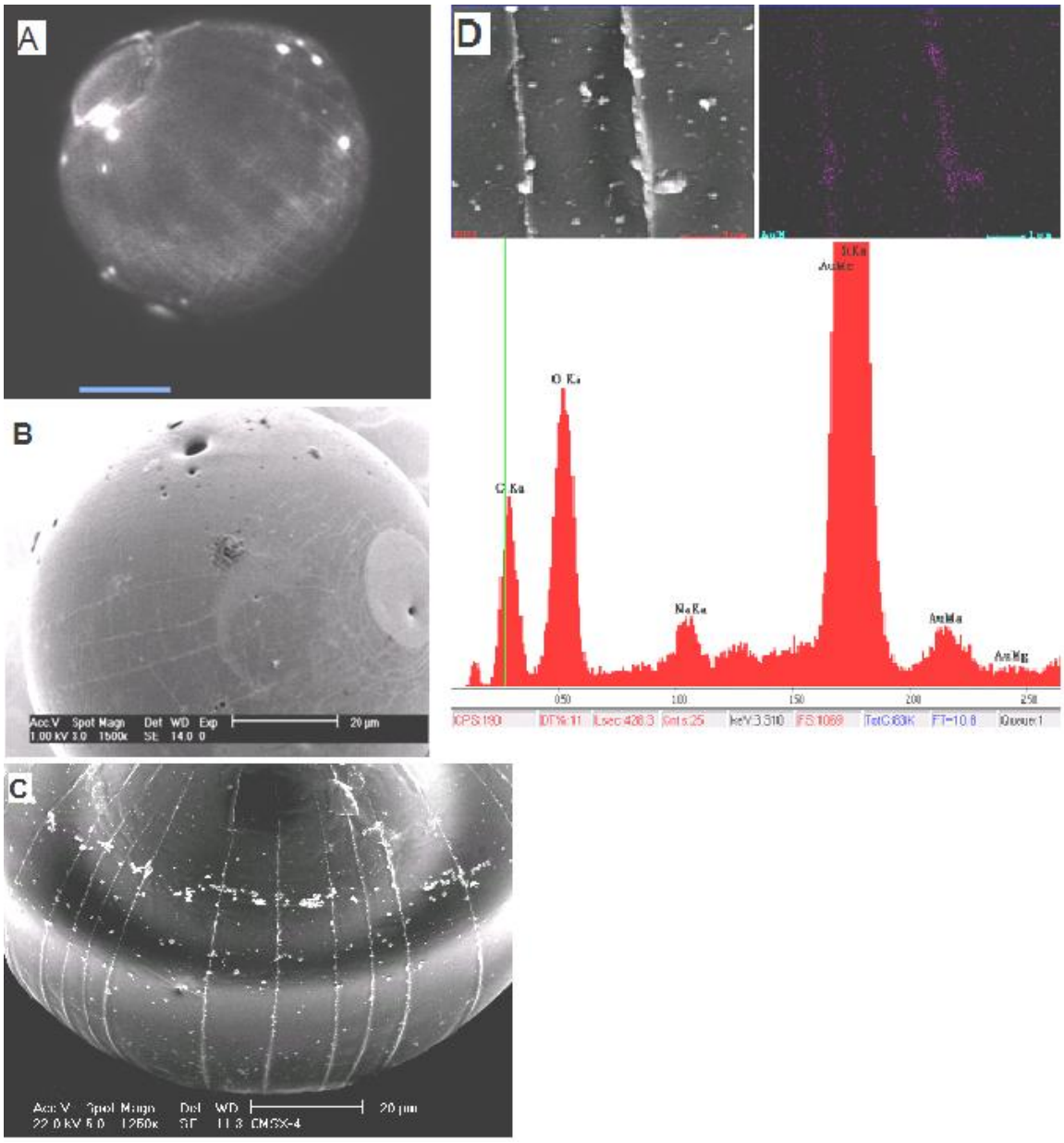

Figure 3.4. A) Fluorescence microscopy image of the PDMS microsphere (diameter = 143 µm, crack ratio = 30.3%) with crack patterns selectively deposited with fluorescence protein (TRITC-BSA). Scale Bar denote 30 micron. Please note that the fluorescence patterns on the microsphere surface are very similar to that of **Figure 3.3B**. B) SEM image of the PDMS microsphere selectively deposited with TRITC-BSA on the compression crack patterns. The protein deposited cracks show a very distinctive look of stained surface, as compare to the cracks that are not deposited with TRITC-BSA as in **Fig. 3.3B**. C) A PDMS microsphere (diameter = 114 µm, crack ratio ~30%, with 80µm spacer) with gold nanowire deposited on the surface along the compression patterns. Parallel gold nanowires generally pretty evenly spaced similar to that of **Fig. 3.3B**. The widths of the of gold wires range from 300 to 500 nm, which is in the order of the

compression crack width. D) Partial screen shot from Energy Dispersive Spectroscopy (EDS) analysis of the gold nanowire on the surface of the PDMS microsphere. The purple image on the upper right corner shows the gold (denoted AuM's on screen) traces detected from the bright-field image of the gold wire from upper-left corner. It shows clearly the outline of the wire matches the outline of the purple gold trace. The lower portion of the figure shows the counted peaks of each of the species detected from the bright-field image, which includes Gold (Au), Oxygen (O), Silicon (Si), Sodium (Na) and Carbon (C).

3.5 References

(1) Chen, C. S.; Mrksich, M.; Huang, S.; Whitesides, G. M.; Ingber, D. E. *Science* **1997**, 279, 1425-1428.

(2) Kato, D.; M. Takeuchi, M.; Sakurai, T.; Furukawa, S.; Mizokami, H.; Sakata, M.; Hirayama, C.; Kunitake, M. *Biomaterials*, **2003**, vol. 24, 4253–4264.

(3) Connors, W. L.; Heino, J. *Anal. Biochem*. **2005**, 337, 246-255.

(4) Kamishina, H.; Miyabayashi, T.; Clemmons, R. M.; Farese, J. P.; UHL, E. W. *J. Vet. Med. Sci.* **2006**, 68(11), 1239-1242.

(5) Yang, Y.; Rossi, F. M. V. Putnins, E. E. *Biomaterials* **2007**, 28, 3110-3120.

(6) Yap, F. L.; Zhang, Y. *Biomaterials*, **2007**, vol. 28, 2328–2338.

(7) Kiser, P. F.; Wilson, G.; Needham, D. *Nature* **1998**, 394, 459-462.

(8) Eniola, A. O.; Hammer, D. A. *Journal of Controlled Release* **2003**, 87, 15-22.

(9) Yang, C.-H.; Huang, K.-S.; Chang, J.-Y. *Biomed Microdevices* **2007**, 9, 253-259.

(10) Moore, G.D.; Croxatto, H. B. J. Reprod. Fert. 1988, 82, 735-742.

(11) Halling, A.; Von Mecklenburg, C.; and Forsberg J. G. J. Reprod. Fert. 1993, 99, 291-297.

(12) Derdeyn, C. P.; Graves, V. B.; Salamat, M. S.; Rappe, A. *Am J Neuror*adiol **1997**, 18, 647-653.

(13) Chemburu S.; Fenton K.; Lopez G. P. and Zeineldin R. Molecules 2010, 15, 1932-1957.

(14) Russias, J.; Saiz, E.; Nalla, R. K.; Tomsia, A. P. *J Mater Sci* **2006**, 41, 5127-5133.

(15) Diego, R. B.; Estelles, J. M.; Sanz, J. A.; Garcia-Aznar, J. M.; Sanchez, M. S. *Journal of Biomedical Materials Research Part B: Applied Biomaterials* **2007**, 81B, 448-455.

(16) Liu, Y.; Wang, S.; Krouse, J.; Kotov, N. A.; Eghtedari, M.; Vargas, G.; Motamedi, M. *Journal of Biomedical Materials Research Part A* **2007**, 83A(1), 1-9.

(17) Lee, J.; Cuddihy, M. J.; Kotov, N. A. *TISSUE ENGINEERING: Part B* **2008**, 14(1), 61-86.

(18) Comiskey, B.; Albert, J. D.; Yoshizawa, H.; Jacobson, J. *Nature* **1998**, 394, 253-255.

(19) Wu, M.; Park, C.; Whitesides, G. M. *Langmuir* **2002**, 18(24), 9312-9318.

(20) Yabu, H.; Shimomura, M. *Langmuir* **2005**, 21(5), 1709-1711.

(21) Cheng, C.; Kubicek, J. D.; LeDuc, P. R. *Apply Physics Letters* **2006**, 88, 053902-1 to 053902-3.

(22) Um, Eujin.; Lee, D. S.; Pyo, H.-B.; Park, J.-K. *Microfluid Nanofluid* **2008**, 5(5), 541-549.

(23) Nisisako, T.; Torii, T.; Higuchi, T. *Chemical Engineering Journal* **2004**, 101, 23-29.

(24) Huang, K.-S.; Lai, T.-H.; Lin, Y-C. *Lab Chip* **2006**, 6, 954-957.

(25) Tan, W.-H.; Takeuchi, S. *Adv. Mater.* **2007**, 19, 2696-2701.

(26) Morimoto, Y.; Tan, W.-H.; Takeuchi, S *Biomed Microdevices* **2009**, 11, 369-377.

(27) Kim, M. S.; Lee, G. H.; Hong, J.-M.; Lee, H. *Materials Science and Engineering* **2007**, C 27, 1247-1251.

(28) Nisisako, T.; Torii, T.; Higuchi, T. *Proc. IEEE Int. Conf. on Micro Electro Mechanical Systems* ,Kyoto, Japan, 19–23 January **2003**, pp 331–4

(29) The, S.-Y.; Lin, R.; Hung, L.-H.; Lee, A. P. *Lab Chip*, **2008**, 8, 198–220

(30) Whitesides, G. M.; Ostuni, E.; Takayama, S.; Jiang, X.; Ingber, D. E. *Annu. Rev. Biomed. Eng.* **2001**, 3, 335-373.

(31) Uchida, T.; Mills, K.L.; Kuo, C. H.; Roh, W.; Tang, Y. C.; Garner, A. L.; Koide, K.; Thouless, M. D.; Takayama, S. *Langmuir* **2009**, 25(5), 3102-3107.

(32) (h4) Mills, K. L.; Zhu, X.; Takayama, S.; Thouless, M. D. J. Mater. Res. 2008, 23(1), 37-48.

(33) Zhu, X.; Mills, K. L.; Peters, P. R.; Bahng, J. H.; Liu, E. H.; Shim, J.; Naruse, K.; Csete, M. E.; Thouless, M. D.; Takayama, S. *Nature Materials* **2005**, 4, 403-406.

(34) Xia, Y.; Yin, Y.; Lu, Y.; and McLellan, J. *Adv. Funct. Mater.* **2003**, 13(12), 907-918.

(35) Ozaki, T.; Sugano, K.; Tsuchiya, T.; Tabata, O. Proceedings of The IEEE International Conference on Micro Electro-Mechanical Systems (MEMS 2008), 1048-1051.

(36) Kang, H.; Lee, J.; Park, J.; Lee, H. H. *Nanotechnology* **2006**, 17, 197-200.

(37) Chueh, B.-H.; Huh, D.; Kyrtsos, C. R.; Houssin, T.; Futai, N.; Takayama, S. *Anal Chem.* **2007**, 79(9), 3504-3508.

(38) Meincken, M.; Berhane, T. A.; Mallon, P. E. *Polymer* **2005**, 46, 203-208.

(39) Anna, S. L.; Bontoux, N.; Stone, H. A. *Applied Physics Letters* **2003**, 82, 3, 364-366.

(40) Garstecki, P.; Stone, H. A.; Whitesides. G. M. *PHYSICAL REVIEW LETTERS* **2005**, 94, 164501-1:4.

(41) Hardt, S.; Jiang, F.; Schonfeld, F. *International Journal of Multiphase Flow* **2005**, 31, 739-756.

(42) Martin-Banderas, L.; Flores-Mosquera, M.; Riesco-Chueca, P.; Rodriguez-Gil, A.; Cebolla, A.; Chavez, S.; Ganan-Calvo, A. M. *Small* **2005**, 1(7), 688-692.

(43) Anna, S. L.; Mayer, H. C. *PHYSICS OF FLUIDS* **2006**, 18, 121512-1:13.

(44) Utada, A. S.; Lorenceau, E.; Link, D. R.; Kaplan, P. D.; Stone, H. A.; Weitz, D. A. *SCIENCE* **2005**, 308, 537-541.

(45) Ganan-Calvo, A. M.; Riesco-Chueca, P. *J. Fluid Mech.* **2006**, 553, 75-84.

(46) Suryo, R.; Basaran, A. *PHYSICS OF FLUIDS* **2006**, 18, 082102-1:13.

(47) He, Y. *Chemical Engineering Science* **2008**, 63 2500-2507.

(48) Nie, Z.; Seo, M.; Xu, S.; Lewis, P. C.; Mok, M.; Kumacheva, E.; Whitesides, G. M.; Garstecki, P.; Stone, H. A. *Microfluid Nanofluid* **2008**, 5, 585-594.

(49) Lee, W.; Walker, L. M.; Anna, S. L. *PHYSICS OF FLUIDS* **2009**, 21, 032103-1:14.

(50) Busse, S; Kashammer, J.; Kramer, S.; Mittler, S. *Sensors and Actuators* **1999**, B, 60, 148-154.

(51) Lacour, S.; Wagner, S. Huang, Z.; Suo, Z. *Applied Physics Letters* **2003**, 82, 15, 2404-2406.

(52) Scheibel, T,; Parthasarathy, R.; Sawicki, G.; Lin, X.-M.; Jaeger, H; Lindquist, S. L. *PNAS* **2003**, 100, 8, 4527-4532.

(53) Sun, Y.; Choi, W. M.; Jiang, H; Huang, Y. Y.; Rogers, J. A. *Nature Nanotechnology* **2006**, 1, 201-207.

(54) Kim, D.-H.; Song, J.; Choi, W. M.; Kim, H.-S.; Kim, R.-H.; Liu, Z.; Huang, Y. Y.; Hwang, K.-C.; Zhang, Y.-W.; and Rogers, J. A. *PNAS* **2008**, 105, 48, 18675-18680.

(55) Kim, D.-H.; Rogers, J. A. *ACS Nano* **2009**, 3(3), 498-501.

(56) Cui, Y.; Wei, Q.; Park, H.; Lieber, C. M. *SCIENCE* **2001**, 293, 1289-1292.

(57) Ozaki, T.; Sugano, K.; Tsuchiya, T.; Tabata, O. *MEMS* **2008**, January 13-17, 1048-1051.

(58) Sauer, G.; Brehm, G.; Schneider, S. *J. Appl. Phys.* **2002**, 91, 5, 3243-3247.

(59) Fan, Z.; Ho, J. C.; Jacobson, Z. A.; Razavi, H.; Javey, A. *PNAS* **2008**, 105, 32, 11066-11070.

(60) Braun, P.; *Nature Materials* **2004**, 3, 281-282.

(61) Jackson, A. M.; Myerson, J. W.; Stellacci, F; *Nature Materials* **2004,** 330-335.

(62) Glotzer, S. C. *Science* **2004**, 306, 419-420.

(63) Zhang, Z.; Glotzer, S. C. Nano Lett., 4, 8, 1407-1413.

(64) Nakao, H.; Shiigi, H.; Yamamoto, Y.; Tokonami, S.; Nagaoka, T.; Sugiyama, S.; Ohtani, T. *Nano Lett.* **2003**, 3, 10, 1391-1394.

(65) Schwarz, U. *Soft Matter*, **2007**, 3, 263-266.

CHAPTER 4

Gas–liquid two-phase flow patterns in rectangular polymeric microchannels: effect of surface wetting properties

Here we map gas–liquid two-phase flow regimes observed in polymeric microchannels with different wetting properties. We utilized video and confocal microscopy to examine two-phase flow patterns produced by parallel injection of air and water through a Y-shaped junction into a rectangular microchannel made of poly(dimethylsiloxane) (PDMS). We observed seven flow regimes in microchannels with hydrophobic walls, whereas only two flow patterns were identified in hydrophilic microchannels. Our study demonstrates that surface wettability has a profound influence on the spatial distribution of air and water moving in microchannels.

4.1 Introduction

Two-phase flows are encountered in a wide range of applications including heat exchangers, oil/gas processing and transport, nuclear and chemical reactors, cryogenics, air pollution control, food production and rocketry. In microfabricated systems, two-phase flows offer new opportunities to enhance and extend the performance of single-phase microfluidics by greatly increasing the rate of heat/mass transfer and preventing sample dispersion. Over the past decade, the potential of two-phase flows at the microscale has gained increasing attention and provided an impetus for the development of multiphase microfluidic systems for a variety of applications such as emulsification [1, 2], electronic chip cooling [3], chemical reactions [4]–[6], flow cytometry [7, 8], material synthesis and fabrication [9]–[14], computation [15, 16], chemical detection/screening [17]–[19] and cell encapsulation/analysis [20]–[23]. This in turn has created the demand for a better understanding of the flow behavior of immiscible fluids inside microchannels, which is crucial for successful design and operation of functional multiphase microfluidic systems.

One of the most conventional ways to characterize two-phase flows is to examine flow regimes defined by distinct spatial distribution of moving fluids. Generally, two-phase flow regimes observed in any given channel depend on several factors including fluid flow rates, fluid properties, channel geometry, channel orientation, surface properties and channel size. For example, early work by Taitel and Dukler [24] related these factors to a model predicting the flow regime transitions and developed a generalized two-phase flow regime map for horizontal gas–liquid two-phase flow. They proposed various criteria for growth, propagation and dissipation of surface waves originated from Kelvin–Helmholtz-type instability as the basis for transitions from stable stratified flow to wavy stratified flow, intermittent flow (slug and plug) and annular dispersed flow. Their subsequent work on gas–liquid two-phase flows in vertical tubes also identified gas–liquid surface tension as one of the factors affecting transitions between different flow patterns [25].

In microscale two-phase flow, dimensional scaling dictates the dominant role of the surface interactions due to the increasing surface-to-volume ratio. Within a confined microchannel, these surface interactions include not only the interfacial interaction between the two phases, but also the interaction of each fluid with channel walls. As a result, the effect of surface properties of microchannel walls becomes prominent, which profoundly influences both the nature of twophase flows in microchannels and flow regime transitions. Two parameters that are often used to describe multiphase flow are Confinement number (*Co*) and Eotvos number (*Eo*):

$$Co = \frac{1}{D}\sqrt{\frac{\sigma}{g(\rho_L - \rho_G)}}$$

$$Eo = \frac{(2\pi)^2 \sigma}{(\rho_L - \rho_G) D^2 g}$$

where D is the hydraulic diameter of the flow channel, σ the surface tension, g the gravitational acceleration and ρ the density of the fluid. These dimensionless numbers represent the ratio of surface tension forces to buoyancy forces, and are often used to characterize the shape of interfaces between different fluids. They have also been employed to describe the transition from macroscale to microscale multiphase flow. For example, Suo and Griffith [26] defined microchannel flow as:

$$Co \geq 3.3$$

Brauner and Moalem-Maron [27] used the Eotvos number to define microchannel flow:

$$Eo > 1$$

Commonplace in these definitions is that the effect of surface tension forces becomes predominant over the buoyancy forces as the size of a channel decreases. Despite the increased effect of surface forces, the focus of previous studies on microscale multiphase flows was primarily on the effect of fluid properties [28], channel geometry [29, 30], orientation [31, 32] and size [31, 33, 34] on the morphology of gas–liquid two-phase

flows in small capillary tubes or microchannels fabricated in glass or silicon. Much remains to be learned about how the properties of microchannel surfaces affect the morphology of two-phase flows. Early studies by Damianides and Westwater [35], Graska [36], and Barajas and Panton [37] highlighted that the surface contact angle and surface tension between fluids are important variables in understanding gas–liquid two-phase flow patterns and transitions between different flow regimes in millimeter-sized capillary tubes. There have also been recent reports demonstrating the significant effect of surface properties such as wettability and cleanness on two-phase flow regimes [38] and flow boiling [39] in glass microchannels.

In this paper, we investigate the influence of surface wetting properties on air–water twophase flows in rectangular microchannels fabricated in one of the most widely used polymeric materials in microfluidics called poly(dimethylsiloxane) (PDMS). Specifically, we varied the hydrophobicity of the PDMS microchannels using a plasma-mediated surface modification method and injected air and water in parallel without premixing to generate high-speed air–water two-phase flows in a horizontal rectangular microchannel that is 300μm in width, 100μm in height and 1 cm in length. In this system, Confinement number (*Co*) and Eotvos number (*Eo*) were estimated to be 18.2 and 13 109.3, respectively. These numbers clearly indicate that the two-phase flow observed in our microfluidic system is well within the realm of microscale two-phase flow where surface tension forces play a predominant role in understanding flow regimes.

Various flow patterns observed using video microscopy were categorized into flow regime maps under different wetting conditions. We also used confocal microscopy to visualize and better understand the vertical distribution of a liquid phase inside microchannels. We show a dramatic difference in two-phase flow patterns caused by channel hydrophobicity; we found seven flow regimes in hydrophobic microchannels and two in hydrophilic channels.

4.2 Experimental

4.2.1 Material and Reagents

PDMS was obtained from Dow Corning Corp (Midland, MI) and SU8 negative photoresist from MicroChem. Corp (Newton, MA). Fluorescein sodium salt was purchased from Sigma-Aldrich (St Louis, MO).

4.2.2 Microchannel Fabrication and Preparation

Hydrophobic microchannels with a height of 100μm were created by casting PDMS prepolymer against a photolithographically prepared SU8 mold [7] and then bringing the negative relief patterns in conformal contact with a flat slab of PDMS. To make hydrophilic channels, the recessed microchannel features prepared by casting PDMS against a SU8 master were first bonded to a flat PDMS substrate irreversibly using plasma oxidation [7] to form enclosed microchannels. Immediately before use, the entire device was then treated with oxygen plasma to render the interior surfaces of the microchannel hydrophilic. The degree of channel hydrophilicity was varied by changing the time elapsed from plasma oxidation to the beginning of experiments. Using this method, three rectangular microchannels having different wetting properties were prepared: (i) untreated hydrophobic PDMS surface with a contact angle of 111º, (ii) hydrophilic surface (3 h after plasma oxidation, contact angle ~35º) and (iii) moderately hydrophilic surface (49 h after oxidation, contact angle ~77º).

4.2.3 Flow Setup

Air–water two-phase flows were generated by parallel injection of compressed air and deionized (DI) water without premixing as depicted in **figure 4.1**. The flow rate of

water was controlled by a syringe pump, and air flows were regulated by a flow-meter connected to a compressed air tank. Injected fluid streams and resulting flow patterns were observed in the downstream region using a high-speed camera mounted on an inverted epi-fluorescence microscope. For confocal microscopy, aqueous fluorescein solution with a concentration of 0.001% w/v (in DI water) was used as a working liquid to capture cross-sectional images of two-phase flow patterns.

4.3 Results and Discussion

In a hydrophobic microchannel with a surface contact angle of 111º, we identified seven flow regimes depending on the flow rates of air and water. Typical images of flow patterns captured during the experiments are shown in **figure 4.2**. In general, air–water two-phase streams maintain their original stratified flow configuration with various interfacial shapes and different degrees of interfacial stability at moderate water flow rates until the water column in the middle spreads to the sidewalls at very high flow rates of water or breaks up into small droplets due to twophase instability as the water flow rate becomes very low. It was noted that there existed maximum flow rates of air and water beyond which conformal seal between PDMS surfaces failed due to extremely high pressure generated by fluid pumps, and the microchannel became no longer operational. The seven flow regimes observed in hydrophobic PDMS microchannels include:

1. Stable stratified flow. This flow regime is prevalent in hydrophobic microchannels and appears mainly at moderate air and water flow rates. Injected water is focused by air flows to form stable stratification of a water column and two air streams (**figure 4.2(a)**). The width of the water column remains the same along the length of the microchannel and changes with the flow rate of water when the air flow rate is maintained constant (or vice versa). The most narrow

water column was observed to be as thin as 6μm. As shown in the crosssectional images in **figure 4.2(a)**, the water column is in contact with top and bottom channel walls, and the air–water interface has a convex shape.

2. Wavy stratified flow. Wavy stratified flow is characterized by a symmetric varicose wave along the air–water interface, which creates alternating locations of water column expansion and contraction (**figure 4.2(b)** and Movie 1). The wavy water column is stably maintained along the center of the microchannel and does not change its shape nor break up into droplets over time at constant air and water flow rates. We observed that the wavelength of the waves found in typical wavy stratified flow was smaller than approximately 600μm. As fluid superficial velocities were varied, the wavelength ranged between approximately 200 and 600μm, yet the flow was stable without any temporal changes in the interfacial shape.

3. Wiggly stratified flow. This flow pattern occurs at exceedingly high water flow rates and very low airflow rates. In this flow regime, the width of a water stream becomes thicker as a result of increased water flow rate, while the air flow rate is kept constant, and the interface between air and water exhibits wavy patterns undergoing unstable and highly irregular motion as the flow approaches the downstream region of the microchannel (**figure 4.2(c)** and movie 2).

4. Detached stratified flow. Interestingly, when the air flow rate is increased while maintaining the liquid flow rate at low levels, the water stream contacts both the top and bottom channel surfaces in the upstream region, but detaches from the bottom floor in the downstream area and forms a convex air–water interface surrounded by ambient air flow as illustrated in the confocal images of **figure 4.2(d)** and movie 3. Both the surface-bound (upstream) and -detached (downstream) columns are stably maintained along the axial line of symmetry without significant changes in their width.

5. Annular-droplet flow. Annular-droplet flow consists of a liquid films deposited along the channel sidewalls and air flow through the center (**figure 4.2(e)** and movie 4). The thin liquid films appear to oscillate in a lateral direction, and water droplets that are typically smaller than 50μm in diameter are entrained in the air stream and travel downstream at high speeds along the core region. This flow configuration becomes more pronounced when the flow rate of water is relatively high and the flow rate of air becomes sufficiently large.

6. Spreading stratified-droplet flow. This flow regime is distinguished by co-occurrence of water column and droplets as shown in **figure 4.2(f)** and movie 5. The water column appears to alternate between spreading and break-up at very high frequencies, resulting in the wetting of channel surface and formation of water droplets along the center of the microchannel. This unique pattern is believed to indicate the onset of two-phase instability as the water flow rate becomes smaller at moderate air flow rates and the water column can no longer maintain its structural integrity.

7. Break-up. In this regime, the water column is formed and immediately breaks up into small droplets (**figure 4.2(g)** and movie 6). This takes place for the entire range of the tested air flow rate when the flow rate of water is sufficiently low.

The hydrophobic flow map in **figure 4.4** show some similarities to the hydrophobic tube results reported in the literature [35, 37], which were generated by using an air–water twophase flow apparatus comprised of horizontal tubes with an inner diameter of between 1 and 5mm having several surface hydrophobic and hydrophilic properties. Parallels can be drawn both in overall flow mapping topology and the flow phenomena within each regime between the results reported in these earlier studies and the observations made in our two-phase micro fluidic system. For example, the characteristics of rivulet and bubbly flows reported in the work of Barajas and Panton [37] and Taitel and Dukler [24] are almost identical to those of stable stratified and annular-droplet flows observed in our experiments. The ranges of superficial gas and liquid velocities in which these flow patterns are predominant are also similar in the flow

map. These similarities are believed to suggest that there exists fundamental mechanics applicable to both macroscale two-phase flow in horizontal pipes and microscale two-phase flow in our microchannels. However, it should be pointed out that the effect of surface forces, which was not factored in the earlier physical modeling of macroscale channel flows, becomes essential in two-phase flow in microchannels. Although beyond the scope of this paper, it is believed that fundamental modeling scheme introduced by Taitel and Dukler [24] might be extended by incorporating surface force parameters to develop a physical model for microchannel two-phase flow described in our work.

It is noted that there existed occasional two-phase instabilities accompanying erratic fluid motion when fluids were initially injected into the channel or when fluid flow rates were varied to induce transition from one flow pattern to another. However, the unstable flow behavior subdued rapidly within 10 s, after which two-phase flow remained steady (in case of stable stratified, wavy stratified and detached stratified flows) or showed particular and predictable patterns with repetitive temporal variations (as in wiggly stratified flow, annular droplet flow, spreading stratified-droplet flow and break-up). Experimental observations were made after the flow reached this point and no longer exhibited transitional behaviors. We did not notice significant variability between experiments, and the same flow regimes were observed reproducibly at their corresponding superficial velocities. However, experiment-to-experiment variability increased near the boundaries between flow patterns, in which case (i) two-phase flow often alternated between two flow patterns neighboring in the flow regime map or (ii) initially observed flow regime persisted for a few seconds and gave way to its neighboring flow regime.

We did not observe a type of microscale two-phase flow called segmented flow that is often used for mixing and reaction applications in microfluidic systems [53, 54]. This may be attributed to sufficiently higher superficial fluid velocities tested in our work than those used to generate gas–liquid segmented flow reported in the literature. Also, we suspect that our Y-shaped junction at the fluid inlet and continuous supply of fluids prevent the segmentation of fluids.

In contrast to various flow patterns found in hydrophobic channels, only two flow regimes were observed in hydrophilic microchannels, regardless of the contact angle (35º and 75º). In both cases, injected water was quickly redistributed to sidewalls and formed a liquid lining of uniform thickness along the length of the channel as shown by confocal images in **figure 4.3(b)** (upper insets).

1. Annular-droplet flow. Annular-droplet flow in hydrophilic channels is slightly different from that in hydrophobic channels in that the water film along the sidewalls appear to be smoother and the phase boundary between water and air can be seen more clearly as illustrated **in figure 4.3(a)**, movies 7 and 8.

2. Annular flow. Annular flow is characterized by smooth liquid films on the sidewalls and can be distinguished from annular-droplet flow by the absence of dispersed water droplets in the center region (**figure 4.3(b)**, movies 9 and 10).

For a given air flow rate, increasing the flow rate of water shifts the flow regime toward annular flow. The absence of the stratified flow pattern could be related to the experimental observations reported by Triplett et al [30] and Chen et al [33] that it becomes impossible to form stratified two-phase flow in case of high Eotvos number flow (> 100), as would occur in microchannels under high surface tension conditions.

The degree of hydrophilicity does not affect the type of two-phase flows that can be identified over the range of air and water superficial velocities tested in the experiments. This observation is consistent with previously reported two-phase flow mapping data available in the literature [37]. However, the difference in channel hydrophilicity results in a notable change in the transition boundary between annular-droplet and annular flows. That is, when the contact angle is higher, annular-droplet flow becomes more prominent at low water superficial velocities, indicating more favorable formation of droplets on the channel surfaces presumably due to increased hydrophobicity. As compared with two-phase flows in a hydrophobic microchannel, the duration of transient instabilities observed before fully developed flow regimes formed was much shorter (less than 2 s) in hydrophilic channels, regardless of their surface

contact angle. Experimental variability still persisted near the transition boundaries, causing the flow to show characteristics of both annular-droplet and annular flows.

It is known that the PDMS surface rendered hydrophilic by plasma treatment is unstable and gradually recovers its hydrophobicity when exposed to air as a result of diffusion of low molecular weight chains from the bulk PDMS to the surface and their accumulation at the thermodynamically unstable surface [52]. To monitor hydrophobic recovery of hydrophilic PDMS, we measured static contact angle of water on plasma-treated PDMS surface at different time points after exposure to oxygen plasma (data not shown). We found that surface contact angle gradually increased as a function of time elapsed from plasma treatment. Therefore, careful attention was paid to the timing of experiments; for observation of flow patterns in a microchannel with a surface contact angle of 35º and 75º, we used PDMS microchannels that had been stored in dry air for 3.7 and 47 h, respectively. The duration of conducted experiments was strictly limited to no longer than 1 h to minimize the recovery of hydrophobicity; contact angle changes during the experiments were measured to be smaller than 2º.

The transition between annular flow and annular droplet flow is believed to be dependent on the onset of droplet entrainment from a moving air stream over a liquid film. It was proposed that the primary mechanism of this event may be the shearing off of the crest of Kelvin–Helmholtz type disturbance wave from low viscosity liquid such as water [40]. In annular air–water flow, this entrainment phenomenon results in water phase traveling along the wall as a liquid film and flowing through the air core as droplets; this is often described by a parameter called entrainment fraction, which represents the combined effects of droplet entrainment and redeposition [41]. Physically, entrainment fraction approaching zero represents pure annular flow without the droplets in the air core. Many researchers attempted to correlate the entrainment fraction with the two-phase flow parameters empirically [42]–[44], and found that the correlation is strongly associated with the following two parameters: air-phase Weber number (*We*) and its modified forms comparing air flow velocity-based inertial force to air–water surface tension force, and liquid phase Reynolds number (*Re*). Although the equations for

entrainment fraction were developed for macroscale flow conditions in large pipes with diameters on the order of centimeters, they appear to perform adequately in describing the flow transitions in hydrophilic microchannels shown in **figures 5(a)** and **(b)**. For example, the equation developed by Savant et al [44] is given by

$$E = \left(1 - \frac{\mathrm{Re}_{ff-\lim}}{\mathrm{Re}_f}\right)\tanh(a \bullet We^{1.25})$$

$$a = 2.31\times10^{-4}\,\mathrm{Re}_f^{\,-0.35}$$

where E is the entrainment fraction, Ref is the liquid-phase Reynolds number, and limiting liquid film Reynolds number Re_{ff-lim} is obtained from the following empirical equation:

$$\mathrm{Re}_{ff-\lim} = 250\ln\left(\mathrm{Re}_f\right) - 1265$$

For the range of liquid-phase Reynolds number and air-phase Weber number tested in the current work, the transition boundary line between pure annular flow (i.e. zero entrainment fraction) and annular-droplet flow predicted by these correlation equations are shown in **figure 4.6**, along with the boundary line established by actual experimental data shown in **figure 5(a)**. Although there are discrepancies between the predicted and experimentally observed transition lines, they both show a general trend of positive slopes, which extend along increasing superficial air and water velocities. This similarity strongly suggests that the mechanism dictating the transition between pure annular and annular-droplet flows is based on droplet entrainment. We suspect that the mismatch between the estimations and actual experimental data may arise from the fact that the correlation equations were originally developed for macroscale flows in larger circular pipes.

Furthermore, the entrainment fraction correlations may also help explain the shift of flow regime transition line between two different levels of hydrophilicity since it is known that the surface contact angle affects the water film thickness on the surface of the

channel wall [45, 46]; at the same superficial water velocity, difference in surface wettability results in different local water velocity to ensure flow continuity. According to the correlation equation by Savant et al [44], this change in local water-phase Reynolds number would shift the transition line between annular flow and annular-droplet flow.

In this work, we have constructed two-phase flow regime maps for the hydrophobic (**figure 4.4**) and hydrophilic (**figure 4.5**) microchannels. Various flow patterns identified in hydrophobic channels are replaced by two flow regimes in hydrophilic channels, making it evident that the modification of interfacial properties between fluids and channel surfaces has a profound influence on the spatial distribution of fluids moving through a microchannel. Considering that most of the multiple flow regimes found in hydrophobic channels are variations of stratified flow having a water stream confined along the centerline of a channel, we speculate that the drastic difference in flow patterns may be attributed to the inability of hydrophilic microchannels to support the formation of a water column focused by air flows: hydrophilicity causes injected water to wet channel surfaces and spread to corners to minimize interfacial surface area exposed to ambient air [7, 8]. In summary, two factors are believed to promote the high sensitivity of two-phase flow to wall surface properties demonstrated by our microfluidic device. Firstly, the cross-sectional dimensions are sufficiently small that surface forces become more important and play a crucial role in the interaction between different phases. Secondly, the flow configuration where a water column is sheathed by two air streams is inherently sensitive to the forces that affect the integrity of the water column, which include the surface tension forces between the top and bottom channel walls and water, and the pressure and entrainment forces exerted by the air flow. These two factors were not present in similar two-phase flow experiments reported in the literature [35, 37]. This may explain why, in other work, the topology of the flow regime maps does not show a dramatic change when wettability of the channel wall was altered from hydrophobic to hydrophilic. Although the dominant effect of surface properties increases the complexity of analyzing two-phase flow regimes, it provides an effective means to dramatically change and manipulate the flow pattern within the microchannel, which may enable the development of novel methods for controlling multiphase flows in micro

fluidic devices. For example, Huh et al [8] utilized electrical modulation of surface wettability to switch air–water two-phase flow regimes dynamically and reversibly in elastomeric microchannels. Other methods for controlling microscale multiphase flows include thermocapillarity [47], chemical coating [48]–[50] and surface topography [51].

4.4 Conclusion

Our work demonstrates that different wetting properties of a microchannel give rise to dramatic changes in the morphological characteristics of two-phase fluid flows at the microscale. We show that surface hydrophobicity in rectangular elastomeric microchannels results in six types of stratification of air–water two-phase flow with various interfacial shapes, and break-up of water stream into droplets originating from two-phase instabilities. Hydrophilic microchannels were found to cause the water phase to wet channel surfaces immediately and collect at the corners. This configuration led to the formation of annular flow and annular-droplet flow regimes. The drastic difference in flow patterns caused by changes in surface chemistry is particularly relevant to understanding the mechanism of the microfluidic actuation that enables reversible switching of two-phase flow patterns using electrical modulation of surface wettability [13]. Flow regime maps established in this study also allow us to identify the bounds of operation in such microfluidic systems. Moreover, our data open new possibilities to manipulate and engineer high-speed gas–liquid two-phase flows in elastomeric microchannels, which may enable new designs of multiphase microfluidic systems and novel methods for creating and controlling dynamic two-phase flows for various applications. We envision that this will be greatly facilitated by various techniques that are readily available for patterning and modifying the surface chemistry of PDMS. We believe that transient nature and important timescales of different types of two-phase flows (e.g. time required to form fully developed flow) examined in our study will

provide valuable design considerations for the development of microfluidic actuation methods based on surface chemistry changes. The performance of such microsystems can also be extended to higher levels of functionality through on-chip integration with more sophisticated methods for reversibly modulating surface energy such as electrowetting and thermocapillarity.

It should be noted, however, that the experimental work presented in this paper is largely qualitative and focuses mainly on highlighting various flow patterns resulting from changes in surface properties of a microchannel. Understanding the physics of flow patterns and transitions observed in our system will require further analysis based on more standardized parameters in two-phase flow such as void fraction and frictional pressure drop. This will allow us to characterize the distribution of different phases more accurately and eventually develop empirical correlations that can describe and predict the transition from one flow regime to another or practically important processes such as heat and mass transfers.

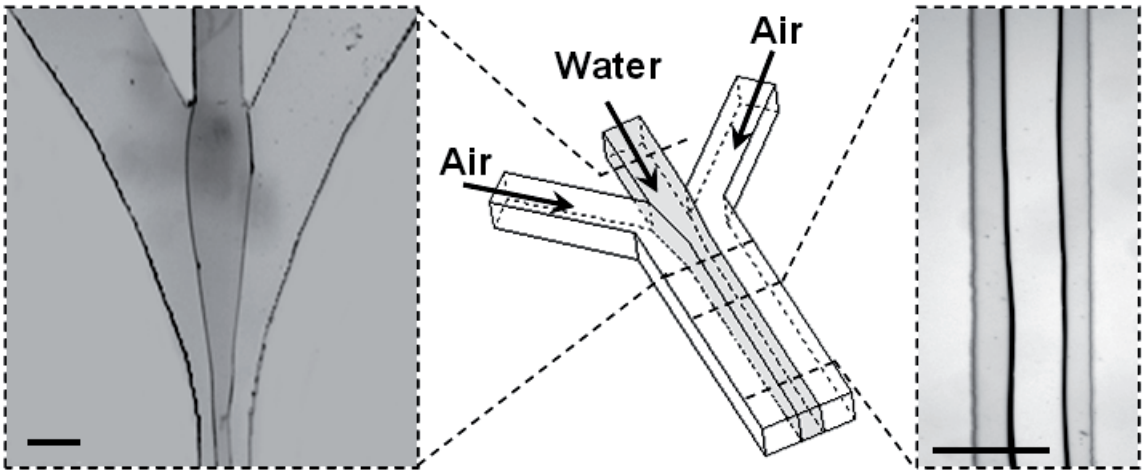

Figure 4.1. Schematic diagram of an experimental setup used to generate and observe air–water two-phase flow patterns. Water flow was driven by a syringe pump connected to the middle inlet, and gas flows were generated by compressed air injected into the side inlets. Resulting two-phase flow is observed in the downstream region. The micrographs show an example of two-phase flow in a hydrophobic PDMS microchannel. Scale bars, 300 m.

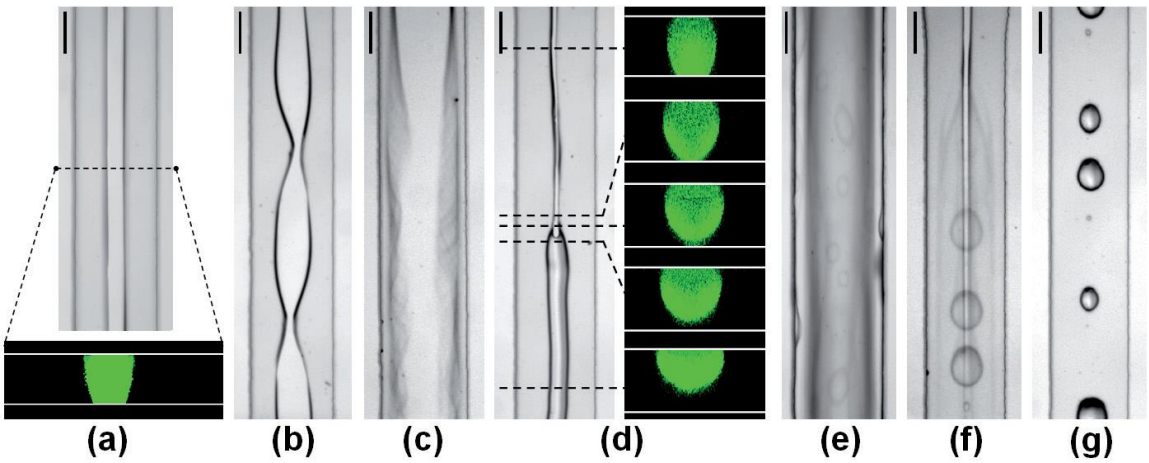

Figure 4.2. Air–water two-phase flow patterns found in a hydrophobic PDMS channel with a contact angle of 111º. Seven flow regimes were observed with changing fluid flow rates: (a) stable stratified flow, (b) wavy stratified flow, (c) wiggly stratified flow, (d) detached stratified flow, (e) annular-droplet flow, (f) spreading stratified-droplet flow, and (g) break-up. Cross-sectional images shown in (a) and (d) were taken by confocal microscopy. Scale bars, 150μm.

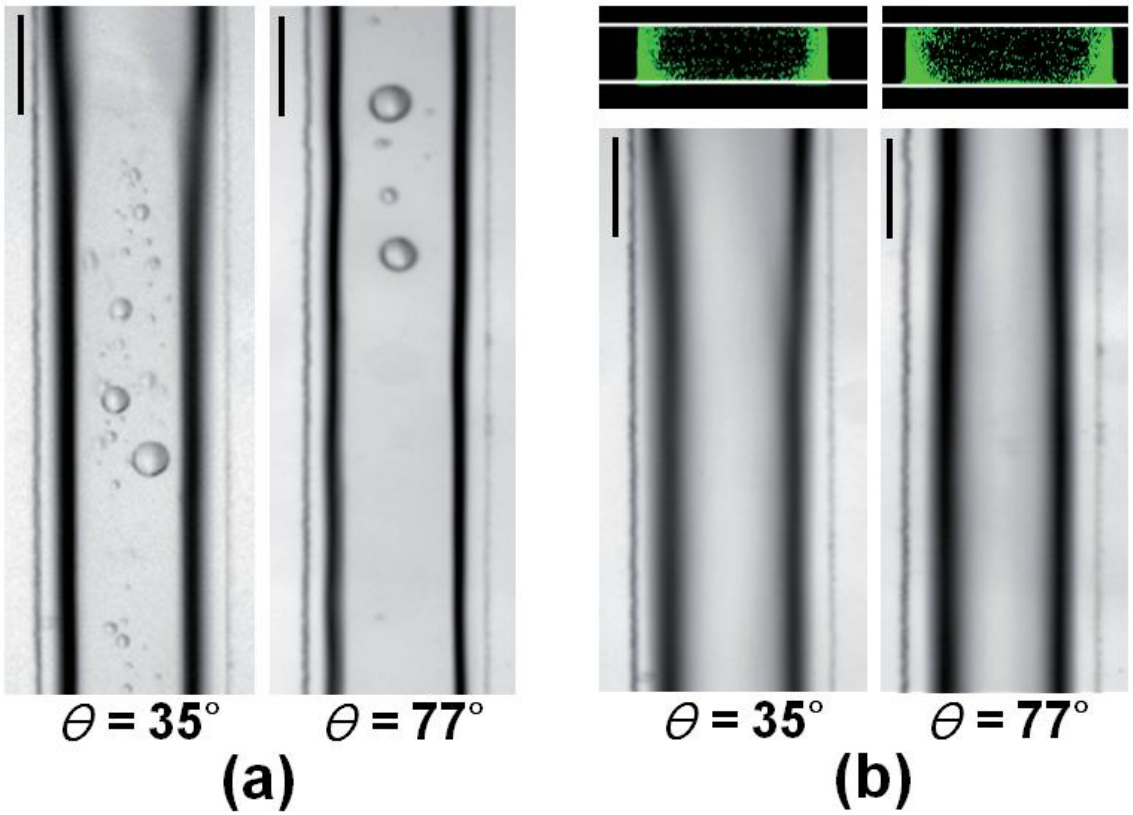

Figure 4.3. Representative images of two flow regimes identified in hydrophilic channels with different surface wettability (contact angle (Θ) = 35ºand 77º). (a) Annular-droplet flow. (b) Annular flow. Upper insets in (b) show the cross-sectional view of annular flow captured by confocal microscopy. Scale bars, 150μm.

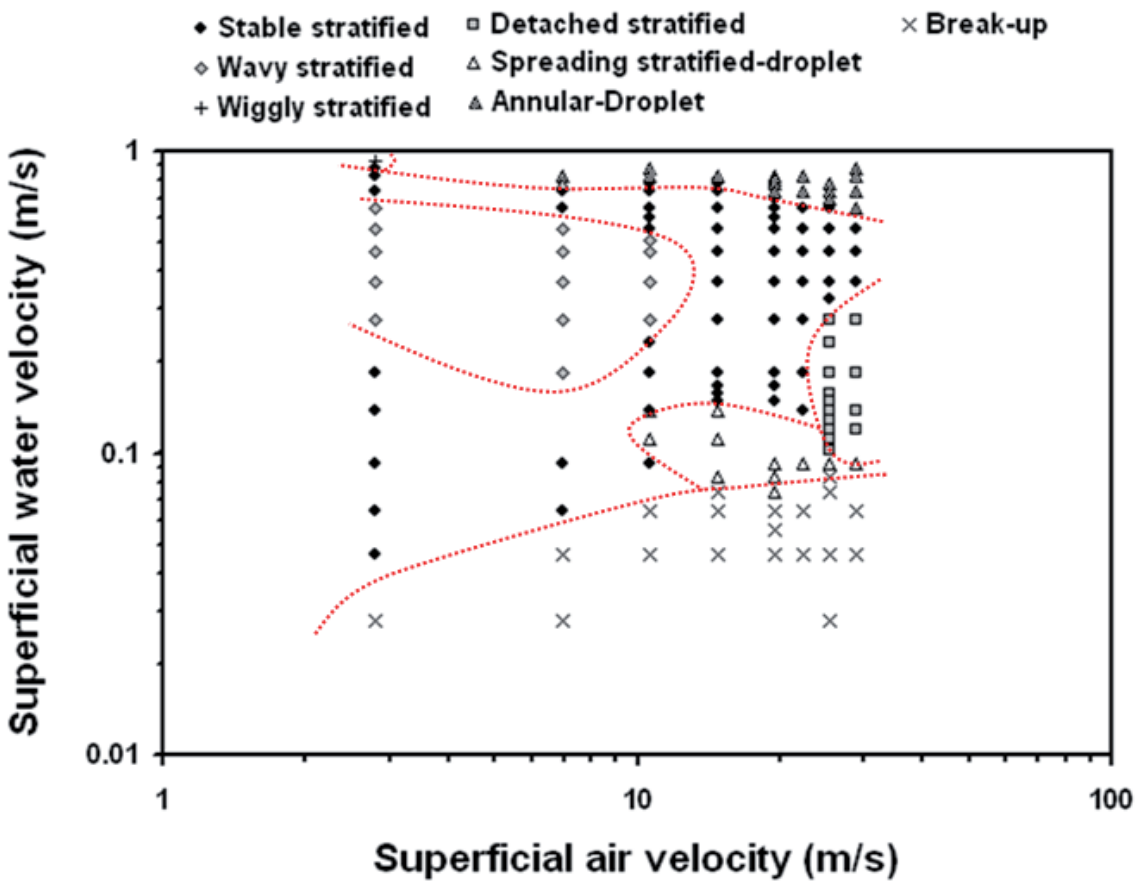

Figure 4.4. Flow regime map for the hydrophobic microchannel (contact angle = 111º). Dotted lines in the plot indicate transition boundaries.

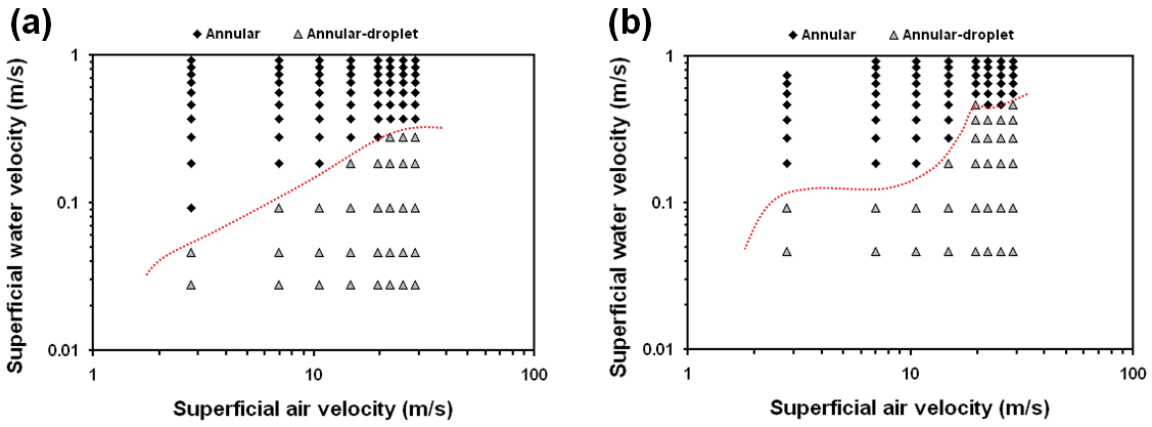

Figure 4.5. Flow regime maps for the hydrophilic microchannels. (a) Contact angle = 35º. (b) Contact angle = 77º. Dotted lines in the plot indicate transition boundaries.

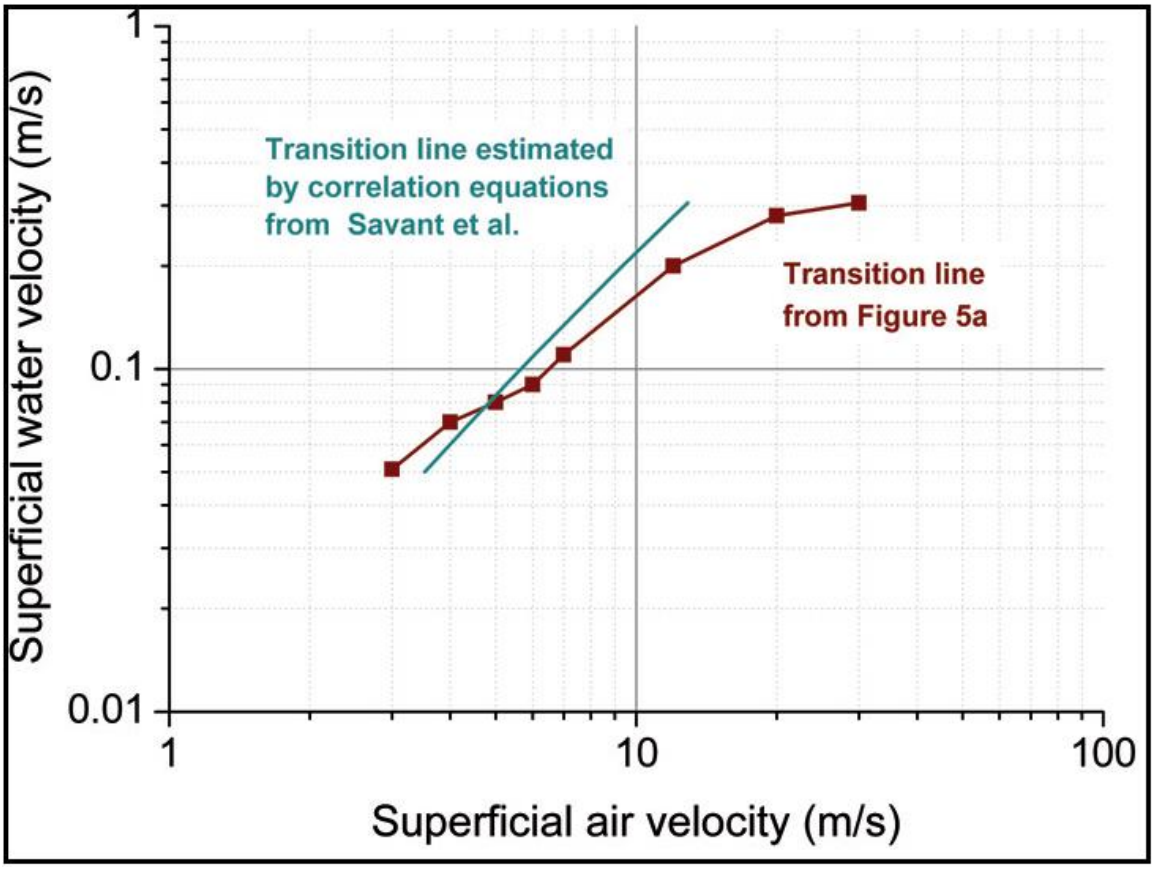

Figure 4.6. Comparison of flow regime transition boundary between pure annular and annular-droplet flow in the hydrophilic microchannel. The transition line estimated by the correlation equations from Savant et al [44] shows a similar trend characterized by a positive slope extending along the increasing superficial air and water velocities, in comparison to the transition line obtained from the experimental observations depicted in **figure 4.5**.

4.5 References

[1] Utada A S, Lorenceau E, Link D R, Kaplan P D, Stone H A and Weitz D A 2005 *Science* **308** 537

[2] Sugiura S, Nakajima M, Tong J H, Nabetani H and Seki M 2000 *J. Colloid Interface Sci.* **227** 95

[3] Zhang L, Koo J M, Jiang L, Asheghi M, Goodson K E, Santiago J G and Kenny T W 2002 *J. Microelectromech. Syst.* **11** 2002

[4] Song H, Chen D L and Ismagilov R F 2006 *Angew. Chem., Int. Ed. Engl.* **45** 7336

[5] Gunther A and Jensen K F 2006 *Lab Chip* **6** 1487

[6] Hibara A, Iwayama S, Matsuoka S, Ueno M, Kikutani Y, Tokeshi M and Kitamori T *Anal. Chem.* **77** 943

[7] Huh D, Tung Y-C, Wei H-H, Grotberg J B, Skerlos S J, Kurabayashi K and Takayama S 2002 *Biomed. Microdev.* **4** 141

[8] Huh D, Tkaczyk A H, Bahng J H, Chang Y, Wei H-H, Grotberg J B, Kim C-J, Kurabayashi K and Takayama S 2003 *J. Am. Chem. Soc.* **125** 14678

[9] Yen B K H, Gunther A, Schmidt M A, Jensen K F and Bawendi M G 2005 *Angew. Chem., Int. Ed. Engl.* **44** 5447

[10] Zheng B, Roach L S and Ismagilov R F 2003 *J. Am. Chem. Soc.* **125** 11170

[11] Dendukuri D, Tsoi K, Hatton T A and Doyle P S 2005 *Langmuir* **21** 2113

[12] Li W, Pharn H H, Nie Z, MacDonald B, Guenther A and Kumacheva E 2008 *J. Am. Chem. Soc.* **130** 9935

[13] Millman J R, Bhatt K H, Prevo B G and Velev O D 2005 *Nat. Mater.* **4** 98

[14] Zhao B, Viernes N O L, Moore J S and Beebe D J 2002 *J. Am. Chem. Soc.* **124** 5284

[15] Fuerstman M J, Garstecki P and Whitesides G M 2007 *Science* **315** 828

[16] Prakash M and Gershenfeld 2007 *Science* **315** 832

[17] Lau B T C, Baitz C A, Dong X P and Hansen C L 2007 *J. Am. Chem. Soc.* **129** 454

[18] Chen D, Du W, Liu Y, Liu W, Kuznetsov A, Mendez F E, Philipson L H and Ismagilov R F *Proc. Natl. Sci. Acad. USA* **105** 16843

[19] Li L, Mustafi D, Fu Q, Tereshko V, Chen D L, Tice J D and Ismagilov R F *Proc. Natl. Sci. Acad. USA* **103** 19243

[20] Clausell-Thormos J et al 2008 *Chem. Biol.* **15** 875

[21] Huebner A, Srisa-Art M, Holt D, Abell C, Hollfelder F, deMello A J and Edel J B 2007 *Chem. Cummun.* **12** 1218

[22] Boedicker J Q, Li L, Kline T R and Ismagilov R F *Lab Chip* **8** 1265

[23] Huh D, Fujioka H, Tung Y-C, Futai N, Paine R, Grotberg J B and Takayama S 2007 *Proc. Natl. Sci. Acad. USA* **104** 18886

[24] Taitel Y and Dukler A 1976 *AIChE J.* **22** 47

[25] Taitel Y, Bornea D and Dukler A 1980 *AlChE J.* **26** 345

[26] Suo M and Griffith P 1964 *J. Basic Eng.* **86** 576

[27] Brauner N and Moalem-Maron D 1992 *Int. Commun. Heat Mass Transfer* **19** 29

[28] Serizawa A, Feng Z and Kawara Z 2002 *Exp. Therm. Fluid Sci.* **26** 703

[29] Chung P M Y, Kawaji M, Kawahara A and Shibata Y 2004 *J. Fluids Eng.—Trans. ASME* **126** 546

[30] Triplett K A, Ghiaasiaan S M, Abdel-Khalik S I and Sadowski D L 1999 *Int. J. Multiph. Flow* **25** 377

[31] Fukano T and Kariyasaki A 1993 *Nucl. Eng. Des.* **141** 59

[32] Liu D and Wang S 2008 *Ind. Eng. Chem. Res.* **47** 243

[33] Chen L, Tian Y S and Karayiannis T G 2005 *J. Process. Mech. Eng.* **219** 167–81

[34] Chung P M Y and Kawaji M 2004 *Int. J. Multiph. Flow* **30** 735

[35] Damianides C A and Westwater J W 1988 *Proc. 2nd UK Natl. Conf. on Heat Transfer* **vol II** 1257–68

[36] Graska M L 1986 MS Thesis University of Illinois at Urbana-Champaign, IL

[37] Barajas A M and Panton R L 1993 *Int. J. Multiph. Flow* **19** 337

[38] Dreyfus R, Tabeling P and Willaime H 2003 *Phys. Rev. Lett.* **90** 144505

[39] Choi C and Kim M H 2008 *J. Micromech. Microeng.* **18** 105016

[40] Ishii M and Grolmes M A 1975 *AIChE J.* **21** 308

[41] Kataoka I, Ishii M and Mishima K 1983 *J. Fluid Eng.—Trans. ASME* **105** 230

[42] Ishii M and Mishima K 1989 *Int. J. Heat Mass Transfer* **32** 1835

[43] Pan L and Hanratty T J 2002 *Int. J. Multiph. Flow* **28** 363

[44] Savant P, Ishii M and Mori M 2008 *Nucl. Eng. Des.* **238** 1342

[45] Mikielewicz J and Moszynski J R 1976 *Int. J. Heat Mass Transfer* **19** 171

[46] EL-Genk M S and Saber H 2001 *Int. J. Heat Mass Transfer* **44** 2809

[47] Darhuber A A, Valentino J P, Troian S M and Wagner S 2003 *J. Micromech. Syst.* **12** 873

[48] Zhao B, Moore J S and Beebe D J 2001 *Science* **291** 1023

[49] Zhao B, Viernes N O L, Moore J S and Beebe D J 2002 *J. Am. Chem. Soc.* **124** 5284

[50] Abbott N L, Folkers J P and Whitesides G M 1992 *Science* **257** 1380

[51] Lafuma A and Quere D 2003 *Nat. Mater.* **2** 457

[52] Bodas D and Khan-Malek C 2007 *Sensor Actuatuators B* **123** 368

[53] Kreutzer M T, Gunther A and Jensen K 2008 *Anal. Chem.* **80** 1558

[54] De Mas N, Gunther A, Schmidt M A and Jensen K F 2009 *Ind. Eng. Chem. Res.* **48** 1428

CHAPTER 5

Dynamics of Liquid Plugs of Buffer and Surfactant Solutions in a Micro-Engineered Pulmonary Airway Model

We describe a bioinspired microfluidic system that resembles pulmonary airways and enables on-chip generation of airway occluding liquid plugs from a stratified air-liquid two-phase flow. User-defined changes in the air stream pressure facilitated by mechanical components and tuning the wettability of the microchannels enable generation of well-defined liquid plugs. Significant differences are observed in liquid plug generation and propagation when surfactant is added to the buffer. The plug flow patterns suggest a protective role of surfactant for airway epithelial cells against pathological flow-induced mechanical stresses. We discuss the implications of the findings for clinical settings. This approach and the described platform will enable systematic investigation of the effect of different degrees of fluid mechanical stresses on lung injury at the cellular level and administration of exogenous therapeutic surfactants.

5.1 Introduction

The airway tree of the lung consists of a branching network of tubes that become shorter, narrower, and more numerous as they penetrate deeper into the lung.[1] The airway is normally lined with a dynamic thin liquid film secreted and maintained by airway epithelial cells. Airways less than 1-2mmindiameter that include membranous, terminal, and respiratory bronchioles, as well as alveolar ducts are known as distal airways.[2] Due to their small size, distal airways are prone to closure at low lung volumes,[3] e.g., at the end of expiration. Pulmonary surfactant within the liquid lining film reduces the surface tension at the air-liquid interface of the airways and prevents airway collapse.[4,5] Abnormalities in biochemical and biophysical properties of surfactant cause instabilities of the air-liquid interface in various respiratory disorders[6-11] creating liquid plugs which obstruct airflow and impede gas exchange.[12] During inflation of the lung, the pressure associated with the inspired air moves the plug downstream. The plug leaves behind a trailing film as it propagates, becomes shorter when the trailing film is thicker than the precursor film,[13] and can eventually rupture re-establishing airflow. This process is known as "airway closure and reopening" and is schematically shown in **Figure 5.1a**. Computational models show that reopening of occluded airways exerts abnormal fluid mechanical stresses on airway walls that may damage the lining epithelial layer.[13-17] Liquid plugs may also form during clinical therapies such as mechanical ventilation (MV) and surfactant replacement therapy (SRT).[18-20] MV is used to support gas exchange for patients with a wide range of respiratory disorders. When the disorder is also accompanied by surfactant dysfunction, cyclic liquid plug mediated closure and subsequent reopening of airways happens that may exacerbate damage to epithelium.[21-23] In SRT, which involves administration of exogenous surfactant into patients' lungs through the endotracheal tube, homogeneous surfactant delivery usually requires a fast injection, which in turn results in the formation of a surfactant plug.[5,24] The plug is then propelled distally into airways during forced inspiration. There is also a great deal of

interest in using liquid plugs as vehicles for targeted drug delivery in various lung diseases.

Despite being implicated in a wide range of events in lungs, liquid plugs have not been studied experimentally in detail mainly due to the difficulty re-creating pulmonary airway-associated flows in vitro. Recently, our group developed a micro fluidic device consisting of a plug generator and a cell culture chamber. [25] Liquid plugs of phosphate buffered saline (PBS) were generated by switching off and on the air stream of a stratified air-liquid two-phase flow and subsequently propagated over a monolayer of epithelial cells under the air stream pressure. Although useful, this system lacked precise control and measurement of pressure levels, making it difficult to relate plug generation and propagation to physiological MV- and SRT-type applications where fine control over airway pressures is required. Here, we describe an automated microfluidic pulmonary airway model that is integrated with a computer-controlled on-chip plug generator and equipped with pressure sensors, solenoid valves, and flow meters to generate and monitor a wide range of airway pressures. This platform enables formation and propagation of liquid plugs of both PBS and, for the first time, surfactant-containing solutions with defined size and speed. Unlike most existing plug generating mechanisms that utilize two-phase flows in different channel configurations (e.g., a T-junction) and result in a "train" of liquid plugs within an air stream,[26,27] the study of liquid plug dynamics in lung airway models requires the flexibility of user-defined timing of formation and propagation of individual plugs.[28] The platform described here facilitates such fundamental investigations. Our analysis shows that channel surface wettability, air pressure, and fluid properties determine flow configurations during both plug generation and propagation events. More importantly, we demonstrate that exogenous surfactants provide protective coating films on airway walls and reduce flow instability-induced airway closure.

5.2 Experimental Section

5.2.1 Fabrication of the Microfluidic Device

The micro fluidic device consisted of two poly(dimethylsiloxane) (PDMS) chambers separated by a porous polyester membrane of 3 μm pore size, which mimics the basement membrane in vivo (**Figure 4.1b**). The dimensions of top and bottom microchannels were 350 μm X 85 μm and 550 μm X 85 μm, respectively. Both layers were fabricated using soft lithography. [29] Prepolymer (Sylgard 184, Dow-Corning) at a 1:10 curing agent-to-base ratio was cast against positive relief features to form a negative replica of microchannels. The relief features were composed of SU-8 (MicroChem, Newton, MA) and fabricated on a thin silicon wafer using conventional photolithography. The prepolymer was cured at 60ºC overnight. After cutting out the channel features, holes to microchannels were punched using a 1.5 mm Biopsy punch (Miltex).

We used a stamping method to assemble the two PDMS layers and the porous membrane.[30] PDMS prepolymer was diluted 1:2 in toluene and spin-coated at 1000 rpm for 1 min on a glass slide to form a thin layer of PDMS glue. Top and bottom layers of the device were stamped against the glue. The porous membrane was carefully placed on the bottom layer microchannel, and small amounts of the glue were applied to the edges of the membrane using a pipet tip. Then, the two layers were carefully aligned under a microscope and the assembly was left at ambient temperature for ~1 h to de-gas. The device was cured at 60ºC overnight. Finally, 14-gauge bent blunt needles (Becton Dickinson) were attached to silicone tubing (Fisher Scientific) of 10-15 cm and connected to inlet and outlet ports of air and liquid on the device using epoxy glue (ITW Performance Polymers). The fabrication procedure ensures robust leakage-free bonding.

5.2.2 Wettability of Microchannels

PDMS is intrinsically a hydrophobic material. To change the wetting properties of microchannels, we exposed devices to radiofrequency oxygen plasma (SPI Supplies) for time periods of 15, 20, and 25 min.[31] Plasma treatment was performed after attaching all tubings to micro fluidic devices. To verify uniformity of plasma treatment along the length of the droplet observation region of microchannels, we estimated contact angles of liquid plugs in these devices and found that increasing the duration of plasma treatment changed the contact angle from ~83º to ~73º to ~65º, respectively. Contact angles were estimated by extracting the profile of liquid plugs from experimental images using a freeware program, ImageJ (NIH), and subsequently fitting a tangent to the extracted profile at the point of contact with the channel wall.

5.2.3 Working Fluids and Viscosity and Surface Tension Measurements

We selected three different working fluids: (i) Dulbecco's Phosphate Buffered Saline (PBS, Gibco), (ii) a 5 mM Tween 20 (Sigma) surfactant solution in PBS, and (iii) a natural lung surfactant, Survanta, with a concentration of 1.0 mg/mL in PBS. Liquid viscosity was measured using a U-tube viscometer (Ostwald). Surface tension of liquids was determined byDu Nouy ring method (Kruss).

5.2.4 Experimental Setup Design

The experimental setup of the plug generator is shown in **Figure 5.1c**. In all experiments, liquid flow rate was fixed at 10 mL/h and the source pressure of the air was adjusted to 10 psi using a pressure regulator on the air tank. An air flow meter (Cole-Parmer) installed upstream of the air inlet port of the microfluidic device significantly reduced the pressure of air supplied to the device. To generate liquid plugs on-chip, liquid was pumped into the K-shaped top microchannel using a syringe pump (KD Scientific) and was focused by compressed air stream to form a stratified air-liquid flow where the two streams flow side-by-side (**Figure 5.2a-1**). Using a programmable solenoid pinch

valve (Cole-Parmer) to close tubing connecting an air source to the plug generator, the airflow was blocked for a very short predefined period of time (≥30 ms), allowing the liquid to spread and progress toward the main channel (**Figure 5.2a-2**). Recovery of the airflow re-established the stratified flow and pinched off a liquid plug that propagated downstream the main channel (**Figure 5.2a-3**). To gain precise control over liquid plug dynamics and to mimic physiologic airway pressures, we used a sensitive pressure controlling mechanism that consisted of a small piece of plastic tubing glued to a 1 mL pipet tip at one end and placed between tunable squeeze jaws at the other end (**Figure 5.1c**). This assembly was connected to the tubing at the outlet of the top chamber. A differential pressure transducer (Omega Engineering) was incorporated in the system to monitor the pressure difference, ΔP, between the inlet port of the air stream (P_1) and the outlet port of the top channel (P_2). Any change in air and liquid flow rates or fine-tuning the closure of the squeeze jaws changed pressure within the system. The transducer translated this differential pressure into an electric voltage, which was measured using a data acquisition (DAQ) board. The voltage data were converted to pressure data using manufacturer's tables.

5.2.5 Data Analysis

The device was placed under a conventional bright field microscope (TS100, Nikon) during the experiment. Images and videos were captured using a Hamamatsu camera (Orca-ER) mounted on the microscope. ImageJ was used to analyze the images.

5.3 Result and Discussion

For a liquid of known physical properties, we identified two main parameters that affect the plug generation process (assuming fixed channel dimensions and a constant liquid flow rate): differential pressure between the air inlet and the outlet port downstream of the main channel and wettability of the channel walls. These are discussed in the next two sections. Additionally, liquid surface tension is an important parameter in lung physiology. We use PBS and Survanta as working fluids to examine this point in the context of plug generation and propagation events in two separate sections following. Finally, we discuss clinical implications of the findings.

5.3.1 Differential Pressure

The baseline value of the differential pressure, ΔP, was adjusted by varying the airflow rate, the liquid flow rate, or the closure time of the pinch valve while keeping the closure of the squeeze jaws of the pressure controlling mechanism fixed. By varying the airflow rate, a large range of pressures including both physiologic transpulmonary pressures ($\Delta P <\sim 0.5$ psi)[32] and abnormally larger nonphysiologic pressures[33] were accommodated in the microfluidic airway model (Supporting Information, **Figure SI.1a**). We found that ΔP was hardly sensitive to changes in the liquid flow rate (Supporting Information, **Figure SI.1b**) and therefore kept the liquid flow rate constant in all experiments and varied ΔP by changing the airflow rate. To examine pressure changes in the channel during generation and propagation of a liquid plug, we analyzed a typical pressure profile. Initially, when both air and liquid flow at constant rates of 35 cm^3/min and 0.167 cm^3/min, respectively, to form a stratified flow, ΔP has a constant baseline value of ~0.3 psi (region A in **Figure 5.2b** corresponding to **Figure 2a-1**). Closing off the pinch valve for 30 ms blocks the airflow momentarily, causing air pressure to build up behind the pinch valve due to the flow of air upstream of the pinch valve. The differential pressure rises sharply and reaches a peak value, ΔP_{peak}, about 50% larger than the baseline value in this case (region B in **Figure 5.2b**). Once the pinch valve is reopened, the air pressure pushes the liquid column of the side channel toward the waste reservoir and the main channel. The stratified flow is recovered and a plug forms in the

main channel (**Figure 5.2a-3**). The pressure drops considerably, yet to a value larger than the baseline pressure (region C in **Figure 5.2b**). This difference reflects resistance to the airflow in the main channel due to the presence of the liquid plug and indicates that, in vivo, occluded lung airways that exist at the beginning of the inspiration cycle require a larger pressure to expand, causing small lung compliance.[32] The pressure remains at this level as the plug propagates downstream of the channel and finally returns back to its baseline value after the plug is cleared from the channel (region D in **Figure 5.2b**). This situation resembles an increase in the lung compliance after collapsed lung units are reinflated (recruitment).

Reopening of the pinch valve is the onset of the plug generation process when the maximum inlet air pressure, and hence ΔP_{peak}, directly affects the flow at the K-junction of the device by pushing the liquid column (**Figure 5.2a-2**) toward the main channel and the waste reservoir. Due to its larger resistance, the main channel is filled with less liquid compared to the channel leading to the waste reservoir. It will be shown below that, at a constant liquid flowrate, ΔP_{peak} directly correlates with the size of liquid plugs (see **Figure 5.4**). The increase in the liquid plug size with ΔP_{peak} is due to the ease of reinitiating flow into the air-filled main channel compared to the liquid-filled side channel. We obtained a wide range of ΔP_{peak} by (i) changing the baseline air pressure and (ii) duration of closure of the pinch valve (Supporting Information, **Figure SI.2a**).

5.3.2 Surface Wettability of Microchannels

Because of the large surface area-to-volume ratios, surface wettability is a critical parameter in microscale air-liquid two-phase flows. That is, one cannot simply control ΔP_{peak} and fluid flow rates and expect the same plug size in microchannels of differing wettabilities. We thus evaluated the role of wettability of microchannel surfaces using two sets of identical devices with different wettabilities: A microfluidic device was rendered hydrophilic by exposure to oxygen plasma for 25 min and a hydrophobic device without any plasma treatment. To verify differences in surface properties, a PBS plug

was formed in each device and advanced slowly using an extremely low airflow to ensure that the front meniscus attains an advancing contact angle.[34] Plugs generated in the plasma treated device yielded a much smaller contact angle, confirming hydrophilicity of channel surfaces (cf. **Figure 5.3a,b**). Next, we performed plug generation experiments with hydrophobic and hydrophilic devices using similar air and liquid flow rates and the pinch valve closure time. As shown in Figure **5.3c,d**, larger plugs are generated in the hydrophilic device compared to the hydrophobic one under similar test conditions. We calculated the solid-liquid interfacial tension (γ_{sl}) in these two systems to explain this observation:

The surface tension of PBS is similar to that of water at room temperature, γ_{lv}= 72.2 mJ/m^2, and therefore, a similar contact angle (θ) is found on hydrophobic PDMS, i.e., ~105º (**Figure 5.3a**).[35] We also estimated that the PBS contact angle on hydrophilic PDMS surface is ~65º (**Figure 5.3b**). To calculate γ_{sl}, first we invoke Young's equation

$$\gamma_{lv}\cos\theta = \gamma_{sv} - \gamma_{sl} \qquad \text{(eq 1)}$$

and an equation of state for interfacial tensions

$$\gamma_{sl} = \gamma_{lv} + \gamma_{sv} - 2\sqrt{\gamma_{lv}\gamma_{sv}}\,e^{-\beta(\gamma_{lv}-\gamma_{sv})^2} \qquad \text{(eq 2)}$$

In eq 2, γ_{lv}, γ_{sv}, and γ_{sl} represent liquid surface tension, solid surface tension, and solid-liquid interfacial tension, respectively, and β = 0.000125 (mJ/m^2)$^{-2}$ is an experimental constant.[36,37] Combining the above equations gives

$$\mathrm{Cos}\theta = -1 + 2\sqrt{\gamma_{sv}/\gamma_{lv}}\,e^{-\beta(\gamma_{lv}-\gamma_{sv})^2} \qquad \text{(eq 3)}$$

Using known values of γ_{lv} and θ, eq 3 is used to first calculate γ_{sv} for both systems: $\gamma_{sv,hydrophobic}$ = 19.8 mJ/m^2 and $\gamma_{sv,hydrophilic}$ = 44.0 mJ/m^2. Subsequently, Young's equation is solved for γ_{sl} using γ_{sv}, γ_{lv}, and θ values of each system. This yields $\gamma_{sl,hydrophobic}$ = 38.5 mJ/m^2 and $\gamma_{sl,hydrophilic}$ = 13.6 mJ/m^2.

This analysis shows that the solid-liquid interfacial tension, which is the energy required to create a unit area of solid-liquid interface, is significantly larger for the hydrophobic system. Therefore, under similar test conditions, the hydrophobic device results in a smaller solid-liquid contact area (i.e., a shorter plug).

5.3.3 Quantification of Plug Generation with PBS and Surfactant Solutions at Different Surface Wettabilities and Peak Differential Pressures (ΔP_{peak})

We first used PBS as the working fluid to study plug generation in three sets of micro fluidic devices with different channel wall surface tensions (γ_{sv}) of 33.2, 39.4, and 44.0 mJ/m^2, obtained by oxygen plasma treatment for 15, 20, and 25 min, respectively. The experiments were performed over a wide range of peak differential pressure, ΔP_{peak} < 1.0 psi. These conditions enabled us to study simultaneously the combined effect of surface wettability and ΔPpeak on plug generation. We found a critical pressure (ΔP_c ~0.22 psi) below which PBS plugs do not form; but rather, small droplets of large curvature are deposited on the channel walls. At $\Delta P_{peak} \geq \Delta P_c$, sufficient volume of PBS entered the main channel to generate a plug across channel walls. Above the critical pressure level, in all three devices, the plug size initially increased linearly with the peak differential pressure up to a certain pressure threshold (**Figure 5.4a**). At a given pressure, larger plugs form in more hydrophilic channels (larger slope for diamonds than squares and triangles in **Figure 5.4a**) due to a smaller solid-liquid interfacial tension, γ_{sl}, in these systems, as explained above and corroborated by non-dimensionalizing the peak differential pressure with respect to γ_{sl} that results in the collapse of all three series of data points toward a linear band (Supporting Information, **Figure SI.3**).

At a certain pressure threshold, further increase of ΔP_{peak} does not yield larger plugs, but rather, multiple plugs are generated (**Figure 5.4b**). To understand this phenomenon, we performed video imaging of the process. As pressure increases, instabilities of the two-phase flow during reopening of the air stream leave small liquid residues on channel walls, in addition to the generated liquid plug. At pressures below the

threshold value, the residues are small and remain immobile under the airflow. However, higher air pressures generate larger residues that move toward the entrance of the main channel and merge to form a second and even a third plug (**Figure 5.4b** and Supporting Information, video SI.1).

We also evaluated the plug generation process by varying ΔP_{peak} using different valve closure times. The size of PBS plugs continuously increased with ΔP_{peak} up to ~0.45 psi that corresponds to a valve closure time of ~500 ms (Supporting Information **Figure SI.2b**). Thereafter, the plug size only changed marginally, because at valve closure times greater than 500 ms, increase in the peak pressure significantly slows down (Supporting Information **Figure SI.2a**).

Surfactant is a critical component of the respiratory system for normal function of the lung. During clinical events such as SRT, surfactant plugs can form in upper airways. To evaluate formation of pulmonary surfactant plugs, we used Survanta as the working fluid. Survanta, a clinical exogeneous surfactant, is an extract of minced bovine lung tissue to which certain components are added to mimic surface tension-lowering properties of natural lung surfactant. [38] We used a hydrophilic device with γ_{sv} = 44.0 mJ/m^2 in a pressure range similar to the PBS tests, i.e., ΔP_{peak} < 1.0 psi. This surface wettability condition was selected because it more closely mimics hydrophilic airways in vivo. Similar to PBS, Survanta plugs do not form below a critical pressure level. However, this minimum is larger for Survanta ($\Delta P_c \sim$ 0.29 psi). We observed that, unlike PBS, Survanta always tends to spread on channel walls rather than forming fairly round droplets. Therefore, it takes a larger pressure and a greater volume of liquid to generate a Survanta plug. This delayed plug formation is mediated by the low surface tension of Survanta ($\gamma_{Survanta}$ = 25.0 mJ/m^2 vs γ_{PBS} = 72.2 mJ/m^2) and a resulting low γ_{sl} and supports a protective role of surfactant against airway closure due to flow instabilities. Above the critical pressure, the plug length increases linearly with pressure up to ~0.65 psi (**Figure 5.4a,c**). Under similar pressure and wettability conditions, Survanta plugs are always shorter than PBS plugs (c.f. circles and diamonds in **Figure 5.4a**) because a significant volume of Survanta entering into the main channel spreads on the walls behind the plug.

As pressure increases to ΔP_{peak} > 0.65 psi, Survanta deposition becomes even more significant and the plug size remains fairly constant (**Figure 5.4a,c**). Spreading of Survanta is also the key factor preventing multiple plug formation, as opposed to the surfactant-free PBS solution.

5.3.4 Propagation of PBS and Surfactant Solution Liquid Plugs

Subsequent to the formation of liquid plugs, the inspired air pressure drives the plug along the airway. Understanding this process in detail and the ability to systematically manipulate it is important to events such as plug-mediated airway injury and SRT. Questions that have largely been studied numerically and yet require experimental analysis are differences in the propagation dynamics of buffer and surfactant solution plugs under similar channel wettability and driving pressure,[13, 39, 40] conditions mediating rupture of liquid plugs,[15] and correlation between plug size and speed.[15]

We tested both PBS and a 5 mM solution of Tween 20 as a model surfactant in hydrophilic microfluidic devices. A key observation was that, unlike PBS plugs, the rear meniscus of model surfactant plugs deposited a thin film on channel walls (cf. **Figure 5.5a and b**) and the plug length decreased approximately 60%over a distance of~6.7mm. We monitored the displacement of front meniscus (X_{front}) and rear meniscus (X_{rear}) of the surfactant plug from an origin point in the main channel where plug propagation starts. The displacement of both menisci followed quadratic polynomial relations, and the data suggested that the rear meniscus propagated slightly more rapidly than the front one (**Figure 5.5c**). This experiment is consistent with a previous observation [28] and suggests that plug rupture is due to a faster rear meniscus eventually catching up with the front one. Equating the displacement equations gave the time of the surfactant plug rupture in the channel, t = 36.45 s. Using this value, the site of plug rupture is estimated from the displacement equations to be ~10.9mm downstream from the origin point. This estimate is valid for a straight, homogeneous channel only. Our micro fluidic setting contains a

porous membrane downstream from the channel allowing liquid to purge through the membrane, complicating dynamics of plug propagation/rupture. Nevertheless, in the presence of a monolayer of differentiated epithelial cells on the membrane, the channel can still be considered homogeneous because cell-secreted tight junctional proteins limit paracellular (passive) fluid transport, and therefore, the above estimate should still remain valid (see Supporting Information, **Figure SI.4**). Thus, this microfluidic platform enables generation of well-defined liquid plugs that can be ruptured at a predetermined region over a cell monolayer to investigate the extent of damage to airway cells solely due to plug rupture and distinguish it from that caused by plug propagation.

The variation of surfactant plug length over time was deduced from differences between front and rear menisci displacements of Tween plugs. The result in **Figure 5.5d** indicates that the plug length decreases nonlinearly with time and the plug speeds up as it becomes shorter (circles). This observation indicates that, under a constant driving air pressure, larger plugs propagate more slowly, most likely due to a stronger viscous resistance, consistent with a recent numerical investigation of unsteady propagation of liquid plugs in a straight tube.[15] Unlike surfactant-containing plugs, PBS plugs did not deposit a detectable trailing film (diamonds). Interestingly, we also found that the propagation of surfactant plugs is associated with the formation of a precursor film that moves ahead of the contact line of the front meniscus of the plug on the microchannel surface (**Figure 5.5e** and Supporting Information, video SI.2). The precursor film formation is likely due to interactions between surfactant head groups and the hydrophilic surface of the channel.[41]

Propagation speed of liquid plugs is another key parameter that influences both the outcome of SRT and airways cell injury due to pathological liquid plugs. To demonstrate the utility of our in vitro platform for such studies, we examined PBS and 5 mM Tween 20 surfactant plug propagation at different speeds realized by tuning the pressure of driving air while keeping other parameters fixed. Under a constant driving air pressure and assuming steady plug propagation, plug speed was obtained by dividing plug displacement over a certain distance with the propagation time. The results in

Figure 5.6 show that PBS plugs propagated about 2.5 times faster than surfactant plugs under similar driving pressures, consistent with computational data.[40] Increasing the driving pressure from ~0.15 to 0.32 psi changes the speed of PBS plugs from 1.9 mm/s to 5.3 mm/s, whereas the speed of surfactant plugs increases from 0.7 mm/s to 2.2 mm/s. The capillary number in these experiments is on the order of 10^{-5}, showing that the flow is surface tension dominant.

We note that the described platform allowed us to experimentally study fundamental liquid plug dynamics that, until now, have been primarily the realm of computational analysis. Our experimental data verified computational findings about differences in propagation dynamics of buffer and surfactant solution plugs in terms of trailing and precursor film deposition and plug speed under similar test conditions, as well as correlation between size and speed of liquid plugs and nonlinear increase in plug speed with increase in driving air pressure.[40]

5.3.5 Clinical Implications

Flow instabilities under large air pressures (~>0.5 psi) led to the formation of PBS drops (residues) of high curvature on channel walls that resulted in multiple occluding liquid plugs. This experiment cautions the use of large ventilation pressures in patients with surfactant deficiency.[42] The fact that PBS plugs propagated along the length of the channel without forming trailing or precursor films on the channel walls reinforces this consideration. This is because the largest mechanical forces on airway walls due to plug propagation are always generated at thin front and rear menisci,[13] and such abnormal forces may cause significant damage to airway cells.

We showed that, unlike PBS, Survanta plug formation required a larger pressure. Furthermore, under flow instabilities at high air pressures (~0.5 - 0.9 psi), 1.0 mg/mL physiologic surfactant prevented formation of trailing plugs; rather, Survanta always spread on the channel walls. This is consistent with earlier benchtop experiments and

computational models that suggested a stabilizing effect for surfactant delaying meniscus formation in rigid airway models by a factor of 4-5 compared to surfactant free solutions.[4,43,44] Thus, the clinical benefits of providing exogenous surfactant to patients is in part to maintain airway patency and protect the epithelial lining cells from the damaging forces of repetitive opening and closing.

Propagation of surfactant plugs was also quite different from PBS plugs and was always accompanied by the formation of a trailing film due to deposition onto channel walls and a precursor film moving ahead of the plug. Measurements of viscosity and surface tension of PBS and Tween 20 helped explain the difference. Both liquids have a low viscosity (μ_{PBS}=1.00 cP and μ_{Tween} = 1.07 cP), whereas the 5 mM Tween 20 solution has a significantly lower surface tension (γ_{Tween} = 37.4 mJ/m^2) compared to PBS (γPBS=72.2 mJ/m^2). This indicates that formation of surfactant films on hydrophilic channel walls is mediated by a low surface tension, which most likely is due to adsorption of surface-active molecules at the air-liquid interface of the surfactant plug. This is consistent with findings from numerical models that suggest a decrease in the surface tension of the working fluid correlates with an increase in the film thickness.[15] Presence of the precursor and trailing surfactant films is thought to protect airway cells against mechanical stresses of nonphysiologic flows. Indeed, numerical models show that surfactant mitigates mechanical forces (pressure, shear stress, and their gradients) on airway walls and the peak values of these forces decrease as the film thickness increases.[16, 40]

Airways are accessible paths for the delivery of genetic materials and drug molecules to treat genetic lung diseases such as cystic fibrosis and arrest the progression of lung cancer. Surfactant liquid plugs are considered potential drug delivery vehicles in the lung. However, the success of such treatments will greatly depend on the accuracy of targeted delivery of liquid plugs to airways.[45] On the basis of a moderate driving pressure of ~0.3 psi in this in vitro model, we showed that the site of rupture of surfactant plugs can be estimated from plug displacement equations. Our approach and automated

platform will facilitate studies of targeted drug and gene delivery to predetermined regions of the lung airway tree.

Another key observation relevant to SRT in clinics was that increasing the driving air pressure caused faster propagation of surfactant plugs and resulted in rupture of the plug earlier in the channel due to a more significant deposition onto channel walls (note: trailing film thickness is proportional to plug speed).[5] This highlights the importance of delivery of exogenous surfactant to patients at moderate pressures to prevent premature rupture of surfactant plug and incomplete delivery, validating predictions from existing computational data. [39] Thus, our approach may be utilized to define optimum conditions for SRT to ensure that sufficient volume of surfactant reaches conducting airways to allow uniform surfactant distribution on airway walls.

5.4 Conclusions

We presented a microengineering approach to model the architecture of pulmonary airways and study associated liquid plug flows. Using computer-controlled mechanical components, liquid plugs of buffer and surfactant solutions with user-defined size and propagation speed were generated. We correlated formation and propagation of liquid plugs with physical properties of working liquids, wettability of channel walls, and pressure of the air stream. A minimum critical pressure was required to initiate plug generation, and this minimum was larger when surfactant was added to PBS. For a fixed surface wettability, increasing the baseline pressure, and hence the peak differential pressure, generated larger PBS plugs up to a certain pressure threshold; thereafter, multiple liquid plugs formed due to increased flow instabilities. A physiologic surfactant solution, Survanta, behaved quite differently from PBS. The plug size initially increased with pressure, but further increases in pressure, which caused larger flow instabilities, did not lead to the formation of additional trailing plugs. The addition of Survanta in hydrophilic channels mimics normal lung airways, and these results suggest a critical role

for pulmonary surfactant in maintaining airway patency. In contrast to PBS alone, propagating surfactant plugs gave rise to trailing and precursor films. Such surfactant coatings on airway walls may serve to protect airway tissue against mechanical stresses associated with nonphysiologic flow conditions. Generation of well-defined surfactant-containing plugs in an in vitro platform is a new capability that will serve various studies in pulmonary research involving surfactants.

Our microfluidic airway model is a flexible in vitro platform that accommodates quantitative investigations of liquid plug dynamics by independently varying components that comprise the air-liquid interface in the lung. The findings and the proposed platform will help design and perform in vitro tests to understand cellular-level effects of liquid plugs in airways and the efficacy of preventive and treatment strategies, such as SRT, for various respiratory disorders.

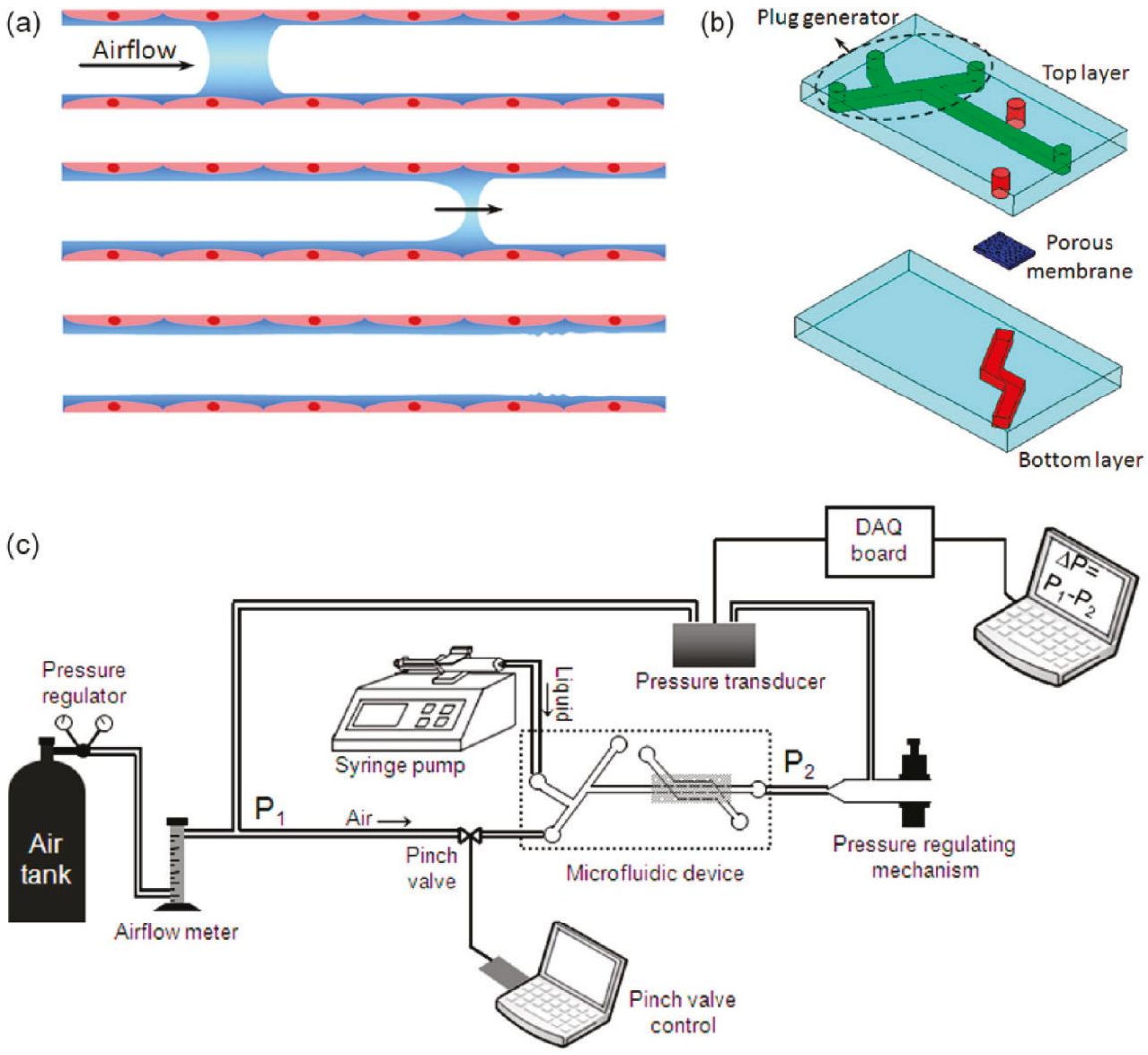

Figure 5.1. (a) Schematic of the obstruction of surfactant-deficient airways by liquid plugs. The plug moves downstream from the airway due to the inhaled air pressure and eventually ruptures. (b) Schematic of the two-layer microfluidic device. (c) Schematic of the computerized liquid plug generating experimental setup.

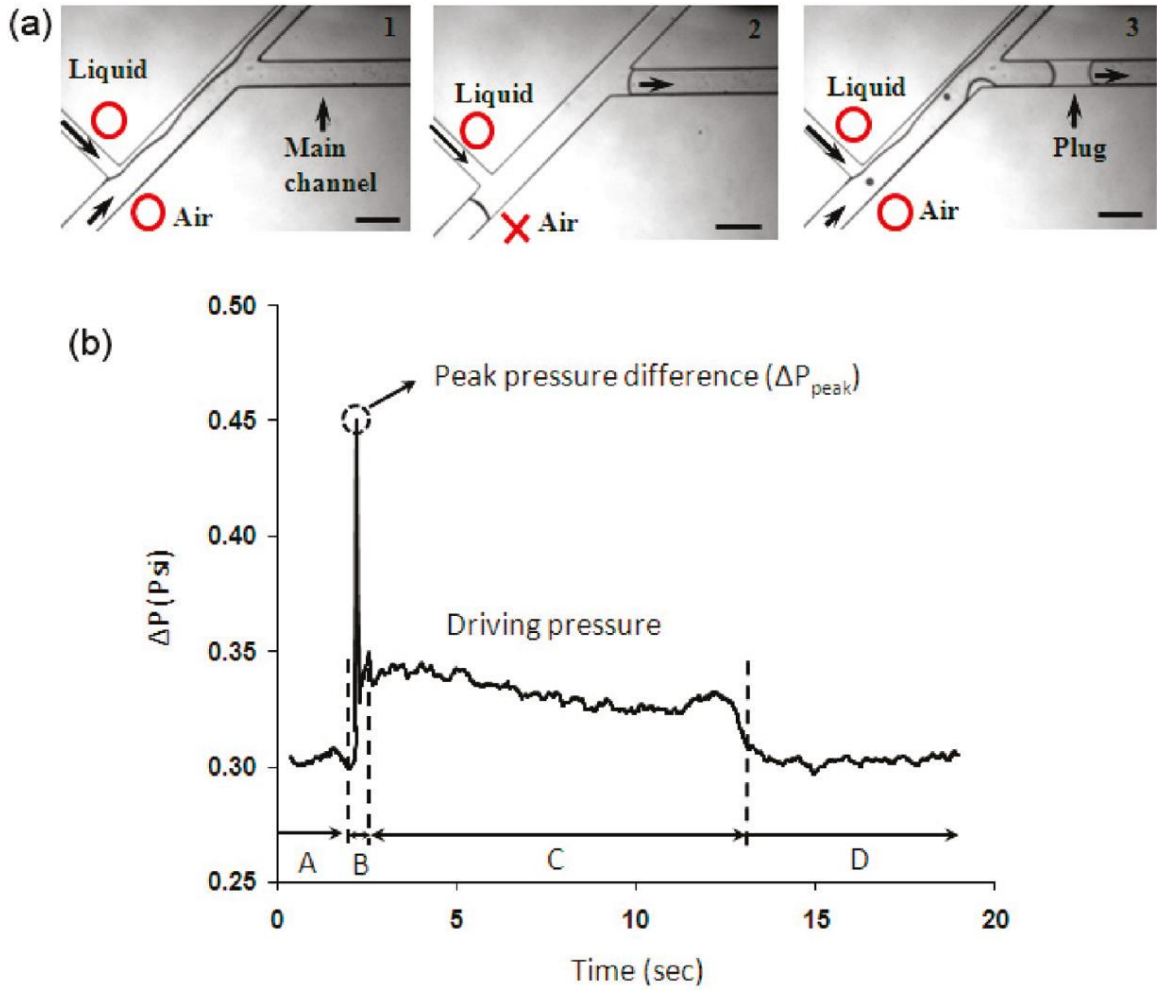

Figure 5.2. (a) Sequence of events during formation of liquid plugs. Open circle and cross symbols denote open and closed states of flows (scale bar 350 μm). (b) Typical pressure profile in the course of one plug generation/propagation event.

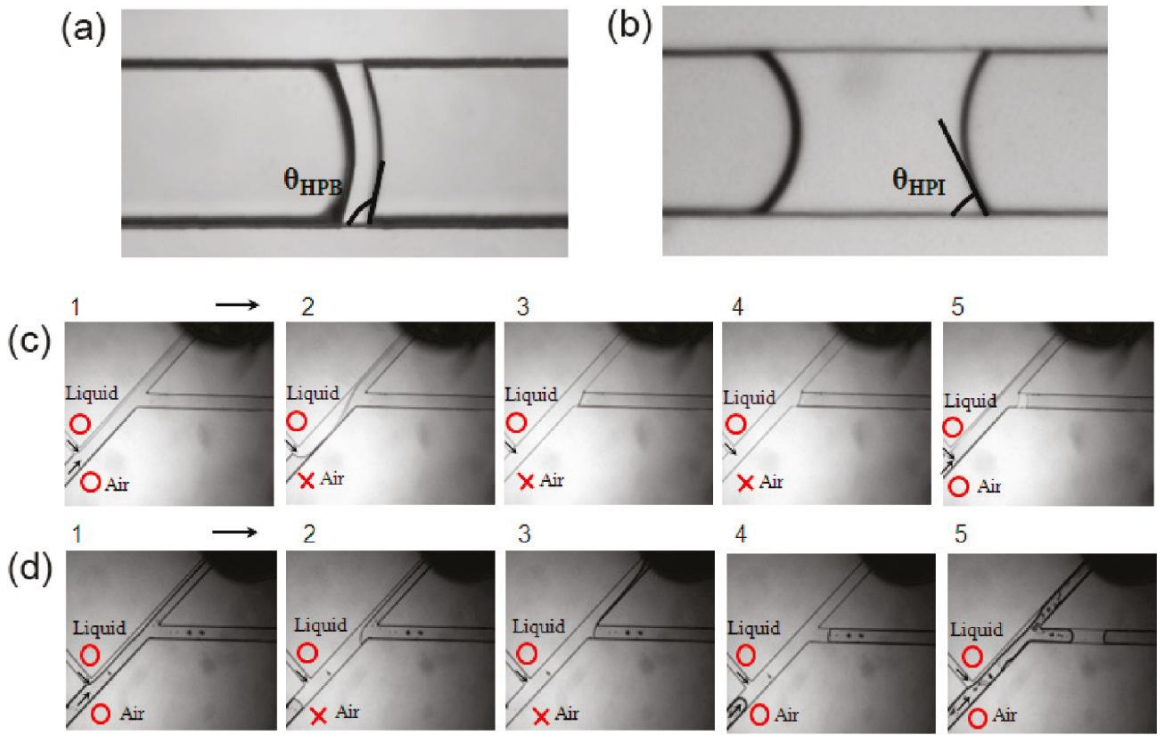

Figure 5.3. Advancing contact angles of PBS plugs in (a) hydrophobic and (b) hydrophilic PDMS microchannels, respectively. Plug generation in (c) hydrophobic and (d) hydrophilic microchannels, respectively, under similar test conditions.

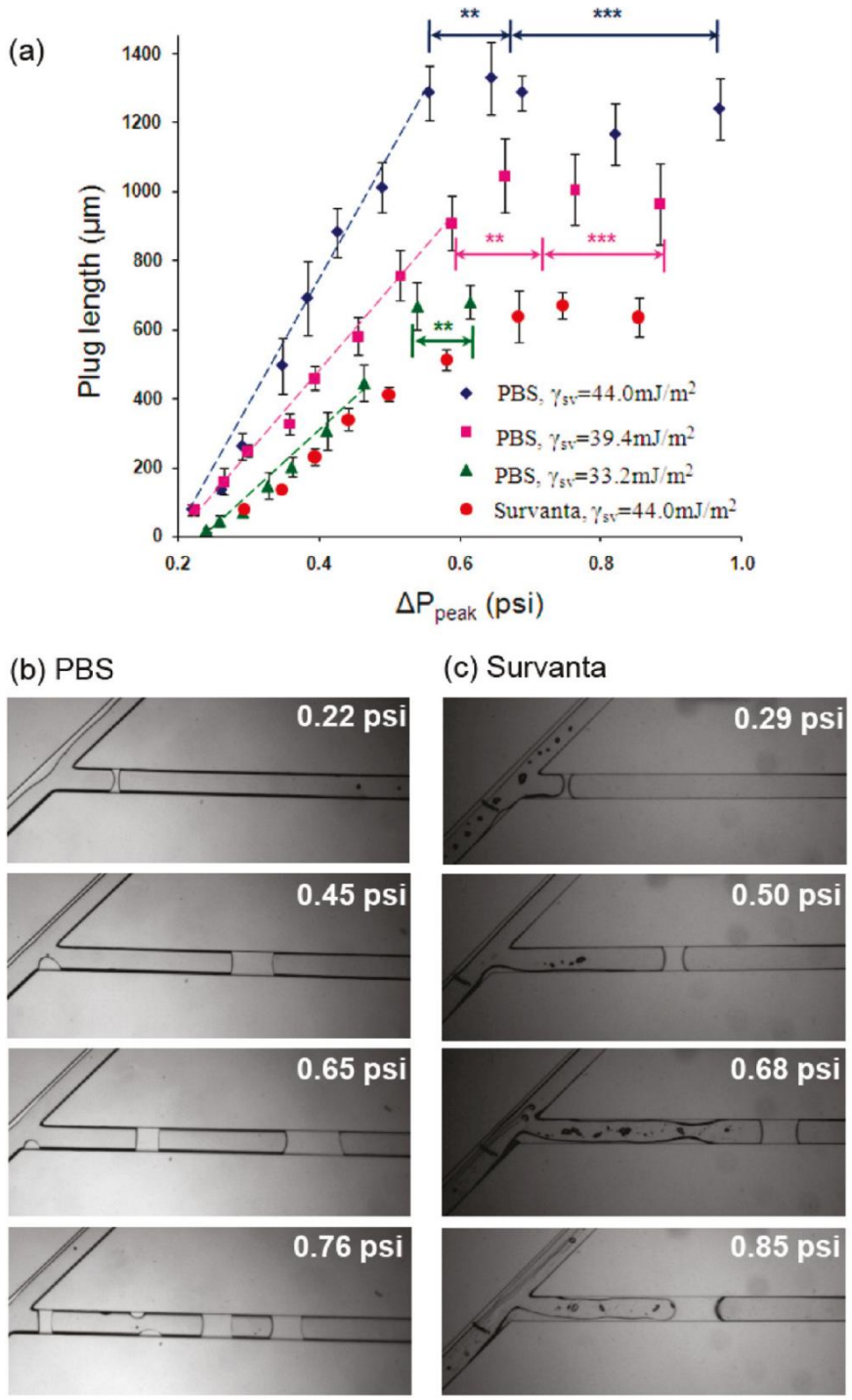

Figure 5.4. (a) Influence of channel surface wettability and peak differential pressure on the length of liquids plugs of PBS (diamonds, squares, and triangles) and Survanta (circles). (b)Continuous increase in pressure causes formation of double and triple PBS plugs (noted by asterisks). (c) Flow instabilities at similar pressure conditions do not generate trailing Survanta plugs.

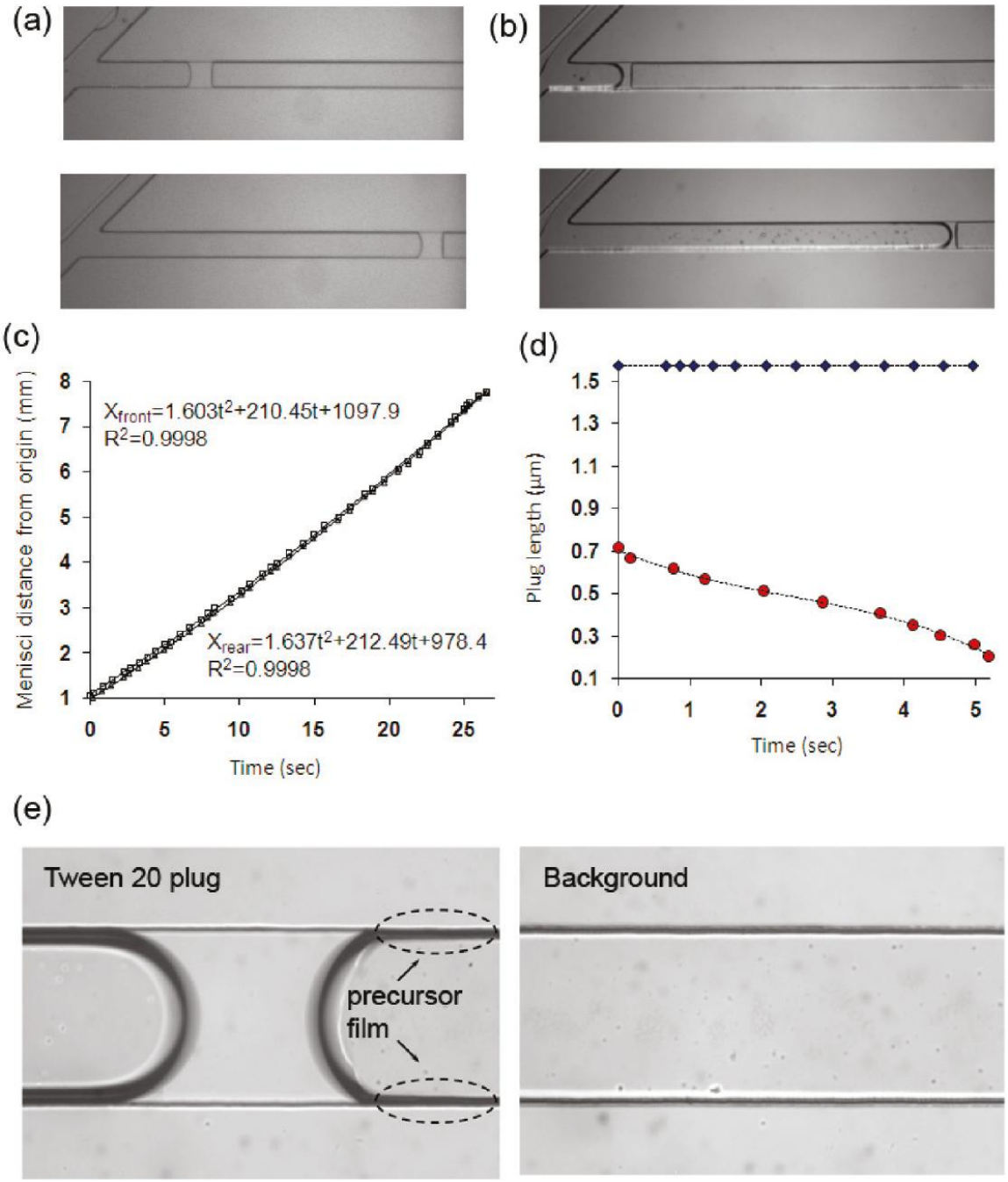

Figure 5.5. (a) PBS plugs propagate without detectable deposition onto channel walls, whereas (b) surfactant-containing plugs deposit a thin trailing film. (c) Displacement of front and rear menisci of the surfactant plug in (b). (d) Variation of PBS (diamonds) and surfactant (circles) plug length due to deposit on channel walls. (e) Precursor film forms ahead of contact line of front meniscus of the propagating surfactant containing plug (compare to the background channel image).

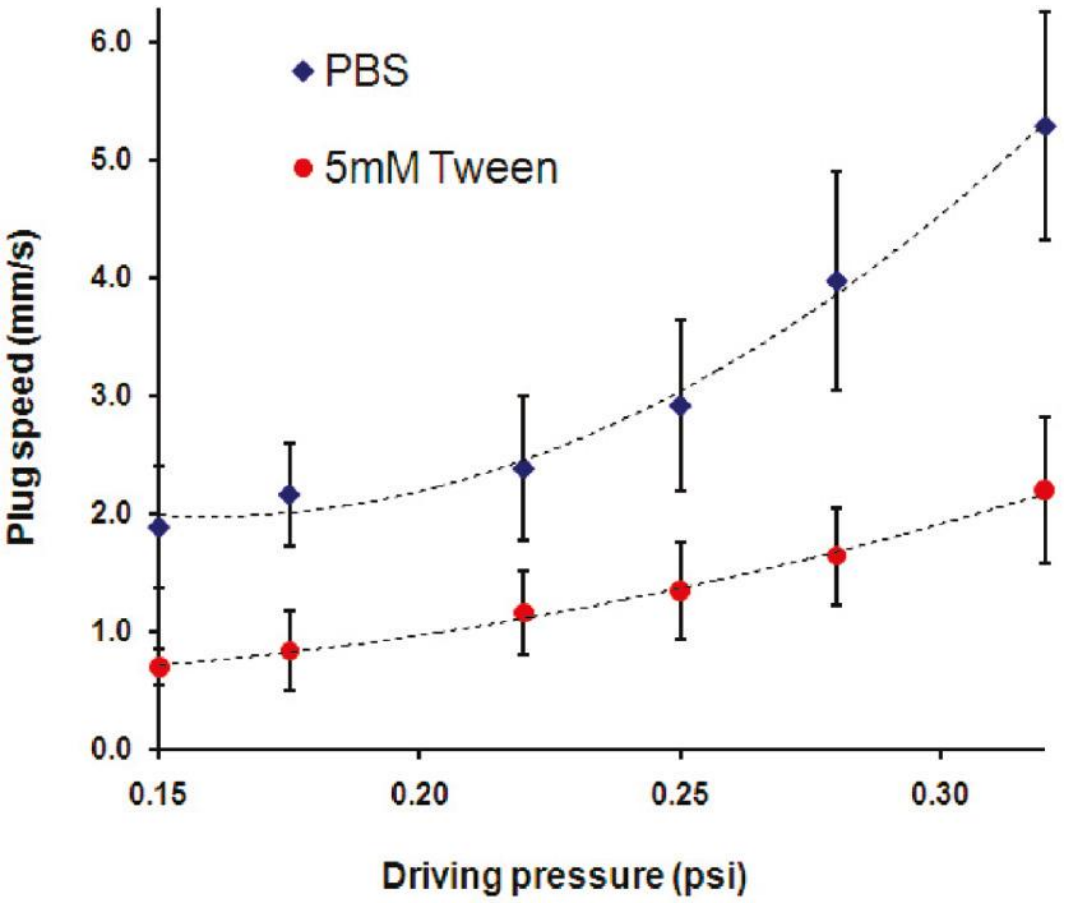

Figure 5.6. Propagation speed of PBS and surfactant liquid plugs is shown as a function of driving air pressure. Overall, PBS plugs propagate about 2.5 times more rapidly than surfactant-containing plugs.

5.5 References

(1) Weibel, E. R.; Gomez, D. M. *Science* **1962**, 137, 577.

(2) Levitzky, M. G., *Pulmonary Physiology*, 7th ed.; The McGraw-Hill Companies Inc.: New York, **2007**.

(3) Macklem, P. T. *Am. J. Respir. Crit. Care Med.* 1998, **157**, S181.

(4) Cassidy, K. J.; Halpern, D.; Ressler, B. G.; Grotberg, J. B. *J. Appl. Physiol.* **1999**, 87, 415.

(5) Grotberg, J. B. *Annu. Rev. Biomed. Eng.* **2001**, 3, 421.

(6) Griese, M.; Birrer, P.; Demirsoy, A. *Eur. Respir. J.* **1997**, 10, 1983.

(7) Gunasekara, L.; Schoel, W. M.; Schurch, S.; Amrein, M. W. *Biochim. Biophys. Acta* **2008**, 1778, 433.

(8) Hohlfeld, J. M. *Respir. Res.* **2002**, 3, 4.

(9) Meyer, K. C.; Sharma, A.; Brown, R.; Weatherly, M.; Moya, F. R.; Lewandoski, J. R.; Zimmerman, J. *Chest* **2000**, 118, 164.

(10) Wright, S. M.; Hockey, P. M.; Enhorning, G.; Strong, P.; Reid, K. B. M.; Holgate, S. T.; Djukanovic, R.; Postle, A. D. *J. Appl. Physiol.* **2000**, 89, 1283.

(11) Tavana, H.; Huh, D.; Grotberg, J. B.; Takayama, S. *Lab. Med.* **2009**, 40, 203.

(12) Pelosi, P.; Rocco, P. R. M. *Crit. Care* **2007**, 11, 114.

(13) Fujioka, H.; Grotberg, J. B. *J. Biomech. Eng.* **2004**, 126, 567.

(14) Bilek, A. M.; Dee, K. C.; Gaver, D. P., III *J. Appl. Physiol.* **2003**, 94, 770.

(15) Fujioka, H.; Takayama, S.; Grotberg, J. B. *Phys. Fluids* **2008**, 20, 062104.

(16) Ghadiali, S. N.; Gaver, D. P. *J. Appl. Physiol.* **2000**, 88, 493.

(17) Halpern, D.; Grotberg, J. B. *J. Fluid Mech.* **1992**, 244, 615.

(18) Corbet, A.; Bucciarelli, R.; Goldman, S.; Mammel, M.; Wold, D.; Long, W. *J. Pediatr.* **1991**, 118, 277.

(19) Jobe, A. H. *N. Engl. J. Med.* **1993**, 328, 861.

(20) Yapicioglu, H.; Yildizdas, D.; Bayram, I.; Sertdemir, Y.; Yilmaz, H. L. *Pulm. Pharmacol. Ther.* **2003**, 16, 327.

(21) Chu, E. K.; Whitehead, T.; Slutsky, S. A. *Crit. Care Med.* **2004**, 32, 168.

(22) D'Angelo, E.; Pecchiari, M.; Baraggia, P.; Saetta, M.; Balestro, E.; Milic- Emili, J. *J. Appl. Physiol.* **2002**, 92, 949.

(23) Dos Santos, C.; Slutsky, A. *J. Appl. Physiol.* **2000**, 89, 1645.

(24) Espinosa, F. F.; Kamm, R. D. *J. Appl. Physiol.* **1998**, 85, 266.

(25) Huh, D.; Fujioka, H.; Tung, Y.-C.; Futai, N.; Paine, R.; Grotberg, J. B.; Takayama, S. *Proc. Natl. Acad. Sci. U.S.A.* **2007**, 104, 18886.

(26) Cubaud, T.; Ho, C.-M. *Phys. Fluids* **2004**, 16, 4575.

(27) Gunther, A.; Jhunjhunwala, M.; Thalmann, M.; Schmidt, M. A.; Jensen, K. F. *Langmuir* **2005**, 21, 1547.

(28) Ody, C. P.; Baroud, C. N.; Langre, E. d. *J. Colloid Interface Sci.* **2007**, 308 231.

(29) Duffy, D. C.; McDonald, J. C.; Schueller, O. J. A.; Whitesides, G. M. *Anal. Chem.* **1998**, 70, 4974.

(30) Chueh, B.-H.; Huh, D.; Kyrtsos, C. R.; Houssin, T.; Futai, N.; Takayama, S. *Anal. Chem.* **2007**, 79, 3504.

(31) Bowden, N.; Huck, W. T. S.; Paul, K. E.; Whitesides, G. M. *Appl. Phys. Lett.* **1999**, 75, 2557.

(32) West, J. B. *Respiratory Physiology: The Essentials*, 8th ed.; Lippincott Williams & Wilkins: Philadelphia, **2008**.

(33) Tsuno, K.; Miura, K.; Takeya, M.; Kolobow, T.; Morioka, T. *Am. Rev. Respir. Dis.* **1991**, 143, 1115.

(34) Tavana, H.; Neumann, A. W. *Adv. Colloid Interface Sci.* **2007**, 132, 1.

(35) Ferguson, G. S.; Chaudhury, M. K.; Biebuyck, H. A.; hitesides, G. M. W. *Macromolecules* **1993**, 26, 5870.

(36) Li, D.; Neumann, A. W. *J. Colloid Interface Sci.* **1990**, 137, 304.

(37) Tavana, H.; Gitiafroz, R.; Hair, M. L.; Neumann, A. W. *J. Adhes.* **2004**, 80, 705.

(38) Willson, D. F.; Chess, P. R.; Notter, R. H. *Pediatr. Clin. N. Am.* **2008**, 55, 545.

(39) Waters, S. L.; Grotberg, J. B. *Phys. Fluids* **2002**, 14, 471.

(40) Fujioka, H.; Grotberg, J. B. *Phys. Fluids* **2005**, 17, 082102.

(41) Frank, B.; Garoff, S. *Langmuir* **1995**, 11, 4333.

(42) Dreyfuss, D.; Martin-Lefevre, L.; Saumon, G. Respir. *Crit. Care Med.* **1999**, 159, 1752.

(43) Halpern, D.; Grotberg, J. B. *J. Biomech. Eng.* **1993**, 115, 271.

(44) Otis, D. R.; Johnson, M.; Pedley, T. J.; Kamm, R. D. *J. Appl. Physiol.* **1993**, 75, 1323.

(45) Halpern, D.; Fujioka, H.; Takayama, S.; Grotberg, J. B. *Respir. Physiol. Neurobiol.* **2008**, 163, 222.

CHAPTER 6

Conclusion and Future Works

The four main research topics described in this thesis has demonstrate the great flexibility of microfluidic systems to be adapted to different kinds of applications. Through innovative design and application of varies engineering principles, microfluidic devices can reach beyond the inherent limitations that is generally associated with its microscale dimensions and low Reynolds number flow operation, while expanding on its advantage as a simple, high throughput, and physiological relevance.

In Chapter 2, we demonstrate that highly unstable, turbulent like flow can be generated, and applied to biological studies in the microchannel. Highly unstable flows are usually not associated with flow within micro fluidic devices, due to its small dimension and the resultant viscous force dominated flow, characterized by low Reynolds numbers. However, as described in the thesis, by exploring the engineering properties of viscoelastic fluids, along with properly designed microchannel geometry, highly unstable flow are observed and applied to in-vitro vascular endothelial cell (EC) studies. Considering the fact that human blood is a complex, highly viscoelastic fluid; in addition to its engineering novelty as a microfluidic test platform, this work also suggest a higher dimension of physical relevance above other Newtonian flow, mechanical system based in-vitro test systems used in similar vascular endothelial cell studies.

Looking forward, we can combine the advantage of the PDMS microchannel device: small package, efficient use of reagent and EC cells, simple mechanical control,

and high throughput capability, and easy monitoring; with the capabilities of generating complex flow patterns foe large scale studies of exploring the effects of complex hemodynamic on vascular EC cells. Microchannels designs could be improved from the current demonstrator version and adapted to larger scale study; by manipulating the channel geometry design and working fluid properties: parallel study platforms with multiple EC samples and multi-flow patterns (Newtonian flow, mildly unstable flow, and highly unstable flow) on the same device are envisioned as the next phase of this research. This could be used in the studies of individual and combined drug response tests and flow modulated microparticle-to-EC layer attachment tests, which has great implication on cancer metastasis, and atherosclerosis.

In Chapter 3, liquid-liquid two-phase flow is utilized, by controlling microchannel geometry and surface property, to create emulsifying flow through flow-focusing phenomena. With emulsified fluid phase being diluted PDMS prepolymer, this work is first report of large scale fabrication of PDMS microspheres in the size range of 85-200 micron. PDMS has many advantageous chemical and mechanical properties which make it a popular material choice in biomedical microfluidic systems. This work expands the possibilities of using PDMS as engineering material by mass production of uniform sized microspheres. Furthermore, the unique capability to generate complex surface patterns and depositions of more functional material on these patterns, greatly expand the potential utilities of these PDMS microspheres.

Future plans including the following: First, further reduction of PDMS microsphere size, potential to cellular scale or beyond. This would be achieved through exploring the known theories of fluid dynamics for two-phasing flow; manipulation of inertial, viscous, and the interfacial forces (include fluid to fluid, and fluids to channel wall) will be the key factors in achieving this goal. And Second, with availability of tailor-sized, uniform PDMS microspheres with functional surfaces; interesting applications can be attempted such as bio-carrier applications or molecular sensing applications (or combined) in microfluidic system.

In Chapter 4 and 5, the role of interfacial tension forces in microchannel is again explored, in combination with other fluid forces, to generate a wide range of two-phase flow patterns. These including continuous two-phase flow patterns (Chapter 4), and Segmented two-phase flow patterns, i.e., liquid plugs (Chapter 5). The dominating role of surface tension forces (includes fluid to fluid, and fluids to channel surfaces), due to the high surface –to-volume ratio, in these different two-phase flow phenomena were discussed thoroughly to evaluate the experimental finding, gaining valuable insights in fundamental mechanisms of these different two-phase flows; also enabling greater abilities to potential control and utilize them for different applications. In the case of liquid plug research, physiological and clinical implications of advancing and rupturing of liquid plugs toward lung injury and treatment were also discussed.

Future works includes further exploring the damaging effects of advancing plugs on pulmonary epithelial cells in-vitro using the currently studied PDMS microchannel with adjustable surface properties which enable control of the plug size and speed.